UAV-based investigations into the hydrology and dynamics of the Greenland Ice Sheet

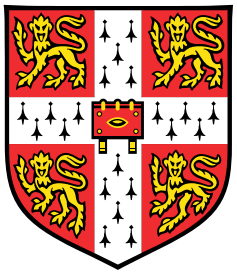

Thomas Russell Chudley

Scott Polar Research Institute
University of Cambridge

This dissertation is submitted for the degree of
Doctor of Philosophy

Downing College

May 2020

Declaration

I hereby declare that except where specific reference is made to the work of others, the contents of this dissertation are original and have not been submitted in whole or in part for consideration for any other degree or qualification in this, or any other university. This dissertation is my own work and contains nothing which is the outcome of work done in collaboration with others, except as specified in the text and Acknowledgements. This dissertation does not exceed the length limits prescribed by the Degree Committee for the Faculty of Earth Sciences and Geography.

Thomas Russell Chudley
May 2020

UAV-based investigations into the hydrology and dynamics of the Greenland Ice Sheet

Thomas Russell Chudley

Variation in the rate of meltwater input into the subglacial system of the Greenland Ice Sheet can force dynamic responses on a range of scales from hourly to interannual. Observations of the ice sheet dynamic response are commonly made either through ground-based Global Navigation Satellite System (GNSS) measurements, which can provide continuous and accurate point measurements, or through satellite remote sensing, which can provide regional-scale observations but at coarse temporal resolutions. This thesis investigates the potential of Unmanned Aerial Vehicles (UAVs) to provide intermediate-level observations of the interactions between ice sheet hydrology and dynamics at a fast-flowing, marine terminating glacier in West Greenland. I first describe the development of a low-cost UAV suitable for deriving ice sheet velocity fields from Structure-from-Motion photogrammetry. In order to geolocate products without using ground control, image locations are determined directly using an on-board L1 GNSS receiver. I validate this method, showing that accuracies are sufficient for producing velocity fields in the ice sheet interior. Next, this method is used, alongside in-situ geophysical observations, to characterise the causes and dynamic influence of a rapid supraglacial lake drainage. I show that rapid drainage can induce a significant dynamic response up to 4 km away from the lake itself, and that fracture history can exert controls on interannual lake drainage behaviour. Finally, I upscale UAV observations using satellite datasets over a $\sim$3,000 km^2 area, exploring dynamic controls on crevasse hydrology. I find that in compressive mean stress compressive regimes, crevasses are more likely to display ponding and rapid hydrofracture than in extensional regimes, where continuous slow drainage is typical. Continued high-resolution observations are necessary to further identify key controls on the hydrological influences of Greenland Ice Sheet dynamics.

Acknowledgements

I have been supported throughout the course of this project by a great number of friends and colleagues. I'd first like to thank my supervisor, Poul Christoffersen, for providing me with an unmissable opportunity; for being an extensive source of academic support, practical guidance, and fieldwork logistics; and most of all for walking the best part of 10 kilometres around a supraglacial lake in 2017 to retrieve a drone that I crash-landed on the wrong side of a river. My thanks also go to Sam Doyle as my informal second supervisor, who was instrumental in steering me through the world of GPS post-processing and sharing invaluable experience of ice sheet hydrology. I am grateful to Neal Snooke and Nick Töberg, who were so generous with their time when helping me to set up and learn to fly the UAVs in the early stages of this study, as well as Guillaume Jouvet for further helpful drone-related discussions. When the time came to process my datasets, Antonio Abellan and Mike James were instrumental in providing expert guidance in all things Structure from Motion, and Tom Dowling was an invaluable mentor for my introduction into the world of machine learning. I am also grateful to Ian Willis, Neil Arnold, Conrad Koziol, Corinne Benedek, Becky Dell, Brent Minchew, Penny How, Johnny Ryan, James Lea, and Evan Miles for various useful discussions throughout the course of my PhD.

Within my research group at the Scott Polar Research Institute, I am indebted to Marion Bougamont for the provision of modelling outputs used in this thesis; to Charlie Schoonman for seismological data and geological insights; to TJ Young for wise and practical fieldwork advice; to Rob Law for doing his best impression of a 'tamed mathematican' when the situation required, and for very kindly not succumbing to cabin fever across endless weeks on an ice sheet; and to my office-mate, Samuel Cook – who has by now definitely earned a break from me – for

endless glaciological discussions and also for letting me copy all his logistics when conference season rolled around. Meanwhile, in the field, I am grateful to Sean Peters for his adept drone-launching skills; Bryn Hubbard for his sage advice on all things glaciology (and his strong, albeit incorrect, opinions on the movie 'Interstellar'); and for the invaluable assistance and good spirits of Nicole Bienert, Mickey Mackie, Eilza Dawson, Mike Prior-Jones, Adam Booth, and Martin Truffer – no matter the hour or how long it had been since we last slept. I am also thankful to Ann Andreasen and the Uummannaq Polar Institute for their kind hospitality whilst in Uummannaq.

This PhD would not have been possible without funding from a Natural Environment Research Council studentship awarded through the Cambridge Earth System Science Doctoral Training Partnership (Grant NE/L002507/1). The wider research project, including logistics and equipment costs, was funded by the European Research Council as part of the RESPONDER project under the European Union's Horizon 2020 research and innovation program (Grant 683043). I am grateful for receiving additional funding for fieldwork and conference costs from Downing College, the Cambridge Philosophical Society, and the Department of Geography Beatrice Shaw Fund.

On top of those already mentioned, a great number of people across Cambridge have contributed to making the past few years a very special time, dragging me (figuratively and on select occasions literally) through the trials and tribulations of completing a PhD. In the department, Henry Anderson-Elliott, Peter Martin, Andrew Williamson, Helen Brooks, Amy McGuire, Frazer Christie, and Christine Batchelor were an endless distraction from work and a reliable motley crew for frequent visits to the pubs (and, on occasion, the cocktail bars, student kitchens, parks, MCRs, fields, and basements) of Cambridge. I will always be grateful for the friendship and support of my Downing College extended second family, including – but not limited to – Parsa Akbari, Gabriel Greening, Shenaiya Kharegat, Audrey Valreau, Helen Jambunathan, Aneira Pugh, Josh Mehta, Josh Newman, Ben Young, Liron Shmilovits, Giles Rought Whitta, Jake Longhorn, Caitlin Bones, Charlotte Imianowski, Elliot Shaw, Gaby Baxter, Ella Brown, Conor Simpson, and Phil Docherty.

Finallly, I am thankful to my family, for their endless and unwavering patience, support, and encouragement.

Table of contents

List of figures

List of tables

List of nomenclature

Roman Symbols

s_{RMSE}	Uncertainty contribution from Root Mean Square Error
s_{xy}	Horizontal Uncertainty
s_z	Vertical Uncertainty

Greek Symbols

Δt	Time interval
$\dot{\epsilon}$	Strain Rate
$\dot{\epsilon}_e$	Effective Strain Rate
$\dot{\epsilon}_l$	Longitudinal Strain Rate
$\dot{\epsilon}_{ij}$	Strain Rate Tensor
$\nabla\theta$	Gradient of the hydraulic potential surface
∇H	Gradient of ice thickness
∇Z_b	Gradient of bed elevation
ρ_i	Density of ice
ρ_w	Density of water

σ_1 First Principal Stress

σ_2 Second Principal Stress

σ_l Longitudinal Stress

σ_m Mean Stress

σ_v von Mises Stress

σ_{ij} Stress Tensor

σ_{sv} Signed von Mises Stress

B Viscosity Parameter

Acronyms / Abbreviations

a.g.l. above ground level

a.s.l. above sea level

API Application Programming Interfaces

dGPS Differential GPS

DSO Direct Sensor Orientation

GCP Ground Control Point

GIS Geographic Information System

GLONASS Global'naya Navigatsionnaya Sputnikovaya Sistema

GNSS Global Navigation Satellite System

GNSS-AT GNSS-supported Aerial Triangulation

GoLIVE Global Land Ice Velocity Extraction from Landsat 8

GPS Global Positioning System

GrIS Greenland Ice Sheet

GSD Ground Sampling Distance

GUI Graphical User Interface

HALE High Altitude, Long Endurance (UAV)

IMU Inertial Measurement Unit

InSO Indirect Sensor Orientation

IPCC International Panel of Climate Change

ITS_ LIVE Inter-mission Time Series of Land Ice Velocity and Elevation

LEFM Linear Elastic Fracture Mechanics

LiDAR Light Detection And Ranging

MEaSUREs Making Earth System Data Records for Use in Research Environments

MVS Multi-View Stereo

NDWI Normalised Difference Water Index

OBIA Object-Based Image Analysis

PIV Particle Image Velicometry

PPK Post Processed Kinematic (GPS)

RCP Representative Concentration Pathway

RESPONDER Resolving subglacial properties, hydrological networks and dynamic evolution of ice flow on the Greenland Ice Sheet

RGB Red Green Blue

RINEX Receiver Independent Exchange Format

RTK Real Time Kinematic (GPS)

SAR Synthetic Aperture Radar

SfM Structure from Motion

SIFT Scale-Invariant Feature Transform

SLR Sea Level Rise

SMB Surface Mass Balance

SNR Signal-to-Noise Ratio

SPS Standard Positioning System (GPS)

TRI Terrestrial Radar Interferometry

UAV Uncrewed Aerial Vehicle

UTC Coordinated Universal Time

WGST West Greenland Summer Time

Chapter 1

Introduction

1.1 Thesis motivation

Prior to the 21st century, ice sheets were understood to respond to climate change on scales of 100s–1000s of years. The past two decades have seen this assumption reassessed as mass losses from the Greenland Ice Sheet (GrIS) have rapidly accelerated (Bevis et al., 2019; King et al., 2018; Mankoff et al., 2019; Meredith et al., 2019; Mouginot et al., 2019a; Shepherd et al., 2012; Van den Broeke et al., 2016; Velicogna et al., 2014). Having been close to balance in the early 1990s, mass balance has transitioned from +31 $\pm$ 83 Gt a^{-1} between 1992–1996 to -247 $\pm$ 15 Gt a^{-1} between 2012–2016 (Bamber et al., 2018). The rate of acceleration of losses from the GrIS have exceeded other sources of global cryospheric mass loss (Figure 1.1a) and form an increasing proportion of global mean sea level rise (SLR), rising from less than 5% of SLR (0.11 mm a^{-1}) in 1993 and more than 25% (0.85 mm a^{-1}) in 2014 (Chen et al., 2017). The ongoing deglaciation of the GrIS has significant potential consequences for society, as the ice sheet constitutes 2.99 $\times$ 10^6 km^3 (2.74 $\times$ 10^6 Gt) of ice, which, were the volume above floatation were to melt completely, would be equivalent to 7.42 metres of global sea level rise (Morlighem et al., 2017).

The GrIS can lose mass via either negative surface mass balance (SMB) (i.e. surface melting) or from dynamic losses, which can be broadly divided into (i) outflow changes in marine-terminating glaciers; (ii) indirect interactions between SMB and ice flow via thinning; and (iii) basal lubrication from the interaction of surface

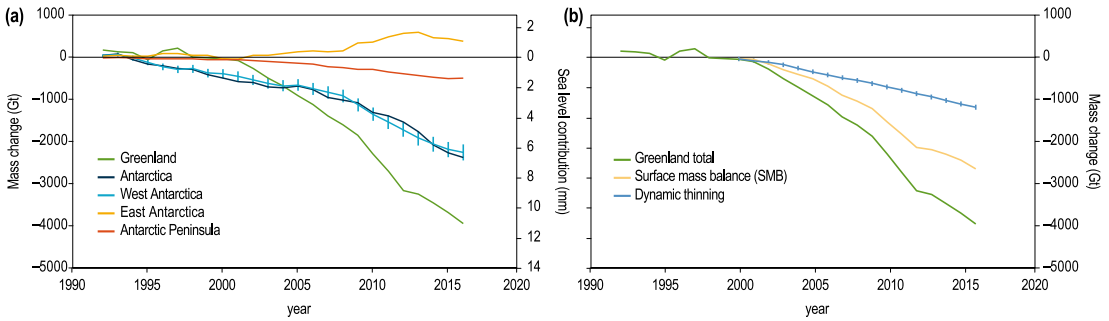

Fig. 1.1 (a) Cumulative ice sheet mass change, 1992–2016 (Bamber et al., 2018; IMBIE Team, 2018). (b) Greenland Ice Sheet mass change components. 2000–2016, from surface mass balance (orange) and dynamic thinning (blue) (King et al., 2018; Van den Broeke et al., 2016). Uncertainties = 1 standard deviation. Figure from Meredith et al. (2019).

meltwater with the bed (Church et al., 2013). Approximately 40% of GrIS mass loss between 1991–2015 can be attributed to these dynamic losses (Van den Broeke et al., 2016), with a particularly exceptional acceleration in discharge losses between the early 1990s and mid 2000s (Figure 1.1b; Meredith et al., 2019). Although Greenland-wide discharge has apparently stabilised since the mid-2000s (Figure 1.1b), this is dominated by slowdown at the largest outlet glaciers, and elsewhere losses from discharge continue to rise (King et al., 2018).

Whilst our observational understanding of GrIS mass balance continues to improve, there remain key deficiencies in our understanding of the underlying mechanisms of the dynamic acceleration of the GrIS, and in particular the coupling between runoff, subglacial hydrology, and glacier dynamics ('hydro-dynamic coupling'). Over 95% of supraglacial melt enters the ice sheet, primarily through crevasses or moulins opened by supraglacial lake drainage events (Koziol et al., 2017). Once water has been routed to the subglacial system, ice dynamics can be influenced by altering the effective pressure at the bed (Schoof, 2010), modifying the connectivity and efficiency of the subglacial system (Cowton et al., 2016), and, in the longer term, warming the ice via cryo-hydrologic warming (Phillips et al., 2010). At first thought to be a strictly positive feedback whereby enhanced meltwater production results in a corresponding ice sheet acceleration, further research has shown that complementary negative feedback mechanisms exist that offset ice acceleration and have even been found even to result in a net slowdown on annual to interannual timescales (Sole et al., 2013; Sundal et al., 2011; Tedstone

et al., 2015). The interaction of positive and negative feedbacks is complex, and as a result modelling the long-term impact of increased meltwater production is challenging. Indeed, in 2013, the Intergovernmental Panel on Climate Change (IPCC) Fifth Assessment Report excluded the interaction of hydrology and dynamics entirely from modelling efforts, making the assumption that hydological positive and negative feedbacks will cancel out, resulting in an insignificant contribution to sea level rise from this process over the next century (Church et al., 2013). In the more recent IPCC Special Report on Oceans and Cryosphere, the modelled effects of of meltwater on ice dynamics are still assessed to be small (Oppenheimer et al., 2019). However, in recent years, research has highlighted further unresolved questions regarding the hydrology of the GrIS, including the implications of meltwater delivery at higher elevations of the ice sheet (Doyle et al., 2014; Poinar et al., 2019), the significance of cryo-hydrologic warming (Lüthi et al., 2015; Poinar et al., 2017a), and the role that hydrology plays at tidewater glaciers (Bevan et al., 2015; King et al., 2018). The last question is particularly pertinent in discussions of dynamic mass loss from the GrIS, as the majority of investigations into GrIS hydrology have been performed in land-terminating environments, and the extent to which knowledge derived from them can be applied to marine-terminating environments is unclear (Nienow et al., 2017). Hence, it is imperative to develop a better understanding of hydro-dynamic coupling in marine-terminating sectors, in order to improve our understanding and numerical modelling of the extent to which dynamic losses from the GrIS will contribute to SLR in the 21st century and beyond.

Concurrent with advances in our understanding of GrIS hydrology, the past decade has seen the maturation of Uncrewed Aerial Vehicles (UAVs) as a platform for aerial remote sensing in glaciology (Bhardwaj et al., 2016), in particular through the use of Structure-from-Motion with Multi-View Stereo (SfM-MVS) photogrammetry to reconstruct detailed 3-dimensional surface models from overlapping sequential imagery (Westoby et al., 2012). UAVs provide an accessible, customisable, and flexible option to obtain 3-D observations at high spatial and temporal resolutions. Detailed surface observations obained from UAVs have been integrated into studies of ice sheet and glacier hydrology (Kraaijenbrink et al., 2016b; Rippin et al., 2015; Smith et al., 2017), whilst accurate repeat observations allow for glacier velocity fields to be obtained from feature-tracking methods, resulting in further applications in studies of glacier dynamics (Jouvet et al., 2017,

2019; Kraaijenbrink et al., 2016a; Ryan et al., 2015; Seier et al., 2017; Wigmore and Mark, 2017). However, the geospatial accuracy necessary to derive ice velocity is difficult to achieve at marine-terminating glaciers, as the creation and maintenance of dense networks of ground control points (GCPs) necessary to geolocate photogrammetric models (Seier et al., 2017) is logistically challenging due to the widespread prevalence of crevasses and the rapid advection of in-situ GCPs. Limitations on the production of glacier velocity fields mean that previous studies examining the interior of the ice sheet have focussed on non-dynamic glaciological questions, such as those relating to surface hydrology or albedo (Cook et al., 2020; Ryan et al., 2017, 2018; Smith et al., 2017). However, recent developments in methods and software supporting alternative geolocation techniques, alongside continuing reductions in the price and accessibility of low-cost carrier-phase global navigation satellite system (GNSS) receivers, have allowed for the popularisation of alternative geolocation method known as GNSS-supported Aerial Triangulation (GNSS-AT), or 'direct geolocation', whereby georeferencing is performed via the accurate geolocation of individual aerial photographs (Benassi et al., 2017; Fazeli et al., 2016; Hugenholtz et al., 2016). This method is beginning to emerge in applications in the broader geosciences (Strick et al., 2018; van der Sluijs et al., 2018), and is ripe for adaptation to a glaciological context.

1.2 Aims & Objectives

The research gaps outlined above have motivated the primary aim of this thesis, which is to develop and explore the potential of UAVs to gain further understanding of the relationship between the hydrology and ice dynamics at a marine-terminating sector of the GrIS. As such, this thesis has two primary aims: the first is to develop a workable method to derive accurate velocity data from UAV imagery whilst working within the practical restrictions of an ice sheet environment; the second is to apply this method to further our understanding of hydro-dynamic coupling in marine-terminating sectors of the Greenland ice sheet. Three primary objectives are outlined following these aims:

1. Develop and validate a low-cost method for UAV-derived photogrammetry able to produce, without the use of GCP networks, photogrammetric prod-

ucts of a suitable accuracy to derive short-term (∼daily) velocity fields of the ice sheet interior. This work is presented in Chapter 3.

2. Use the UAVs and methodology developed from objective (1), alongside *in-situ* geophysical data, to investigate supraglacial lake drainages and associated subglacial hydrological pathways. This work is presented in Chapter 4.

3. Use the UAVs and methodology developed from objective (1), alongside satellite remote sensing data, to characterise the dynamic controls on meltwater delivery to the bed from water-filled crevasses. This work is presented in Chapter 5.

1.3 Work presented in this thesis

This thesis consists of six chapters, including this introduction:

Chapter 1 frames the underlying motivations and introduces the key objectives of the thesis.

Chapter 2 the current state of the knowledge regarding the hydrology and dynamics of the Greenland Ice Sheet, and the methods used to study them. It also introduces the principles of SfM-MVS photogrammetry and the current state of the art of UAV applications in glaciology.

Chapter 3 describes the development of a UAV platform suitable for inferring ice sheet dynamics, and applies and validates the method in an outlet glacier environment.

Chapter 4 applies the method, along with ground-based geophysical instrumentation, to the study of the dynamic impacts of a rapidly draining supraglacial lake.

Chapter 5 explores the integration of UAV and satellite data to investigate the relationship between crevasse hydrology and surface stress.

Chapter 6 summarises and synthesises the developments described in the thesis, and highlights possible avenues for future research.

1.4 Publications resulting from this thesis

The material in chapters 3 and 4 of this thesis have been published (Chudley et al., 2019a,b), and the material in chapter 5 is under peer review. The co-authors of these publications provided research oversight, methodological guidance, raw primary data (e.g. GPS base station data), and processed supporting data (e.g. seismic data and hydrological flow routing). All of the analysis and manuscript writing was undertaken by the the thesis author, with co-authors providing feedback. Named co-authors, and their contributions to the research, are identified in the author-contribution statements at the beginnings of each respective chapter and the ends of the published papers.

Chapter 2

Background

The purpose of this chapter is to briefly introduce the background and most recent literature necessary to understand the context of the following chapters. It is divided into two main sections: the first summarises the state of knowledge on the interaction between the hydrology and dynamics of the Greenland Ice Sheet; and the second introduces UAVs and Structure-from-Motion photogrammetry as a method to study glacier and ice sheet dynamics.

2.1 The hydrology and dynamics of the Greenland Ice Sheet

2.1.1 Supraglacial hydrology

Following the onset of the industrial era, air temperatures have been trending upwards in Greenland since the 1830s (Trusel et al., 2018), experiencing a step acceleration in the 1990s (Box, 2013; Trusel et al., 2018; Van Angelen et al., 2014). High temperatures have resulted in a consequential increase in the frequency, duration, and intensity of melt events (Box, 2013; Fettweis et al., 2017; Meredith et al., 2019; Noël et al., 2017; Trusel et al., 2018), with 1994–2013 runoff being 33% (50%) higher than the mean for the 20^{th} (18^{th}) century (Trusel et al., 2018). In particular, 2003–2013 marked a particularly intense period of surface melt, aided by large-

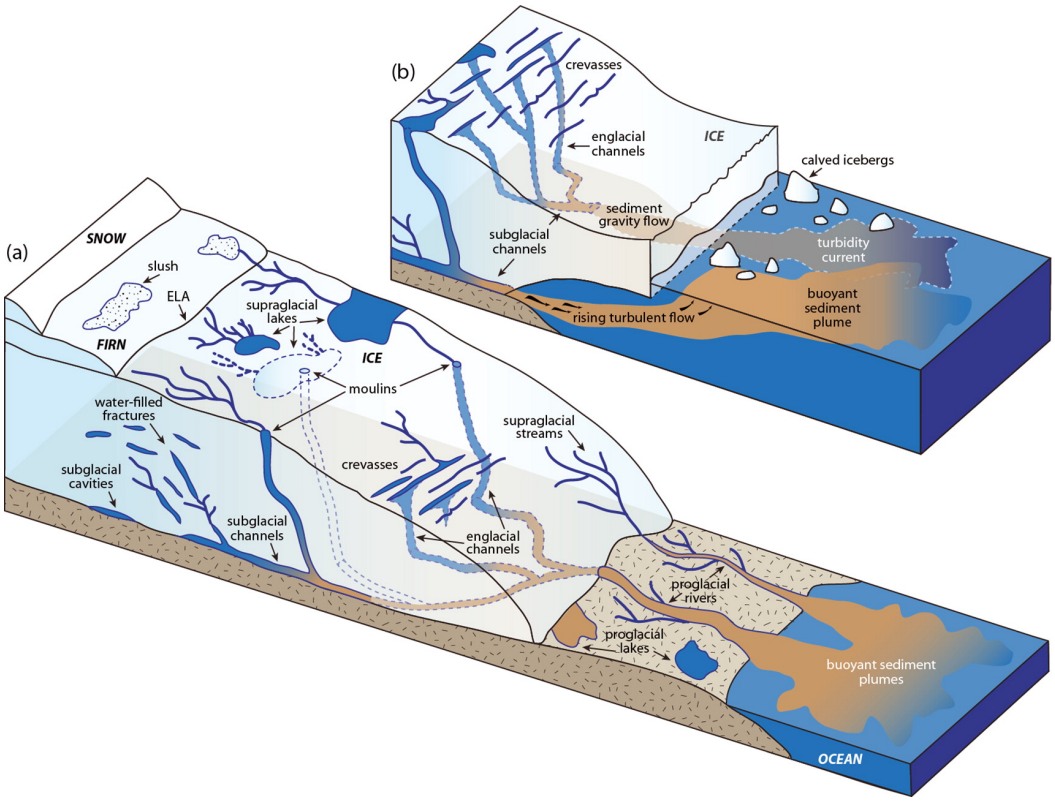

Fig. 2.1 Conceptual model of Greenland hydrology. (a) Hydrological pathways, from accumulation zone to proglacial environment, in a land-terminating system. (b) Differences at the calving front for a marine-terminating glacier. Figure from Chu (2014).

scale atmospheric variations such as a negative summer phase North Atlantic Oscillation (NAO) index (Bevis et al., 2019; Van Angelen et al., 2014) and high summer Greenland Blocking Index (Hanna et al., 2016), culminating in a record 2012 melt season where, at its peak, as much as 98.6% of the entire ice sheet surface was found to have experienced surface melt (Hanna et al., 2014; Nghiem et al., 2012).

Of this surface melt, a majority of runoff is routed to the bed of the ice sheet (Smith et al., 2017) through a variety of access points to the englacial system (Figure 2.1) including crevasses (Colgan et al., 2011; McGrath et al., 2011), supraglacial lake drainage events (Das et al., 2008; Doyle et al., 2013; Stevens et al., 2015), and the moulins they form (Catania and Neumann, 2010; Hoffman et al., 2018). For a representative area of West Greenland, modelling has estimated that over 95% of surface runoff enters the ice sheet during a typical melt season: 47% through crevasses, 3% through direct lake drainage, 21% through the moulins subse-

quently opened by lake drainages, and 15% through moulins already existing or opened by other means (Koziol et al., 2017). An elevation bias occurs within this distribution, with crevasses more likely to drain runoff at lower elevations (Clason et al., 2015; Koziol et al., 2017). At higher elevations, some temporary storage may also occur at the ice sheet surface (Cooper et al., 2018) and in firn aquifers (Forster et al., 2014; Koenig et al., 2014), although the total capability of these systems may be limited as warming continues (MacFerrin et al., 2019; Machguth et al., 2016).

Supraglacial Lakes

Over 2000 lakes form across the GrIS every summer (Selmes et al., 2011) as runoff collects within topographic depressions on the ice-sheet surface. Following early work from aerial imagery by Echelmeyer et al. (1991), a proliferation of remote sensing studies have characterised lake formation across the GrIS. Many of these studies are focussed in the west and south-west of the ice sheet (Cooley and Christoffersen, 2017; Fitzpatrick et al., 2014; Morriss et al., 2013; Williamson et al., 2017, 2018a), although studies in other locations (Gledhill and Williamson, 2018; Macdonald et al., 2018), as well as GrIS-wide studies (Selmes et al., 2011, 2013), are becoming more common. As topographic depressions are controlled by bedrock topography, lakes form in the same place year after year, allowing for their inter-annual response to climate change to be characterised. In response to increases in surface temperature and a rising equilibrium line altitude, lakes have been advancing further inland over the observational satellite record, particularly in the post-2000 period (Gledhill and Williamson, 2018; Howat et al., 2013), as well as becoming larger in area and draining in greater abundance (Cooley and Christoffersen, 2017). These trends are predicted to continue into the future, with Leeson et al. (2015) modelling that, in southwest Greenland, lakes may appear another 110 km inland by 2060 under an extreme (RCP 8.5) climate change scenario, which is representative of current trends. Ignéczi et al. (2016) further showed a 174% increase in total lake volume across the GrIS by 2070–2099 relative to 1980–2009 under the RCP 8.5 scenario.

Many lakes on the ice sheet drain 'rapidly' (on the scale of $\sim$hours), whereby a surface-to-bed connection is opened via a hydraulically-driven fracture mechanism termed hydrofracture (Das et al., 2008; Krawczynski et al., 2009; van der

Veen, 2007). Satellite observations have shown that 28-45% of supraglacial lakes drain rapidly (Cooley and Christoffersen, 2017; Fitzpatrick et al., 2014), although lakes that exhibit rapid drainage behaviour do so in fewer than half of years (Morriss et al., 2013; Selmes et al., 2013). However, there is uncertainty surrounding the exact factors controlling hydrofracture, and the timing of hydrofracture is seemingly stochastic. Although water volume-based thresholds are often used to predict lake drainge in modelling studies (e.g. Arnold et al., 2014; Banwell et al., 2016), analysis has failed to support the hypothesis that the drainage of lakes can be explained by any critical thresholds relating to lake hydrology (depth, volume, or morphology), glaciological setting (hypsometry, velocity, or strain) or meteorological conditions (Fitzpatrick et al., 2014; Williamson et al., 2018b). Field-based studies have observed lake drainages to exploit pre-existing moulins (Doyle et al., 2013; Stevens et al., 2015), suggesting that water entering the subglacial system from an overtopping lake via a previously-existing surface-to-bed connection may be able to trigger hydrofracture by inducing localised acceleration (as a 'precursor event') and hence a transient extensional flow regime (Alley et al., 2005; Stevens et al., 2015). Meanwhile, Christoffersen et al. (2018) propose that lake drainages may be able to induce transient extensional flow sufficient to act as precursor events from as far as 80 km, allowing for cascading chain reaction of lake drainages.

Rapid supraglacial lake drainages have remained an important consideration for GrIS hydro-dynamic coupling (Section 2.1.2) despite directly draining only 3% of total runoff in rapid drainage events (Koziol et al., 2017). This is because lake-induced hydrofracture forms the majority of moulins (Hoffman et al., 2018) which can go on to efficiently deliver runoff to the bed (Koziol et al., 2017; McGrath et al., 2011) for weeks to years (Catania and Neumann, 2010), strongly affecting the development of subglacial drainage systems (Banwell et al., 2016). However, not all supraglacial lakes drain rapidly via hydrofracture. Some drain 'slowly' (on a scale of $\sim$days) into pre-existing moulins outside of the basin via lake overtopping and resultant incision of a supraglacial outlet channel (Clason et al., 2015; Kingslake et al., 2015; Koziol et al., 2017; Tedesco et al., 2013). Additionally, lakes that remain at the end of the melt season will become buried or freeze, persisting through the winter (Koenig et al., 2015; Law et al., 2020; Miles et al., 2017; Selmes et al., 2013), although the total proportion of meltwater that refreezes in this way is estimated to be small (Koziol et al., 2017).

Crevasses

Despite accounting for 47% of surface runoff drainage (Koziol et al., 2017), the means by which water is routed to the bed through crevasses has received far less study than for supraglacial lakes, which account for only 27% of drainage. Crevasses were largely ignored in models of GrIS surface hydrology (Arnold et al., 2014; Banwell et al., 2013) until recently (Clason et al., 2015; Koziol et al., 2017). The fundamental principle of hydrofracture remains the same as for lake drainage, and indeed, was considered for water-filled crevasses before lakes were widely studied (Van der Veen, 1998; Weertman, 1973). However, several aspects of crevasses mark them as hydrologically distinct from lake drainages and moulins. Many studies, supported by observations from mountain glaciers (Fountain et al., 2005), consider crevasses to continuously, but inefficiently, route water to the subglacial system (Colgan et al., 2011; McGrath et al., 2011). In contrast, water-filled crevasse systems have also been observed to undergo episodic discrete drainage (Cavanagh et al., 2017; Lampkin et al., 2013) in a way analogous to supraglacial lakes. These assumptions are mutually exclusive, and both contrasting views have been incorporated into the two state-of-the-art models of regional surface hydrology that incorporate crevasse systems (Clason et al., 2015; Koziol et al., 2017). As the efficiency of meltwater delivery to the subglacial system has consequences for subglacial hydrology (Section 2.1.2), understanding conditions under which these two contrasting mechanisms are representative of GrIS crevasse hydrology is key to accurately representing crevasses in models needed to estimate future rates of sea level rise.

2.1.2 Subglacial hydrology and hydro-dynamic coupling

Physical principles and conceptual models

Glacier motion, driven principally by gravitational driving stress, is composed of three processes: the deformation of the ice column due to the visco-elastic nature of ice, the sliding of the glacier across the underlying bed, and, where the bed is composed of unconsolidated sediment, by basal deformation (Cuffey and Paterson, 2010). The generation of surface melt, and subsequent routing to the subglacial environment, has the potential to modulate all three of these dynamic

processes. Much of our understanding of subglacial hydrology that is outlined in this section has been derived from initial studies of valley glaciers (e.g. Kamb, 1987; Nienow et al., 1998; Sharp et al., 1993). However, several studies have shown that, at least at the southwestern margins of the GrIS where water inputs are large, the seasonal hydrology of the GrIS can be understood in terms of the same conceptual model (Andrews et al., 2014; Bartholomew et al., 2010, 2012; Chandler et al., 2013).

Routing of water to the ice-bed interface can affect basal motion for both hard and soft beds, as increased basal water pressure results in reduced effective pressure (defined as ice overburden minus basal water pressure). In hard beds, this results in hydraulic ice-bed seperation ('hydraulic jacking'), which results in increased ice velocity via reduced basal friction. In soft beds, increased pore water pressure in the subglacial sediment results in sediment weakening, and as a result increased basal deformation. Hence, regardless of bed type, as the effective pressure drops, ice velocity is expected to increase. The relationship between water input and effective pressure is, however, modulated by the state of the subglacial hydrological system. These states can be broadly divided into two modes. The first group are referred to as distributed, or inefficient, systems. In these systems – which can include groundwater flow, sheet flow, or, at hard beds, subglacial cavities occurring on the lee side of bedrock topography (Figure 2.2a; Fountain and Walder, 1998) – water flux is slow and inputs cannot be evacuated efficiently. As such, ice creep closure of cavities results in increased water pressure and prevents the closure of distributed drainage networks, whilst increased discharge into the system results in increased water pressures (Figure 2.2c). Alternatively, in channelised, or efficient, systems, conduits can be carved upwards into the ice (Röthlisberger, 1972) or downwards into bedrock or sediments (Nye, 1976) that efficiently transport water towards the ice margins. These channels are maintained by viscous dissipation (i.e. frictional heating in the water), either melting of the ice of the channel wall (Figure 2.2b) or eroding the soft sediment of the channel bed. This process allows efficient systems to accommodate increases in discharge by expanding their cross-sectional area, maintaining high effective pressure at high rates of discharge. As water supply into a distributed system increases, the system can switch into a channelised system at a critical discharge threshold (Figure 2.2c) as an oversupply of water begins to drive the form efficient pathways. This is a positive feedback, as channelisation reduces local water pressure, meaning that more water will en-

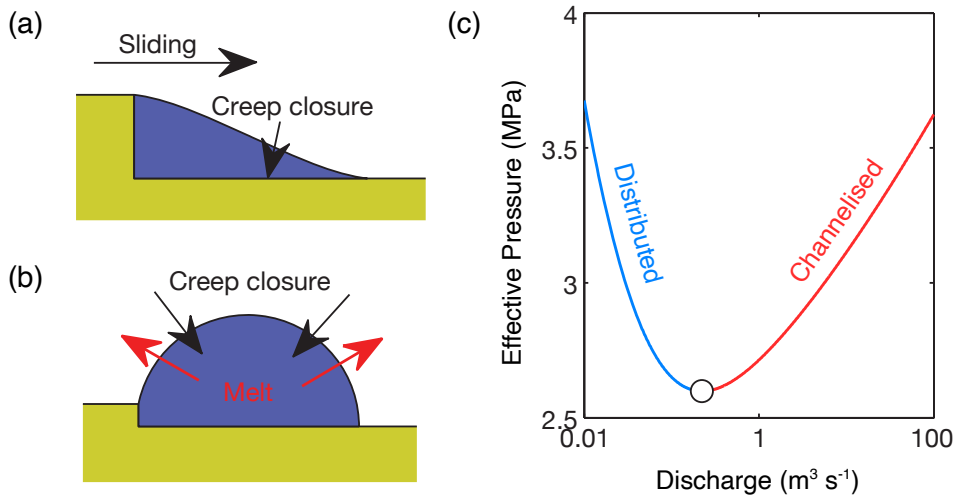

Fig. 2.2 Physics of (a) cavities and (b) channels. (c) Relationship between steady-state discharge and effective pressure, with the point at which a conduit becomes a channel marked with a white circle. Figure adapted from Schoof (2010).

ter the channel from surrounding zones of high basal water pressure along the pressure gradient. In contrast, a reduction in discharge means that channel sizes cannot be sustained, and eventually will result in the collapse of a channelised drainage system back into a distributed form. The ability for an inefficient subglacial system to accommodate a sustained increase in water flux by transitioning to an efficient system means that ice acceleration is largely forced by short-term spikes in water pressure, such as from diurnal melt cycles, rainfall events, and lake drainages (Schoof, 2010). At land-terminating ice sheet margins, sustained increases in supply have been shown to result in the development of an efficient channelised system (Andrews et al., 2018), leading to a net increase in effective pressure.

The principles outlined above underlie the common conceptual model of the seasonal cycle of hydro-dynamics that occur at the temperate beds of glaciers (Hubbard and Nienow, 1997; Nienow et al., 1998) and ice sheets (Andrews et al., 2018; Bartholomew et al., 2010; Palmer et al., 2011; Sole et al., 2011). According to this model, at the beginning of the melt season, water is contained in the subglacial system (Chu et al., 2016) in an inefficient, distributed state. As the melt season begins, water enters the subglacial system but cannot be evacuated efficiently due

to the low water flux, initiating a high-pressure state that induces higher ice velocities (Bartholomew et al., 2012; Meierbachtol et al., 2016). This is often referred to as the 'spring event' (Mair et al., 2001). High daily melt rates in the early ablation season may induce accelerations of as much as 50-200% of the background winter velocities in this period (Joughin et al., 2013; Palmer et al., 2011). However, this high-pressure state is not sustained, as the development of an efficient drainage system acts to evacuate water from the system and increase effective pressure, allowing further melt supply to be accommodated in the system (Chandler et al., 2013; Sundal et al., 2011).

A longer-term way in which water can alter the flow of an ice sheet is cryo-hydrologic warming. The rate factor in the Nye-Glen flow law has a strong temperature dependency (Cuffey and Paterson, 2010), and as such an increase in ice temperature has the ability to reduce ice viscosity and thus lead to faster ice flow on the order of years–decades. Phillips et al. (2013b, 2010) proposed that large quantities of meltwater delivering latent heat to the englacial or subglacial system could explain ice flow rates that exceed model predictions in certain sectors of the GrIS.

Long-term implications for GrIS dynamics

Early concerns over the potential long-term (inter-annual – decadal) effects of increased meltwater supply were raised by Zwally et al. (2002), who were the first to use GPS records to identify seasonal acceleration in the west GrIS in response to summer melting, sparking a research focus that has lasted nearly two decades. In the intervening time, a better understanding has been gained of this impact on a variety of scales, from hourly to interannual. Although short-term accelerations are observed in response to impulses of runoff delivery to the bed, such as following supraglacial lake drainage events (Das et al., 2008; Doyle et al., 2013; Stevens et al., 2015) or rainfall events (Doyle et al., 2015; Tedstone et al., 2013), in the long-term studies have appeared to show that, at least at land-terminating margins, rising summer melt on the GrIS since the 1990s has been associated with a net slowdown in ice velocities (Tedstone et al., 2015; Williams et al., 2020). For reasons described above, this slowdown in ice velocities appears to be a consistent feature of the GrIS melt season at the margins (up to 30–40 km inland) of the land-terminating ice sheet (Andrews et al., 2018; Cowton et al., 2016; Van de Wal et al.,

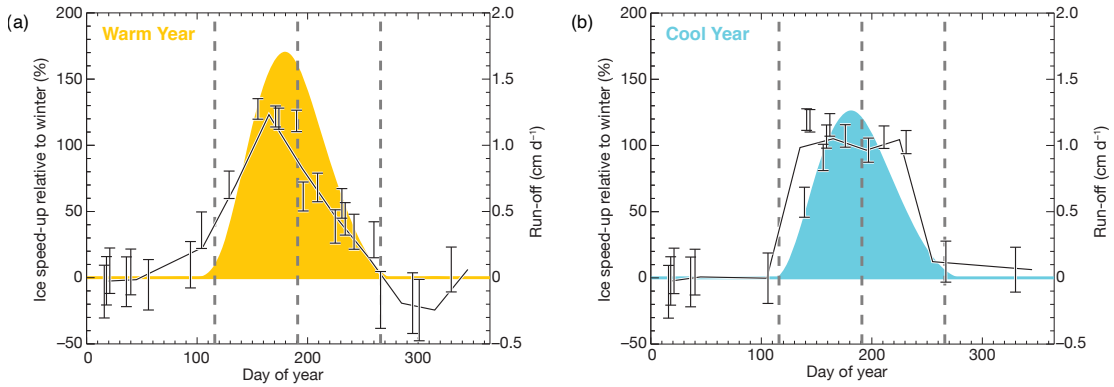

Fig. 2.3 Seasonal ice velocities and surface runoff in (a) warm and (b) cool years, from Sundal et al. (2011).

2015) as transition to an efficient, channelised drainage system occurs (Chandler et al., 2013; Cowton et al., 2013). It is thought that on an inter-annual scale, an increasing melt supply will further enhance the late-season negative feedback and result in slow annual velocities (Figure 2.3), either by forcing an earlier transition to an efficient system (Sundal et al., 2011) or by slowing winter velocities via a reduction in the volume of water stored subglacially overwinter (Sole et al., 2013).

As a result of these negative feedbacks, in 2013 the IPCC Fifth Assessment Report concluded that basal lubrication will make an insignificant contribution to sea level rise over the next century, with positive and negative feedbacks cancelling out. As a result, the process was excluded entirely from subsequent modelling efforts (Church et al., 2013). In the time since this report, however, it has become clear there are major unresolved questions regarding Greenland hydro-dynamics that require answers before the net impact of a changing hydrology on GrIS dynamics can be properly predicted and numerically modelled (Nienow et al., 2017).

One unresolved factor is the significance of cryo-hydrologic warming on ice sheet acceleration (Phillips et al., 2013b, 2010). Borehole temperature profiles have found warmer temperatures than would reasonably occur from heat diffusion and dissipation alone (Harrington et al., 2015; Lüthi et al., 2015), which is thought to occur due the latent heat released during the englacial refreezing of meltwater. However, the extent to which cryo-hydrologic warming may be able to influence ice velocities has been questioned. At the rates of warming calculated, >60% of ice in Greenland flows too quickly through the ablation zone for cryo-hydrologic warm-

ing to be significant (Poinar et al., 2015), and modelling studies for west Greenland have estimated that a 10 °C increase in ice temperature at 300 m depth results in only a 10 m a^{-1} increase in ice velocity (Poinar et al., 2017a). In contrast, Colgan et al. (2011) have argued that an increase in coverage of crevasses may facilitate cryo-hydrologic warming, as warming is sensitive to the mean spacing of hydrologic pathways. Studies of cryo-hydrologic warming are uncommon, and it is still plausible that the mechanism may have long-term consequences for ice dynamics.

The other unresolved factor is the extent to which observations of long term hydro-dynamic decelerations are applicable away from land-terminating ice sheet margins. Observations have shown that at inland sites, where the ice sheet is thicker, accelerations can be sustained further into the melt season (Bartholomew et al., 2012; Van de Wal et al., 2015) and, in contrast to the margins, can be enhanced during warmer years as opposed to cooler years (Doyle et al., 2014; Sole et al., 2013), potentially due to: (i) thicker ice limiting the development of channelised systems due to greater ice creep closure; or (ii) a flatter inland surface, which reduces the hydraulic gradient and lowers the subglacial water flux, potentially hindering channel growth and formation. Faster winter flow was also observed by Doyle et al. (2014), possibly related to summer meltwater input decoupling frozen sticky spots or warming basal ice. In addition, firn aquifers have recently been found to be exploiting crevasses to transfer water to the bed inland of Helheim Glacier at ∼1500 m a.s.l. (Poinar et al., 2017b), with modelling results showing a consequential raising of inland subglacial water pressure (Poinar et al., 2019). Hydrological influence may further be enhanced if the expansion of lakes inland (Ignéczi et al., 2016; Leeson et al., 2015) is also associated with ongoing rapid lake drainage. Poinar et al. (2015) argued that low surface strain inland may limit the ability of crevasses to hydrofracture to the bed, but other studies have found that rapid drainage is relatively insensitive to elevation (Cooley and Christoffersen, 2017) and that rapid lake drainages can induce transient tensile stresses sufficient to induce further hydrofracture as far as 80 km away (Christoffersen et al., 2018). These studies only consider supraglacial lake drainage, as parallel relationships between dynamics and crevasse hydrology have yet to be explored. Regardless, it might be expected that ongoing net deceleration at the land-terminating margins may have to be considered alongside net acceleration further inland at land-terminating sectors (Davison et al., 2019). The extent to

which these understandings can be applied at marine-terminating margins is even less clear (Nienow et al., 2017): this is the focus of the next section.

2.1.3 Marine-terminating outlet glaciers

Significance and dynamic controls

Marine-terminating (or tidewater) outlet glaciers act to drain ice from the ice sheet interior, losing mass to the ocean environment via calving and submarine melting. Particularly common in the northwest and south-east of the ice sheet, the GrIS contains approximately 276 fast-flowing (>100 m a^{-1}) outlet glaciers (Mankoff et al., 2019), with wide variability in parameters such as size, discharge, and recent velocity response (Moon et al., 2012, 2014). Discharge from marine terminating outlet glaciers contributed 66% of the total GrIS mass loss (9.1 mm of SLR) between 1972–2018, increasing by 18% over the time period (Mouginot et al., 2019a). Recently, a combination of accelerating SMB losses and a halt in the acceleration of discharge losses since the mid-2000s (Figure 1.1b) has meant that SMB has come to dominate, with discharge contributing only 40% of total GrIS mass loss between 1991–2015 (Van den Broeke et al., 2016). However, this apparent stabilisation is dominated by slowdown and thinning at the four largest outlet glaciers, and across the rest of the ice sheet, losses from discharge continue to accelerate (King et al., 2018).

Influences on outlet glacier discharge can be broadly divided into oceanic and atmospheric (i.e. surface melt and its effect on subglacial hydrology controls). Initial rapid acceleration in discharge and retreat of marine-terminating glaciers was likely driven by oceanic influence from warm waters entering fjord systems (Seale et al., 2011; Straneo et al., 2010), modulated by local factors to introduce high heterogeneity in glacier response (Enderlin et al., 2014; Felikson et al., 2017; King et al., 2018; Moon et al., 2012). Once ocean-induced changes at the calving front occur, they can induce dynamic thinning far inland (Bondzio et al., 2017; Felikson et al., 2017; Nick et al., 2009). This secondary mass loss is so significant that it likely outweighs that directly resulting from the retreat of the calving front, with >75% of total mass loss coming from long-term feedbacks (Price et al., 2011). As such, it is clear that oceanic controls have significant and long-term influences on

the behaviour of marine-terminating outlet glaciers in Greenland. Given the magnitude of this oceanic influence, the relative importance of atmospheric influences in the marine-terminating sector has been questioned (Nick et al., 2009). Furthermore, it has been suggested that basal friction supports very little of the driving stress beneath Greenland's fastest flowing glaciers (Shapero et al., 2016), so velocity response from variability in basal water pressures may be limited. Even the long-term influence from cryo-hydrologic warming has been questioned, as in fast-flowing areas, rapid advection through the ablation zone reduces the timescales over which latent heat can be delivered to the bed (Poinar et al., 2015).

Hydrology and dynamics at marine-terminating outlet glaciers

More recent work has suggested that atmospheric influences still play an important role in the future response of marine-terminating outlet glaciers. Indeed, even oceanic influence has been found to be strongly modulated by runoff, as meltwater emerges at the front in the form of plumes that can control both calving and submarine melt mechanisms. They have been found to impact both the location, style, and rate of calving (Chauche et al., 2014; Fried et al., 2018) as well as the rate of submarine melting (Cowton et al., 2015; Slater et al., 2018, 2016). As well as modulating frontal dynamics, there is good evidence that changes in the subglacial system still impact seasonal dynamics. Howat et al. (2010) found that, for five out of six studied marine-terminating glaciers in west Greenland, seasonal accelerations 4–6 km from the calving front indicated the effects of subglacial drainage system evolution and not variations in front position – findings that have been replicated in further remote sensing studies (Moon et al., 2014; Rathmann et al., 2017). Csatho et al. (2014) found, with laser altimetry, rapid thickening since $\sim$2005 that occurred too far into the interior to be explained by inland propagation of ocean-driven processes. Even near the calving front, Bevan et al. (2015) attributed dynamic thinning at Helheim Glacier between 2011–2014 to melt-induced acceleration rather than oceanic influence. Most recently, King et al. (2018) found that GrIS-wide discharge reaches a seasonal maximum 13 ± 9 days after the fastest increase in runoff, which is similar to a previously estimated 18-day average residence time for water in the subglacial environment (Van Angelen et al., 2014). This suggests that discharge may peak around the time that maximum pressurisation of the subglacial drainage system might be expected. Even

so, total discharge losses do not correlate with either the seasonal maximum nor seasonally integrated runoff, suggesting that more complex mechanisms underlie these relationships.

The biggest weakness in our understanding of the hydrology of marine-terminating glaciers arguably lies in the extent to which we can apply processes occurring in the land-terminating margins, from where much of our understanding is derived, to that of the less-studied marine-terminating margin (Flowers, 2018; Nienow et al., 2017). In contrast to land-terminating margins, it may be easier for high basal water pressures to be maintained at marine-terminating margins: near the calving front, the hydrological system will remain continually pressured as it meets the ocean, and, as occurs during the active phase of surging glaciers (Kamb, 1987), a channelised drainage system may be difficult to maintain at high rates of basal sliding (Nienow et al., 2017). Few have been able to supplement understanding gained from remotely sensed data and numerical modelling with field-based measurements (Catania et al., 2020). Fieldwork at marine-terminating outlet glaciers introduces additional logistical challenges: crevasse fields are extensive, limiting the operational zones suitable for surface geophysics, and the longevity of borehole instrumentation is limited by high strain rates. Although some studies exist across the GrIS, studies of the glacier bed from fast-flowing (>100 m a^{-1}) glaciers remain limited to a few boreholes at Jakobshavn Isbræ (Funk et al., 1994; Iken et al., 1993; Lüthi et al., 2002), with some supporting data from slower-flowing, but still marine-terminating, sectors (Walter et al., 2014). Most recently, a series of integrated geophysical datasets from Store Glacier have been published, which, given the relevance to this thesis, are focussed on here.

Primary instrumentation at Store Glacier included active seismic surveys (Hofstede et al., 2018), borehole instrumentation (Doyle et al., 2018), and autonomous phase-sensitive radio echo sounding (Young et al., 2019). These studies build up a picture of the basal environment where fast flow is divided between an ∼80 m layer of easily deformable anisotropic ice below the Holocene-Wisconsin transition, explaining 29–37% of the observed surface velocity, underlain by a thick (∼45 m) layer of unconsolidated sediments whose deformation explains 63–71% of the ice velocity (Doyle et al., 2018; Hofstede et al., 2018). Boreholes drained rapidly upon reaching the bed, indicating a connection to an active subglacial hydrologic system (Doyle et al., 2018). Diurnal variability in subglacial water

pressure and surface velocity are indicative of surface runoff accessing the bed. Distinct peaks in velocity were reached on days following peak surface ablation rates, and occurred coincident with peaks in uplift rate, indicative of hydraulic ice-bed separation. Small (<0.5%) variations in effective pressure (which was typically low, between 2–10% of overburden) were associated with accelerations in surface velocities of 6–81%. This is significant, although proportionally less sensitive to runoff input than observed at land-terminating sectors (e.g. >100% recorded by Bartholomew et al., 2010). However, in contrast to land-terminating observations, no evidence was found for additional slowdown following high-velocity events. Given the observational evidence, the system was interpreted to be likely inefficient in nature, with water flowing through (and possibly above) a thick subglacial sediment layer maintained by, and facilitating, fast glacier flow (Doyle et al., 2018). However, seismic reflectivity was highly variable across scales of ∼100s of metres, likely representing transitions between water stored in the pore spaces of the unconsolidated till layer and a second system where unconsolidated till is absent and water exists at the ice-bed interface (Hofstede et al., 2018). This suggests not only that basal slipperiness is highly heterogeneous, but that on the scale of hundreds of metres, Coulomb-type plastic flow of basil till can exist alongside Weertman-type basal sliding.

The apparently high spatial heterogeneity of subglacial behaviour highlights a gap in spatial scales that existing methods use to observe and understand hydrodynamic behaviour. Boreholes and other *in-situ* geophysics are highly effective at building a detailed and continuous dataset of behaviour, but by their nature are 'point data' that have limited effectiveness at assessing spatial heterogeneity, especially in marine-terminating environments where additional logistical challenges are introduced to instrumentation. At the other end of the observational spectrum, remote sensing methods can be used to assess regional change, but it is rare (and often opportunistic) that these observation have the ability to observe short term (<∼days) and localised (∼100s m) accelerations (Joughin et al., 2013; Palmer et al., 2011). This motivates the development of new observational methods that can gain high-resolution understandings of ice dynamics whilst working around field risks in highly crevassed marine-terminating glaciers.

2.2 UAVs and SfM-MVS photogrammetry for assessing glacier motion

Photogrammetry, as relevant to the geosciences, is the process of obtaining geometric properties of objects from photographs. It is arguably the oldest form of remote sensing, and in the most basic form can be as simple as measuring the distance between two points in a single image of a known scale. In contemporary usage most references to photogrammetry refer to *stereophotogrammetry*, whereby 3-D coordinates of points in a scene are calculated from two or more photographs taken from different positions. Photogrammetry has been used for geoscience applications for many decades, making use of both ground-based camera positions ('terrestrial photogrammetry') and sequential photography taken from aircraft ('aerial photogrammetry') and satellites ('satellite photogrammetry'). In glaciology, there is a decades-long history to photogrammetric studies performed from both terrestrial (Finsterwalder, 1954; Kick, 1966) and aerial (Brecher, 1986; Konecny, 1966) imagery, including for the calculation of glacier velocity (Brecher, 1986; Kick, 1966; Voigt, 1966).

Within the past decade, geoscience has seen a renaissance of photogrammetry based on a combination of two factors. The first factor is the emergence, since the 1990s, of a flexible and user-friendly form of photogrammetry: Structure-from-Motion (SfM) paired with Multi-View Stereo (MVS) algorithms, abbreviated to SfM-MVS or commonly just SfM. SfM-MVS allows for 3-D positions to be computed from images without needing the the full suite of prior information that is commonly required for traditional photogrammetry, such as image location and orientation, camera calibration parameters, or surveyed GCPs within a scene. SfM-MVS is also now available in the form of user-friendly software, with accessible Graphical User Interfaces (GUIs) as well as Application Programming Interfaces (APIs) in languages widely-used in the geosciences, such as Python. The two primary advantages of SfM-MVS in its modern form are that it is (i) cheap, and (ii) accessible. SfM data can provide 3-D point data of a similar density and, when properly performed, of comparable accuracy to methods such as light detection and ranging (LiDAR) for a fraction of the price. With multidimensional points containing both XYZ and optical red-green-blue (RGB) data, outputs can be transformed into a variety of alternative formats, such as orthophotos and digital ele-

vation models (DEMs), allowing a single dataset to perform multiple functions to the end user. Additionally, the ability to perform photogrammetry without the requirement for a full suite of prior information has also unlocked a wider suite of historic aerial record for processing, allowing historic glacier geometry to be derived from otherwise challenging input data (e.g. Holmlund and Holmlund, 2019; Mölg and Bolch, 2017). The downsides of using SfM-MVS include the fact that data quality is dependent on factors such as lighting and surface texture that cannot be controlled by the end user, a particular issue in polar environments where snow often obscures surfaces of interest (or indeed is the surface of interest). This is compounded as SfM-MVS is often processing-intensive, meaning that full-quality products cannot be produced in the field, limiting opportunities for real-time quality assessment. Additionally, commercial SfM-MVS software, whilst outperforming open-source alternatives in data quality and ease of use, are 'black box', which makes identifying causes of error difficult. It has been shown that different SfM-MVS software produce different quality results (Gindraux et al., 2017; Mölg and Bolch, 2017), but a lack of ability to understand the underlying software means that picking the 'best' or 'correct' software for a given use case is difficult.

The second factor in the recent popularity of photogrammetry is the development and proliferation of uncrewed aerial vehicles (UAVs) and other low-cost, user-friendly technologies that facilitate the collection of aerial data by the 'typical' geoscientist operating without specialist engineering knowledge or collaborators. These systems have proved popular in recent years as they now represent mainstream, low-cost systems made from off-the-shelf components – supported by an increasingly sophisticated ecosystem of open-source autopilot hardware and software. Whitehead and Hugenholtz (2014) highlight that particular aspects of the modern UAV make them attractive to environmental and earth scientists: (i) low initial and operating costs (especially compared to traditional manned aerial platforms); (ii) autonomous operation, which minimises the expertise required from human operators; (iii) manoeuvrability, making UAVs ideal for low-altitude flying in complex, often mountainous environments; (iv) the ability to operate in diverse environments; (v) a reduced exposure risk to pilots; (vi) a regulatory framework that enables research and commercial operations. This has resulted in rapidly increasing amounts of UAV-based studies in recent years, and a proliferation of low-cost instrumentation has allowed for remote sensing applications limited not just to SfM-MVS (the focus of this section and thesis) but alternative in-

strumentation including LiDAR (Sankey et al., 2017) and gas composition sensors (Liu et al., 2019). The downsides of UAVs include their vulnerability to weather, especially in extreme environments, where intense winds and precipitation can prevent flights (although UAVs can operate in certain weathers, such as high cloud cover, that would limit optical satellites). Additionally, UAVs have a relatively small range and payload capacity compared to manned aerial platforms. This can vary over a wide range, from quadcopters with flight times in the tens of minutes to professional UAVs with military applications that can fly for days. However, as a general rule, as the capability of UAVs increase, so does the cost and operating expertise required to run them, leading to a natural trade-off in investment and performance.

Having provided a general introduction to SfM-MVS and UAVs, the rest of this section will be divided into three parts. The first focusses on the principles and specific technical workflow of SfM-MVS. The second reviews existing methods of deriving glacier motion, providing a methodological underpinning to the work in this thesis. The third briefly reviews the existing glaciological literature deriving glacier motion from UAVs and SfM-MVS.

2.2.1 Principles of SfM-MVS

This section provides a brief description of the workflow and principles of the SfM-MVS process. For a comprehensive description of Structure-from-Motion (SfM) photogrammetry, the reader is referred to Carrivick et al. (2016), Furukawa and Hernández (2015), and Snavely et al. (2008), the first of which the following summary is predominantly sourced. The SfM-MVS process refers to what is in fact a cascade of processes and software (Figure 2.4) that will vary in exact nature between implementations. The common examples referred to here are open-source in nature and black-box commercial applications (including Agisoft Metashape, the SfM-MVS software used in this thesis) may differ in exact implementations.

The first stage in the SfM-MVS workflow is *feature detection*, the identification of common 'keypoints' between images. To identify matching points between images with wide baselines (large distances between images), methods must be used

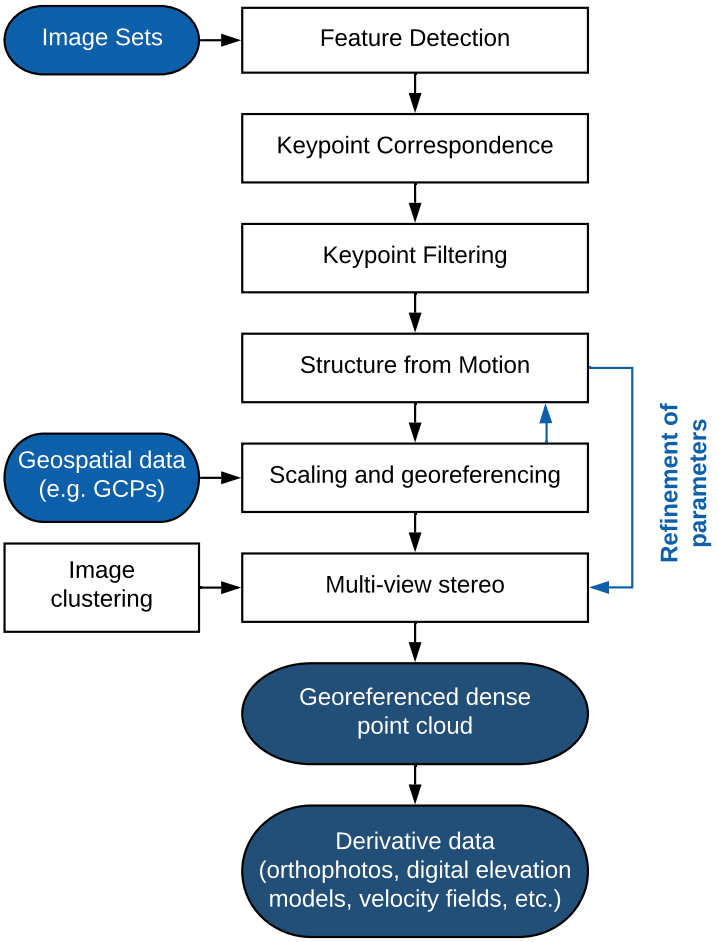

Fig. 2.4 Flowchart showing principal steps in the SfM-MVS workflow. Based on figure from from Carrivick et al. (2016).

that can successfully identify features invariant to changes in scale, orientation, and other geometric distortions associated with changes in perspective. The most commonly used system is the scale-invariant feature transform (SIFT; Lowe, 2004). Keypoints are identified based on detecting local extremes in monochrome intensity that are stable even when convolving with a Gaussian function at a variety of different scales. Images that offer a high density of keypoints are sharp, high-texture, and contain a complex scene. As such, snow and ice are considered a particular challenge for SfM-MVS: however, practical assessment of UAV-based SfM-MVS in a glacial environment has shown that, except for surfaces covered in fresh snow, surface texture does not significantly influence final model accuracy (Gindraux et al., 2017).

Following feature detection, *keypoint correspondence* must be performed to match keypoints between images. Potentially hundreds of images may have hundreds or thousands of keypoints each, and the SIFT algorithm assigns every keypoint a 128-dimension descriptor. Hence, matching keypoints has the potential to be highly computationally intensive. However, a variety of efficient algorithms are used based upon k-dimensional trees, which partition data into bins based upon splitting points such as median values, allowing large regions of the search space to be efficiently eliminated. After keypoints have been matched, *keypoint filtering* is performed to remove erroneous matches. Where multiple keypoints are identified between pairs of images, a 3×3 fundamental matrix can be constructed describing the spatial relationship between the pair. By iteratively subsampling input keypoints and assessing error, outliers can be identified and removed, leaving behind geometrically consistent matches.

Then, *Structure from Motion* can be performed. This is the process where, from feature correspondences previously identified, three parameters are simultaneously reconstructed: (i) 3-D scene geometry (structure); (ii) camera positions and orientations (motion); and, where not provided, (iii) intrinsic camera calibration parameters, such as focal length and coefficients of radial distortion. Parameters are first given initial values via 'sequential' SfM, whereby structure and motion are estimated pairwise. This begins with an initial pair of images with a large number of matches and baseline, allowing for a robust reconstruction of their spatial relationship. Successive images are incorporated one at a time. Once multiple images have been incorporated into the model, a 'bundle adjustment' can be undertaken. This involves refining structure and motion for all images simultaneously, an iterative process whereby the aim is to minimise a cost function quantifying reprojection errors. Outlier keypoints with high errors are removed after every iteration. This process is repeated, adding further images via sequential SfM and optimising the model using bundle adjustment, until no further images remain to be added to the model.

The output of the SfM process is a 'sparse' point cloud (matched keypoints) and reconstructed camera poses. However, these locations and geometries are only output in an arbitrary coordinate system, and must be scaled and oriented into a real coordinate system via *georeferencing*. Doing so requires a minimum of three points identified with real-world XYZ coordinates. These real-world coordinates

can be in the form of ground control points (GCPs), rigorously surveyed targets visible in the input images, or in the form of GNSS-supported aerial triangulation (GNSS-AT, or 'direct' georeferencing) whereby image positions are recorded in real time using a survey-grade GNSS receiver. A combination of the two can also be used, whereby coarse camera locations (often from the lower-precision navigational GNSS used as part of UAV surveys) are used to initialise the bundle adjustment, before GCPs are used to accurately constrain the geolocation. The move from GCP-based to direct georeferencing for glaciological purposes is a key advancement made in this thesis: chapter 3 describes the development and validation of a suitable workflow, with section 3.2.3 describing the background and method in detail. Following the addition of geospatial reference points, bundle adjustment can be performed again to further refine the scene geometry and camera parameters.

In the final step, *Multi-View Stereo* techniques are used in order to transform the data output from a sparse point cloud, consisting only of keypoints, to a high-resolution 'dense' point cloud, where point density may increase by as much a two orders of magnitude. To reduce computational burden, a preprocessing step called *image clustering* is often performed. This involves splitting the larger scene-wide process into smaller chunks, or clusters, of overlapping images. An MVS algorithm, of which a wide variety exist (Seitz et al., 2006), may then be applied. MVS relies upon the now well-parameterised camera locations and distortions to reconstruct surfaces under principles akin to traditional stereophotogrammetry, albeit from multiple viewpoints, finding corresponding pixels between images. A popular and effective MVS method is the patch-based MVS (Furukawa and Ponce, 2010), whereby once initial matched pixels are identified in 3-D, 'patches' are created, expanding into neighbouring pixels, until patches overlap. A filtering step is applied to account for any depth discontinuities that occur between neighbouring patches. This final dense cloud can be converted into a variety of alternative geospatial products according to the need of the final user. In glaciological applications, RGB orthophotos and DEMs are often selected as outputs, such that they can be included as part of familiar processing pipelines such as feature-tracking algorithms, or loaded into traditional Geographic Information System (GIS) software packages.

2.2.2 Methods for assessing ice motion

To understand the context for UAV-derived SfM-MVS to assess glacier motion, it is useful to review established methods for assessing ice motion - particularly as the principles of both GNSS and optical feature tracking techniques are employed in the methods used in this thesis.

Field-based techniques

The oldest form of measurement of glacier motion, used as far back as Agassiz (1847), involves the repeat measurement of a network of stakes in the glacier surface using theodolites. Although having fallen out of favour since the early 2000s as alternative methods emerged, they still hold value in that they can record multiple measurements at sub-daily sampling rates without a high financial cost, and, once stakes or reflectors are set out, without needing to traverse the glacier. Advancements such as auto-theodolite scanners means that this research tool has still been used in the modern era to supplement more expensive in-situ measurement techniques such as GPS (Harper et al., 2007).

In the past decade, theodolite-based stake measurement has largely been supplanted by alternative field-based techniques such as terrestrial radar interferometry (TRI) and LiDAR datasets. LiDAR produces dense and precise 3-D point cloud data from which velocities can be extracted using particle image velocimetry (PIV) (Telling et al., 2017). Interferograms from TRI acquisitions can be turned into line-of-sight velocities using known wavelengths and differences between image acquisitions (Voytenko et al., 2015) - this must be converted to true velocity by making assumptions about glacier flow direction, although this process can be more rigourous with two TRI units (Voytenko et al., 2017). The precision and automated nature of both of these methods allow for a velocity field to be constructed over a large area (on the order of 1–10 kilometres) with a high temporal resolution (down to a scale of minutes), properties that cannot be replicated using traditional stake measurements. However, there are also limitations to these methods. Individual data files are extremely large, especially when run at high sampling frequencies, and so storage space limits the ability of these techniques to run unattended for extended periods of time (e.g. left to run between fieldwork

seasons). They must be placed on stable ground with good line-of-sight across the study area, which limits their applications to valley glaciers and ice sheet calving fronts. Finally, the equipment has a high capital cost, which limits their accessibility.

The issue of cost in field-based techniques has been addressed recently through the use of terrestrial photogrammetry, which can be performed with off-the-shelf commercial cameras (e.g. Mallalieu et al., 2020, 2017). Here, velocities can be derived from a network of cameras by measuring the displacement of point clouds produced from stereophotogrammetry (Schwalbe and Maas, 2017) or alternatively from one camera ('monoscopic photogrammetry') with the image projected onto a well-constrained DEM (Messerli and Grinsted, 2015). As rigourous SfM can produce point clouds as dense and accurate as LiDAR (Carrivick et al., 2016), this provides a low-cost alternative to expensive field-based methods that can also be set up to collect long time-lapse datasets. However, it also introduces weaknesses associated with SfM, such as a requirement for good camera geometry which may not be possible in challenging proglacial environments (particularly fjords), and poor reconstruction of geometries with low-texture surfaces.

GNSS techniques

A Global Navigation Satellite System (GNSS) is a satellite constellation that, by continuously transmitting timing and positional data, allows GNSS receivers on Earth to determine their location from the unobstructed view of four or more satellites. GNSS are passive systems, not requiring the transmission of data by the user, nor connection via telephone or internet systems. This is beneficial for independent operation in remote environments. The oldest and most well known of these is the American Global Positioning System (GPS), although other examples include the European Union's Galileo, Russia's Global'naya Navigatsionnaya Sputnikovaya Sistema (GLONASS), and China's BeiDou. The work in this thesis is based exclusively upon the GPS constellation. Using multiple constellations can help to improve geolocation, especially when the sky view is poor (e.g. in mountainous terrain), but increases the data file size. Given that a 180° sky view can be consistently achieved in an ice sheet environment, optimising file size was prioritised over observing additional constellations. A basic outline of the method is

provided in this section in order to provide context for the use of GPS in Chapter 3, along with a brief outline of the use of GNSS in glaciology. For a comprehensive review the reader is referred to Leick (2004) and Doyle (2014).

GNSS can be compared to the terrestrial surveying technique of trilateration, using measurements of distance from known points (in this case, satellites) to determine a position. The record of the location of a satellite through time is referred to as its *ephemeris*. GPS satellites continuously broadcast a navigation (NAV) message at 50 Hz on two frequencies: L1 (1575.42 MHz) and L2 (1227.6 MHz). The NAV message contains information essential to the derivation of location such as the satellite ID, ephemeris, and an accurate time. They also transmit continuous pseudorandom code as a phase modulated binary signal in two formats: the coarse acquisition (C/A) code, available on the L1 frequency, and the precise (P) code, available on both L1 and L2 frequencies. The same pseudorandom code is also being generated by an internal oscillator in the ground-based receiver. By calculating the phase shift between the received and generated signal, signal travel time, and thus an estimate of satellite range (the *pseudorange)*, can be calculated. Given a number of errors propagating through the process (such as satellite orbital errors, ionospheric interference, multipath effects, and receiver noise) the maximum resolution achievable when calculating phase shift is, as a rule of thumb, about 1% of the wave length of the signal. As such, higher-frequency signals allow for more precise geolocation. The C/A code, transmitting at 1.023 MHz (wavelength $\sim$300 m), is sufficient to provide a best-case level of accuracy $\pm$3 m in the horizontal. Utilising the P code, at 10.23 MHz, will achieve $\pm$0.3 m. Exclusive use of the C/A code is referred to as the standard positioning service (SPS), and is used in everyday applications such as smartphones where precise positioning is not required and low receiver costs are a priority.

By applying a number of further corrections, better accuracies can be achieved. The first way this can be done is by utilising the phase shift of the carrier wavelength itself, rather than the modulated code. For the L1 signal (1575.42 MHz; wavelength $\sim$19 cm), utilising the carrier phase means that measurements can be made down to approximately 2 mm. This requires, however, specially equipped receivers that come with an additional cost. The second is to address errors introduced by the time-variable delay as the GPS signal passes through the charged particles of the ionosphere. L1 measurements utilise a simple ionospheric model

broadcast by the GPS satellites, but, as ionospheric delay is frequency-dependent, dual-frequency (i.e. L1 and L2) observations can be used to estimate and remove the effects of the ionosphere. Once again, dual-frequency receivers come at an additional expense. Finally, relative positioning (also known as differential GPS or dGPS) can be used when both a static 'base' station of known coordinates and a moving 'rover' are available. This technique allows the removal of all errors that are common to both receivers, which will include everything except multipath errors (assuming that the effects of the ionosphere are uniform, which is broadly true over baselines $<\sim$10 km).

These approaches can be combined. For instance, relative positioning can take advantage of the carrier-based ranging rather than code-based ranging, whereupon it is referred to a kinematic (rather than differential) GPS. This can be performed in real time (RTK) or post-processed (PPK) if a real-time link between the base station and receiver cannot be established, or the user would like to take advantage of the precise ephemeris (as opposed to the broadcast ephemeris), which is only available in the days following the observation. Kinematic methods are sufficient to achieve sub-centimetre accuracy in positioning. In addition, relative positioning can be performed over a wider baseline ($\sim$100 km) by using using dual-frequency receivers to account for the effects of the spatially variable ionosphere.

Given the difficulty of obtaining measurements through traditional survey techniques in glacier environments (where line-of-sight to stable bedrock is often lacking), glaciologists were early adopters of GPS surveying. Initial receivers were large, heavy, and expensive, so glacier velocities were derived using a single receiver, transported using a vehicle such as a snowmobile, to measure the movement of multiple stakes, before post-processing was applied differentially (Hinze and Seeber, 1988). Although limited by the necessity of the user to be in the field, as well as limitations on repeat time when surveying a large area, it is still an efficient method when the number of available GPS receivers are limited compared to the desired survey scale. However, as GPS receivers became more affordable, the installation of continuously-operating on-ice GPS receivers became feasible, allowing for continuous records of ice motion to be derived. Early limitations included battery capacity, meaning that some studies operated GPSs intermittently on a scheduled basis (e.g. Zwally et al., 2002). Additionally, it was common to use single-frequency receivers and as such be reliant on SPS position-

ing (e.g. van de Wal et al., 2008) , meaning that reliable estimates of glacier velocity required temporal averaging and thus were not able to assess sub-daily variation in ice velocity. However, most modern state-of-the-art studies will take advantage of dual-frequency carrier phase receivers, which, although expensive, will allow for kinematic processing to obtain centimetre-scale precision, and thus the determination of sub-daily variability in ice velocity (including uplift) even tens of kilometres away from bedrock-located base stations (e.g. Doyle et al., 2014, 2015).

Satellite techniques

The continuous, high-frequency measurements of ice motion made available by modern dual-frequency carrier-phase GNSS receivers are provided at the expense of spatial coverage, as GPS records effectively represent discrete point data. At the other end of this spectrum lie observations of glacier velocity from satellite data, which can provide a regional (or even global) spatial coverage but at a proportionally poorer sampling interval (on the scale of days–weeks) and coarse spatial scale (on the scale tens–hundreds of metres).

The two broad classifications of satellite systems used to derive glacier velocity are optical and synthetic aperture radar (SAR) imagery. Optical satellite imagery has the advantage of generally being provided 'analysis-ready' (e.g. Landsat Level 2 surface reflectance) with very little optional pre-processing, such as edge detection, required before velocities can be derived. However, it has the disadvantage of utilising wavelengths that are not able to pass through clouds, so continuous coverage can be disrupted, and – as a passive sensing system – high latitude regions are not observable in the winter during the polar night. The use of active SAR imaging can get around these limitations, as clouds are transparent to microwave and the radiation is emitted by the satellite. However, SAR imagery requires significantly more intensive pre-processing before velocities can be derived. Additionally, SAR instruments are often side-looking, making velocity retrievals difficult in mountainous terrain (e.g. the trunks of outlet glaciers).

The most commonly applied method of obtaining glacier velocity from remotely sensed datasets (including those within this study) is that of feature tracking. Feature tracking is based around identifying the spatial offsets between matching groups of pixels visible in a pair of images. The group of pixels, known as a tem-

plate or interrogation window, is matched across a larger area (known as a search window) using a correlation algorithm (e.g Messerli and Grinsted, 2015; Taylor et al., 2010). Pixel offset can then be converted into a velocity using the known spatial resolution, geospatial projection, and temporal baseline of the images. Feature tracking is the only method to obtain velocity datasets from optical datasets, but is also used with SAR data (Lemos et al., 2018), where it is often referred to as 'speckle tracking' with reference to the backscatter pixel intensity. SAR sensors can also provide more precise velocity information via interferometric techniques, which involve phase-based differencing of successive target returns (the full description of which is beyond the scope of this review). With this method, precision can be 1–2 orders of magnitude greater than feature tracking approaches. This allows for ice velocity information in very slow-flowing areas, such as the interior of ice sheets (Mouginot et al., 2019b), but comes with more complex data acquisition and processing requirements. For example, single-orbit passes only measure line-of-sight velocity, and so multiple passes are required at different angles (e.g. ascending and descending) in order to derive true velocity.

A combination of open data practices, increased processing power, and openly available feature tracking algorithms has seen a step-change in the ubiquity of satellite-derived velocity datasets across glaciological studies in recent years. Indeed, the onset of the 'big data' era has seen the automated ingestion and production of near-real-time glacier velocity fields in recent years, both from optical feature tracking (Fahnestock et al., 2016) and, more recently, from SAR offset tracking (Lemos et al., 2018). However, the medium-resolution satellite sensors commonly used to derive remotely sensed glacier velocity products are of relatively limited spatial (10s of metres) and temporal (∼days-weeks) resolution. As a result, rapid or low-amplitude variations in glacier dynamic behaviour can be missed using satellites, with many studies focussing only on intra-annual (Tedstone et al., 2015; Williams et al., 2020) or intra-seasonal (Palmer et al., 2011) changes. Only at the edges of the capability of satellite methods is there is some evidence that short-term (∼10 days), spatially confined (∼kilometres) dynamic variability due to hydrologic behaviour can be detected (Joughin et al., 2013; Palmer et al., 2011). A desire to better observe and understand the spatially distributed nature of ice sheet hydro-dynamics motivates the continued development of new methods for assessing glacier velocity.

Table 2.1 A comparison of methods for measuring ice motion. Expanded and updated from initial table presented by Doyle (2014).

Technique	Advantages	Disadvantages	Example studies
Field Techniques			
Theodolite / Electronic distance meter (EDM)	Line-of-sight surveys of multiple sites without having to traverse glacier.	Requires user to be in the field with good visibility.	Gudmundsson et al. (2000); Harper et al. (2007)
Repeat surveys (GPS)	High-accuracy. Can survey multiple sites with one GPS.	Requires user to be in the field and to visit each specific site.	Flowers et al. (2016); Hagen et al. (2005)
Continuously operating GPS	Automated collection. High sampling frequency and high precision.	High precision requires dual-frequency post-processing. High cost. Potential equipment failure.	Doyle et al. (2014, 2015); Tedstone et al. (2013)
Terrestrial Radar Interferometer	High precision and sampling frequency.	High cost. Large data files. True velocities determined indirectly from line-of-sight velocities.	Voytenko et al. (2017, 2015)
LiDAR	High precision and sampling frequency.	High cost. Large data files.	Schwalbe et al. (2008); Telling et al. (2017)

Table 2.1 A comparison of methods for measuring ice motion (*continued*).

Technique	Advantages	Disadvantages	Example studies
Remote Sensing			
Optical feature tracking	Large spatial coverage. Global automated datasets now available. Freely available datasets.	Low spatial and temporal resolution. Unusable in darkness or cloud cover.	Tedstone et al. (2015); Williams et al. (2020)
SAR (Speckle tracking and InSAR)	Large spatial coverage. Unaffected by cloud. Can also extract vertical changes. Freely available datasets.	Low spatial and temporal resolution. Disrupted by changing surface water. Non-trivial preprocessing required.	Joughin et al. (2018); Mouginot et al. (2019b)
Photogrammetry			
Terrestrial time lapse	Automated collection and high sampling frequency.	Potential equipment failure. Specific viewing geometry requirements limit use cases.	Messerli and Grinsted (2015); Schwalbe and Maas (2017)
Aerial	High spatial resolution. Potential for historic analysis.	High costs limit frequent or opportunistic surveys.	Brecher (1986); Kääb et al. (1997)
UAV	High spatial resolution and high sampling frequency compared to other remote sensing methods. Low cost.	Requires user to be in the field. GPS surveying or postprocessing for accurate geolocation.	Kraaijenbrink et al. (2016a); Ryan et al. (2015)

2.2.3 Recent glaciological applications of UAVs and SfM-MVS

Given the context of the above methods of evaluating glacier motion, UAVs offer distinct advantages and limitations. A combination of increasing affordability, accessibility and ease of use, and high-resolution output data mean that UAVs provide key advantages over traditional remote sensing platforms in a number of glaciological use cases. Unlike satellites, UAVs are not limited by set repeat times, and can be flown on-demand during the course of a field campaign. Although, like optical satellite imagery, they are limited by certain weather conditions (e.g. high winds or low cloud), they can collect usable data in a wider range of conditions, such as being able to fly underneath cloud. Collected data is very high resolution, up to cm-scale depending on flight altitude, which is higher than all commercial satellite options. The base UAV-SfM product, the 3-D point cloud, contains both spectral and topographic information as standard, whereas optical satellite data requires further stereophotogrammetric postprocessing in order to produce DEMs. Compared to DEMs stored as rasters, point clouds that have been obtained with good viewing geometries also have the advantage that they can store multiple elevation values at a single XY coordinate, allowing for complex ice geometry such as overhanging ice cliffs or calving fronts to be observed (Watson et al., 2017). UAVs, being highly manoeuvrable, are particularly suitable for obtaining a range of photogrammetric camera viewing geometries that can obtain information from both horizontal (ice surface) and vertical (ice cliff/calving front) surfaces, whereas ground-based observations, such as time-lapse cameras, LiDAR, and TRI, are best at observing vertical surfaces and may contain significant data gaps and shadows over relatively flat regions. However, UAVs are a time-intensive data collection platform, requiring active logistics to operate (e.g. launches/landings), whereas all other methods can collect data passively with little to no intervention. Compared to satellites, UAVs operate over smaller survey areas, and in some cases (for instance, when high spatial resolution requirements mandate low flight altitudes) may be limited to as small an area as 100 m^2. Although more complex fixed-wing hardware running from lithium-ion batteries can operate over significantly larger study areas (Jouvet et al., 2019), this requires a parallel increase in operating complexity. At the far end of this spectrum, there is a potential to use high altitude, long endurance (HALE) UAVs that can function for days at a time to observe, as have been used to study atmospheric chemistry

(Stutz et al., 2017). However, these technologies are far removed from the principle of UAVs as a low-cost, accessible platform for glaciology, reintroducing logistic and capital requirements normally associated with aircraft data collection.

A comprehensive history of the use of UAVs in glaciology has been published by Bhardwaj et al. (2016). However, even since this review, the use of UAVs has continued to grow, being exploited in nearly every aspect of field glaciology in applications as wide-ranging as: measuring surface mass loss (Bash and Moorman, 2020; Brun et al., 2016; Seier et al., 2017); classifying supraglacial features (Azzoni et al., 2018; Kraaijenbrink et al., 2016b; Smith et al., 2017); measuring albedo (Burkhart et al., 2017; Ryan et al., 2017, 2018) and surface temperature (Kraaijenbrink et al., 2018); mapping glacial geomorphology (Dąbski et al., 2017; Ely et al., 2016; Midgley et al., 2018; Tonkin et al., 2016; Westoby et al., 2016); and as an input for modelling studies (Ragettli et al., 2015).

The earliest example of deriving glacier velocity fields from 'contemporary' (i.e. low-cost, off-the-shelf) UAVs assessed the velocities of valley glaciers through the manual feature tracking of visible features, which were then interpolated into a continuous velocity field (Immerzeel et al., 2014; Whitehead et al., 2013). However, it is now standard to use automated feature tracking as commonly applied to satellite imagery (Section 2.2.2), which has been used to produce velocity fields for glaciers in the Alps (Seier et al., 2017), the Himalaya (Kraaijenbrink et al., 2016a), and the Peruvian Andes (Wigmore and Mark, 2017). The first use in Greenland was by Ryan et al. (2015), who used a fixed-wing UAV to assess ice velocity and flux at the calving front of Store Glacier. This was followed by similar applications at Bowdoin Glacier (Jouvet et al., 2018, 2017), where links were made between short-term variations in ice velocity and iceberg calving and plume activity. As UAVs have become established as a method, they have also been used as ground validation in a SAR-based study at Eqip Sermia (Rohner et al., 2019). It is significant that all of the above studies make use of GCPs to geolocate models in the SfM process. As a result, Greenlandic studies have been limited to operation at the glacier calving front, where exposed bedrock can provide stable ground control - although only at the margins of the survey zone. Ultimately, then, the logistical constraints of glaciological work often necessitate working with a sub-optimal GCP network that can contribute significant error to the final SfM-MVS product. Ice velocities are particularly sensitive, as by their nature they contain errors

propagated through two separate photogrammetric datasets. As a result, 'inland' studies (located away from the calving front and stable bedrock) are limited to non-dynamic applications where metre-scale geolocation errors are permissable, such as albedo studies (Cook et al., 2020; Ryan et al., 2017, 2018; Tedstone et al., 2020). This current limitation motivates the development of an alternative workflow suitable for deriving glacier velocity fields even where stable ground control is not available.

2.3 Summary of Motivations

In light of the state of knowledge presented in this chapter, there are some specific unknowns in the hydrology of the Greenland Ice Sheet that this thesis can aim to address. In particular, they are: (i) the extent to which hydro-dynamics at marine-terminating outlet glaciers in Greenland bear resemblance to those at land-terminating glaciers; (ii) to what extent the nature of hydro-dynamic response in the ablation-zone of ice sheets is spatially heterogeneous at scales beneath that visible in satellite imagery; and (iii) the nature and style of meltwater delivery to the bed via crevasses.

UAVs are well-posed to address these research questions, as they are efficient at collecting data in regions that are otherwise difficult to access by traditional field techniques (i.e. heavily crevassed regions of marine-terminating outlet glaciers). Additionally, they have been shown to be effective at producing velocity field observations at higher spatio-temporal resolutions than possible with satellite-derived data. UAVs have not previously been applied in the interior of ice sheets due to the challenge of accurately geolocating data obtained away from stable bedrock that provides opportunity for ground control. Hence, this thesis begins by developing and validating an alternative workflow for producing accurate glacier velocity fields (Chapter 3), before assessing the link between glacier hydrology and dynamics in two different contexts. The first context is during a rapid supraglacial lake drainage (Chapter 4). Here, a strong dynamic response can be used to assess the spatial heterogeneity of hydro-dynamic interaction. Additionally, a well-established series of studies of lake drainage in land-terminating sectors allows the identification of distinct (and comparable) features of lake drainage

in a marine-terminating environment. The second context is over a crevasse field (Chapter 5). Here, UAVs can be used to assess crevasse hydrology and links to the ice surface stress regime in a region that would be inaccessible to conventional field techniques, and at a higher resolution than satellite methods. This understanding is upscaled by pairing with satellite data at a regional scale in order to better understand the spatial variation, and controls on, crevasse hydrology in fast-flowing regions of the GrIS.

Chapter 3

Results I: Developing directly georeferenced UAV photogrammetry for ice sheets

Chapter published in **The Cryosphere**, March 2019

Citation Chudley, T. R., Christoffersen, P., Doyle, S. H., Abellan, A., & Snooke, N. (2019). **High-accuracy UAV photogrammetry of ice sheet dynamics with no ground control.** *The Cryosphere*, 13(3), 955–968. https://doi.org/10.5194/tc-13-955-2019

Contributions Tom Chudley and Poul Christoffersen designed the study. Tom Chudley designed the UAV payload, built the UAVs, processed the GPS rover data, and processed and analysed the photogrammetry data. Sam Doyle advised on GPS techniques, collected and processed the GPS reference and base station data, and assisted with GPS rover processing. Antonio Abellan assisted with flight path design and photogrammetric processing. Neal Snooke originally designed the UAV and helped to build the units used in this study. Tom Chudley wrote the paper with input from all authors. Guillaume Jouvet and Oliver Wigmore reviewed this manuscript for *The Cryosphere*.

Abstract

Uncrewed aerial vehicles (UAVs) and structure from motion with multi-view stereo (SfM–MVS) photogrammetry are increasingly common tools for geoscience applications, but final product accuracy can be significantly diminished in the absence of a dense and well-distributed network of ground control points (GCPs). This is problematic in inaccessible or hazardous field environments, including highly crevassed glaciers, where implementing suitable GCP networks would be logistically difficult if not impossible. To overcome this challenge, we present an alternative geolocation approach known as GNSS-supported aerial triangulation (GNSS-AT). Here, an on-board carrier-phase GNSS receiver is used to determine the location of photo acquisi- tions using kinematic differential carrier-phase positioning. The camera positions can be used as the geospatial input to the photogrammetry process. We describe the implementation of this method in a low-cost, custom-built UAV and apply the method in a glaciological setting at Store Glacier in western Greenland. We validate the technique at the calving front, achieving topographic uncertainties of $\pm$0.12m horizontally ($\sim$1.1 $\times$ the ground sampling distance) and $\pm$0.14 m vertically ($\sim$1.3 $\times$ the ground sampling distance), when flying at an altitude of $\sim$ 450 m above ground level. This compares favourably with previous GCP-derived uncertainties in glacial environments and allows us to apply the SfM–MVS photogrammetry at an inland study site where ice flows at 2 m day^{-1} and stable ground control is not available. Here, we were able to produce, without the use of GCPs, the first UAV-derived velocity fields of an ice sheet interior. Given the growing use of UAVs and SfM–MVS in glaciology and the geosciences, GNSS-AT will be of interest to those wishing to use UAV photogrammetry to obtain high- precision measurements of topographic change in contexts where GCP collection is logistically constrained.

3.1 Introduction

In recent years, Uncrewed Aerial Vehicles (UAVs) have emerged as a versatile and practical tool for aerial surveying. A common application of this method that holds particular promise in the geosciences is the production of 3-D topographic models from sequential 2-D imagery using Structure from Motion with

Multi-View Stereo (SfM-MVS) photogrammetry (Eltner et al., 2016; Fonstad et al., 2013; Westoby et al., 2012). With repeat surveys enabled through flight autonomy, SfM-MVS is creating new opportunities for the study of terrain evolution in 4-D (James et al., 2017). The technique compliments, and provides key advantages over, satellite-based earth observation methods, which have larger spatial coverage but lower spatial resolution, as well as an inherent trade off between spatial and temporal resolution in many applications. With a relatively low barrier of entry in terms of cost, UAV-derived photogrammetry is rapidly advancing and the versatility of the technique provides new avenues of research using additional image processing methods or on-board sensors, many of which have yet to be explored. UAV-SfM has become an increasingly used tool within the cryospheric sciences (see Bhardwaj et al., 2016), in particular through the application of feature-tracking methods to multitemporal datasets in order to produce velocity datasets in glacial environments as diverse as the Himalaya (Immerzeel et al., 2014; Kraaijenbrink et al., 2016a), Alps (Seier et al., 2017), Peruvian Andes (Wigmore and Mark, 2017), and the Greenland Ice Sheet (Jouvet et al., 2018, 2017; Ryan et al., 2015).

While UAV-derived photogrammetry offers key advantages over conventional surveying techniques in studies of 4D topographic change, the dependency on ground control points (GCPs) is often impractical, yet necessary to scale and orient photogrammetric models to a real coordinate system (Carrivick et al., 2016; James and Robson, 2014). Previous work has shown that the quantity and distribution of GCPs can have a significant impact on the final accuracy of the photogrammetric products: for example, topographic error has been shown to increase if the number of GCPs is decreased and spacing between GCPs increases (James and Robson, 2014; Johnson et al., 2014; Shahbazi et al., 2015; Tahar, 2013; Tonkin and Midgley, 2016). Accuracy assessments performed specifically for a glaciological environment report that for a ground sampling distance (GSD) of $\sim$6 cm, local accuracy decreases with the distance to the closest GCP at a rate of about 0.09 m per 100 m (Gindraux et al., 2017). Additionally, Gindraux et al. (2017) report an optimal GCP distribution density (i.e. beyond which no improvement in accuracy is observed for their GSD) of 7 GCP km^{-2} for horizontal accuracy and 17 GCP km^{-2} for vertical accuracy. Producing a GCP network of this density in glacial terrain can be impractical, logistically-expensive to collect, and often unfeasible – as well as limiting one of the inherent advantages of UAVs in being able to re-

motely and accurately observe terrain which is difficult and hazardous to access on the ground. The difficulties of producing these networks can be observed in applied glaciological studies, where GCPs are often located only along the valley sides near a glacier's lateral margin (e.g. Immerzeel et al., 2014; Ryan et al., 2015). On-ice GCPs, if used, require repeat surveying as GCPs continuously advect with the glacier's flow. On fast-flowing glaciers (surface velocities of metres per day), these changes are so rapid that GCP collection would need to be nearly contemporaneous with image acquisition to be effective for accurate geolocation – a requirement which is unfeasible for these glaciers due to crevasses forming on their surface. As a result of the difficulties in building GCP networks in glacial environments, alternative methods are often applied to externally constrain photogrammetric products. Such methods include using tie points to tie datasets together geodetically (Kraaijenbrink et al., 2016a); linearly interpolating the on-ice GCP location from the beginning and end of a UAV campaign (Jouvet et al., 2017); or providing some additional external constraint using an on-board navigational GPS geolocation (Jouvet et al., 2017; Ryan et al., 2015). The practical limitations of GCP collection is one of the most limiting factors in UAV-derived photogrammetry in the geosciences, especially in glaciological studies, where errors to date have been systematically larger than what is theoretically possible with this technique. Furthermore, these limitations have meant that no one has, to date, succeeded in using UAV-based methods to derive 4D surface evolution and velocity fields away from an ice sheet margin, where topographic ground-control is especially scarce and often lacking altogether.

Recent developments in lightweight, low-cost GNSS technology have allowed for the proliferation of a new technique whereby differential carrier-phase GNSS positioning is used to accurately geolocate imagery and subsequent photogrammetric products. This technique, known as GNSS-supported aerial triangulation (GNSS-AT; Benassi et al., 2017), has been shown to result in sub-GSD horizontal accuracy without the use of GCPs (Benassi et al., 2017; Fazeli et al., 2016; Hugenholtz et al., 2016; Mian et al., 2015; van der Sluijs et al., 2018). Published applications of this technique in the geosciences are so far limited (Strick et al., 2018; van der Sluijs et al., 2018), and no studies yet examine the appropriateness of this technique for the study of glacial dynamics.

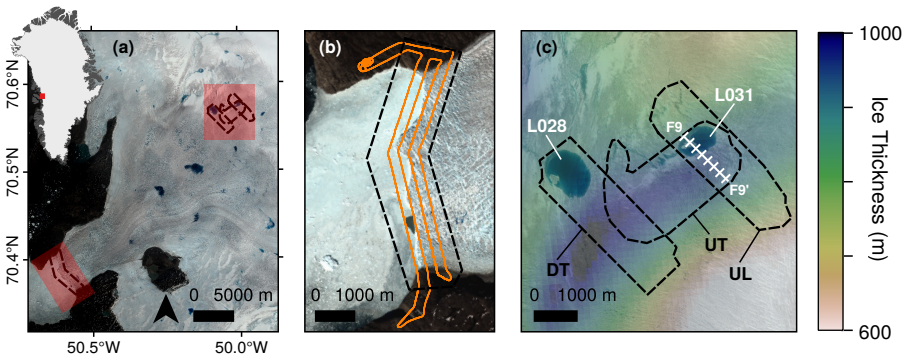

Fig. 3.1 Location of study sites. (a) Store Glacier with calving front and inland study sites highlighted. Inset: location of Store Glacier in Greenland. (b) Calving front flight zone with example flight path shown. (c) Inland flight zones with labelled names: downstream transverse (DT), upstream longitudinal (UL), and upstream transverse (UT). Transect F9 marks location of Figure 3.9. Ice thickness from BedMachine v3 (Morlighem et al., 2017) is overlaid, and supraglacial lakes at the inland study site (L028 and L031) are also labelled.

The aim of this paper is to: (i) apply GNSS-AT using a low-cost, custom-built airframe suitable for the study of extreme environments; (ii) develop and describe modifications to the GNSS-AT process to allow surveys to be undertaken at inland ice sheet location far from suitable GPS reference stations; and (iii) validate the method for the study of glacier dynamics. Here, we demonstrate the suitability of GNSS-AT assisted UAV photogrammetry for assessing glacier dynamics using examples from two specific settings where on-ice GCPs are not feasible. The first is the glacier's calving terminus, where deep fractures prohibit access, and bedrock exposure allows method uncertainty to be quantified; the second is the interior ice sheet where there is no exposed bedrock and therefore distributed ground control is prohibitively difficult.

3.2 Methods

3.2.1 Study site

Store Glacier (*Sermeq Kujalleq*, 70.4° N 50.6° W) is a marine-terminating outlet glacier in West Greenland. The third-fastest outlet glacier in Greenland, it has a 5.2 km wide calving front draining a ~34,000 km^2 catchment (Rignot et al., 2008).

The terminus of Store Glacier has been located in approximately the same position since at least 1948 (Weidick, 1995), likely due to the presence of a prominent basal pinning point and the position of the terminus at a lateral valley constriction (Todd et al., 2018). The calving front of Store Glacier also marks the study site of a previous application of UAVs to the study of glacial dynamics in Greenland by Ryan et al. (2015). Store's ice catchment extends 280 km from the calving front (Todd et al., 2018), and is underlain by an active subglacial hydrological system extending at least 30 km inland.

We surveyed two locations on Store Glacier: (i) at the calving front of Store, and (ii) at an on-ice site 30 km inland (Figure 3.1). Our flights at the calving front were designed to test the GNSS-AT method, with exposed bedrock at the sides of the calving front providing good ground control for validation and error quantification. The location of our primary inland flight zones were motivated by a subglacial bedrock trough visible in Bedmachine v3 data (Morlighem et al., 2017), which our flights profile longitudinally and transversely (Figure 3.1c).

3.2.2 UAV platform and flight planning

We used a Skywalker X8 UAV (Figure 3.2a; Appendex A, Figure A.1), an off-the-shelf fixed-wing air frame with a 2.12 m wingspan (Jouvet et al., 2017; Ryan et al., 2015). In a setup similar to the one used by Jouvet et al. (2017), we use open hardware "PixHawk" autopilot (https://pixhawk.org/) and APM Arduplane firmware (http://ardupilot.org/plane/) for flight control along a pre-programmed flight path. The UAV is capable of $\sim$1 hour of flight time at a $\sim$60 km h^{-1} cruising speed, although given our use case in an extreme environment, we flew conservatively for no more than 40 minutes. The total scientific payload weighs 500 g. This includes a nadir mounted Sony α6000 24 MP camera with fixed 16 mm lens. To allow for direct georeferencing of each photo location, we included an on-board lightweight L1 carrier-phase GNSS receiver (an Emlid Reach, using a small Tallysman TW4721 antenna with a 100mm ground plane). The GNSS receiver was powered by the PixHawk autopilot, and recorded camera trigger events in the output RINEX data via a hot shoe trigger cable linked to the camera. The cost of a complete flight unit (including frame, hardware, and scientific payload) was approximately $\sim$£1500 per unit. Further necessary ground equipment, which could

be shared between units, came to ∼£300: this includes the radio transmitter and lithium polymer battery charger, but not the ground-based GPS (sections 3.2.3, 3.4.3).

The UAV flew autonomously along pre-defined flight routes designed on-site using Ardupilot's Mission Planner software. The 5m ArcticDEM mosaic (Porter et al., 2018) was used to assist with the flight path design, ensuring a constant relative altitude over the glacier and avoiding collision with high relief topography at the glacier margins. For each flight, the UAV flew a route autonomously at a relative altitude of ∼450 m above ground level (a.g.l.), resulting in a ground-level footprint of ∼660 x 440 m and a GSD of ∼11 cm. Our camera was set to autofocus, and a fixed f-stop and ISO (between f/4–f/8 and ISO 100-400 respectively depending on lighting conditions) chosen to target an auto shutter speed of 1/1000 s. Photos were recorded in RAW format to ensure lossless storage of images, and converted into Photoscan-compatible 16-bit tiffs before processing. Flight lines were spaced ∼250 m apart and the camera was set to trigger every ∼80 m, typically acquiring ∼300 images in an average flight. These parameters ensured adequate overlap in the photographs for photogrammetry purposes, targeting 80% in the flight direction and 60% in the cross-flight direction. Flight paths in the ice sheet interior, where flight endurance allowed, also included a lower-altitude ∼200 m along-track flightline with sharp banking turns designed to obtain imagery from multiple elevations and oblique angles. The aim of these lower-level flights was to reduce the potential vertical 'doming' effect on reconstructed surface topography that can occur when using self-calibrating bundle adjustment with image sets consisting of solely near-parallel viewing directions (James and Robson, 2014; James et al., 2017; Nesbit and Hugenholtz, 2019).

3.2.3 GNSS-supported aerial triangulation

The block orientation process of SfM-MVS photogrammetry can be performed in two main ways (Benassi et al., 2017). The first is Indirect Sensor Orientation (InSO), where ground-based GCPs provide external constraints. The second is Direct Sensor Orientation (DSO, sometimes referred to as 'direct georeferencing'), where external orientation parameters are provided by on-board systems including GNSS and an inertial measurement unit (IMU). Full DSO combines camera

orientation data (e.g. from the IMU) with accurate camera location data from a GNSS receiver (see Cucci et al., 2017). Although DSO is not a new method for aerial photogrammetry (e.g. Blankenberg, 1992), InSO based methods have prevailed in UAV-based surveying, as the inexpensive navigational GNSS and IMU equipped in standard commercial UAVs are not accurate enough to provide more than metre-scale accuracy (James et al., 2017). Recently, commercial off-the shelf UAV units with DSO capability have become available, although these remain expensive, often in excess of £20,000 for fixed-wing units at the time of writing. Here, we take advantage of the recent availability of low-cost, light-weight carrier-phase GNSS recievers to implement direct orientation for the first time in a glaciological study. The implementation described in this study is a subset of DSO referred to as GNSS-supported Aerial Triangulation (GNSS-AT), which requires GNSS data but not IMU data (Benassi et al., 2017). GNSS-AT is therefore well-suited to UAV applications where IMU data is not available or not accurate enough (e.g. where IMU data is limited to that from lower-quality navigational units). GNSS-AT does, however, require position data that is more accurate than that provided by the GNSS receivers typically used for UAV navigation which use the Standard Positioning Service (SPS). Higher positioning accuracy than is offered by the SPS can be achieved by using differential carrier phase positioning, which makes use of the ability of GNSS receivers to measure the carrier phase to one hundredth of a cycle, equivalent to about 2 mm in distance (Leick, 2004).

To obtain accurate camera positions we kinematically post-processed 5 Hz data logged by the on-board L1 carrier-phase GNSS receiver. Data were post-processed using the differential carrier phase kinematic program within Emlid's b27 fork of RTKLIB v. 2.4.3 software relative to a base station located at the launch site. Single-frequency receivers such as the Emlid Reach can be used for differential carrier-phase positioning for baselines on the order of kilometres – distances over which the differential ionospheric delay is negligible. To apply differential corrections over the longer baselines as is often necessary in glacial environments, dual-frequency (L1/L2) receivers must be used to cancel out the frequency-dependent ionospheric delay. As dual-frequency GNSS receivers suitable for integrating in to the UAV were not available at the time of the survey (see section 3.4.3) we use single-frequency carrier phase positioning to determine the camera position ('R' in Figure 3.2c) relative to a nearby base station ('B_1'), and dual-frequency carrier-phase positioning to determine the absolute position of the base station ('B_1') rela-

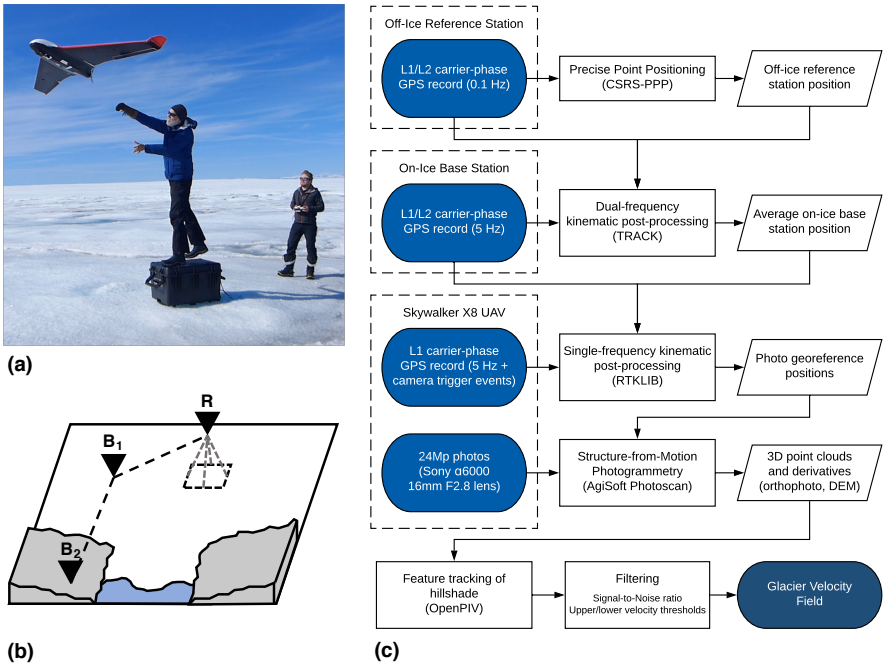

Fig. 3.2 The method used in this study: (a) Launching the Skywalker X8 on the ice sheet; (b) cartoon visualising the relationship of kinematic GPS corrections between the UAV rover (R), on-ice launch site base station (B_1), and the off-ice reference station (B_2); and (c) flowchart showing the workflow used in this study to derive photogrammetry products and velocity fields at the inland study site.

tive to a bedrock-mounted reference station ('B_2'). This method has the limitation that the UAV must stay within 10 km of the launch site base station, which may be located on or off the ice, but allows the launch site base station, and therefore the UAV flight, to be located long distances away from the bedrock-mounted reference station. In this study, our base station (B1) was a Trimble R9s GNSS receiver (with Zephyr 3 antenna) located at the launch site, and the bedrock-mounted reference station was a continuously-operating Trimble NetR9 GNSS receiver (with Zephyr 3 Geodetic antenna) recording at 0.1 Hz located at Qarassap Nunata (70.4° N, 50.7° W), a mountain ridge near Store Glacier's calving front. For practical reasons and redundancy, we used this three-receiver set-up for all flights including those at the calving front, however, only one of the dual-frequency receivers was strictly required for flights at the calving front, where a bedrock-mounted base station was located nearby.

Whilst the Emlid Reach GNSS receiver is capable of real-time kinematic (RTK) correction, we used instead post-processed kinematic (PPK) positioning for three

primary reasons. First, PPK does not rely on maintaining a reliable real-time radio link with a GNSS base station, which would introduce additional technical constraints. Second, PPK solutions are also often more accurate than RTK solutions as precise ephemeris data for the GNSS satellites is available during post processing. Third, absolute positioning using RTK requires a stationary reference station with a known position, which is not possible in real time on an advecting ice surface.

The overall workflow for photogrammetric reconstruction and for the generation of the glacier velocity field is illustrated in Figure 3.2c. First, the position of the Qarassap Nunata reference station was estimated using the average of 17 days of data collected at 0.1 Hz and processed with Precise Point Positioning (PPP) using the Natural Resources Canada Precise Point Positioning service (webapp.geod.nrcan.gc.ca/geod/tools-outils/ppp.php). Second, the position of the launch site base station was determined and for this two different methods were used depending on whether the base station was located on or off the ice. Where the base station was located on bedrock its position was determined using static differential carrier-phase positioning within RTKLIB 2.4.3 software. For flights at the ice sheet interior, the launch site base station was moving at approximately 1.5 m d^{-1}. We therefore processed this data kinematically (King, 2004) using the differential carrier phase positioning software Track v1.30 (Chen, 1998, http://geoweb.mit.edu/gg/). All GNSS processing used final precise ephemeris products from the International GNSS Service (Dow et al., 2009). We took the average position of the base station over the flight time as the absolute reference location. During the ∼20 minute flight period the base station could have moved by up to ∼2 cm, introducing a systematic error into the final calculated photo location. Given the small magnitude of this error relative to larger errors later in the workflow, we assume the interior base station data during the flight can be treated as stationary for post-processing purposes. Finally, we post-process the UAV-based data kinematically against the launch site base station data using Emlid's RTKLIB 2.4.3 b27 fork. The Emlid RTKLIB fork provides final photo geolocation using the GPS time of the camera trigger marker in the RINEX data by linearly interpolating between the two closest points of the 5 Hz record. RTKLIB canera location outputs are estimated to have standard deviations ∼0.6 mm horizontally and ∼1.1 mm vertically for fixed solution data.

3.2.4 SfM-MVS photogrammetry and feature tracking

SfM-MVS photogrammetry was performed with AgiSoft Photoscan (version 1.3.3; http://www.agisoft.com), using the determined camera positions in the input process. As geolocation was accurate to within millimetres, it was also necessary to include the directional offset between the receiver antenna and camera position (-7.9 cm in the Y direction and +13.2 cm in the Z direction relative to the lens of the camera) to properly locate camera centre points. Camera calibration was performed automatically in the bundle adjustment process, which is the preferred option when other variables of the bundle adjustment are well constrained. From the final dense point clouds, we produce orthophotos at 0.15 m resolution and geoid-corrected DEMs at 0.2 m resolution based on recommended output resolutions from Photoscan.

We produced horizontal velocity fields by feature tracking 0.2 m resolution multidirectional hillshade models produced from the DEMs using GDAL 2.2. Using DEM-derived products has the disadvantage of having a slightly lower resolution than an orthophoto, but the advantage of being consistently comparable when tracking datasets collected in variable lighting conditions. In particular, orthophotos acquired at different times of the day can complicate feature tracking due to the variation in shadow directions (cf. Jouvet et al., 2017). To feature track images, we used OpenPIV (Taylor et al., 2010), an open-source particle image velocimetry software implemented in MATLAB. Following a sensitivity analysis, we chose an optimal interrogation window size of 320x320 pixels and a spacing of 32 pixels, resulting in a final resolution of 6.4 m. After the production of the velocity field, we filtered erroneous values using manually chosen upper and lower thresholds for both velocity and signal-to-noise ratio (SNR) - generally between 0.8-1.1 at the lower bound and 2.8-3.5 at the upper bound.

3.2.5 Uncertainty assessment

Relative uncertainties were calculated by assessing inter-DEM variation in the elevation of the exposed bedrock on Qarassap Nunata near the calving front, assuming no expected change in topography. Vertical uncertainty (s_z) was calculated by assessing the mean per-pixel standard deviation from the mean elevation of the

repeat DEMs. Horizontal uncertainty (s_{xy}) was estimated using feature-tracked displacement fields. First, we calculate the root mean square error in displacement fields (s_{RMSE}) produced in the feature tracking process (Ryan et al., 2015). We assume that this value results from the combined error from the root mean square error of the two tracked images. Hence, we estimate the horizontal uncertainty (s_{xy}) as follows:

$$s_{xy} = \sqrt{\frac{s_{RMSE}^2}{2}} \tag{3.1}$$

Note that this estimate ignores potential error contributions from feature tracking in s_{RMSE}, and hence likely only provides an upper bound on the horizontal uncertainty.

From s_{RMSE}, we can also calculate the uncertainty of any horizontal velocity field (s_v) as follows:

$$s_v = \frac{s_{RMSE}}{\Delta t} \tag{3.2}$$

where Δt is the time interval of the velocity field.

As our external orientation parameters (camera positions) are distributed densely, consistently, and evenly throughout the point cloud (cf. a GCP-based network), we assume that error is spatially non-variable, and hence that uncertainties measured at the bedrock margins are representative of error across the SfM-MVS product.

3.3 Results

3.3.1 Calving front

DEMs and velocity fields

The calving front of Store Glacier was surveyed ten times between 10th-14th July 2017 (Appendix A, Table A.1). Typical UAV-derived glaciological products for the

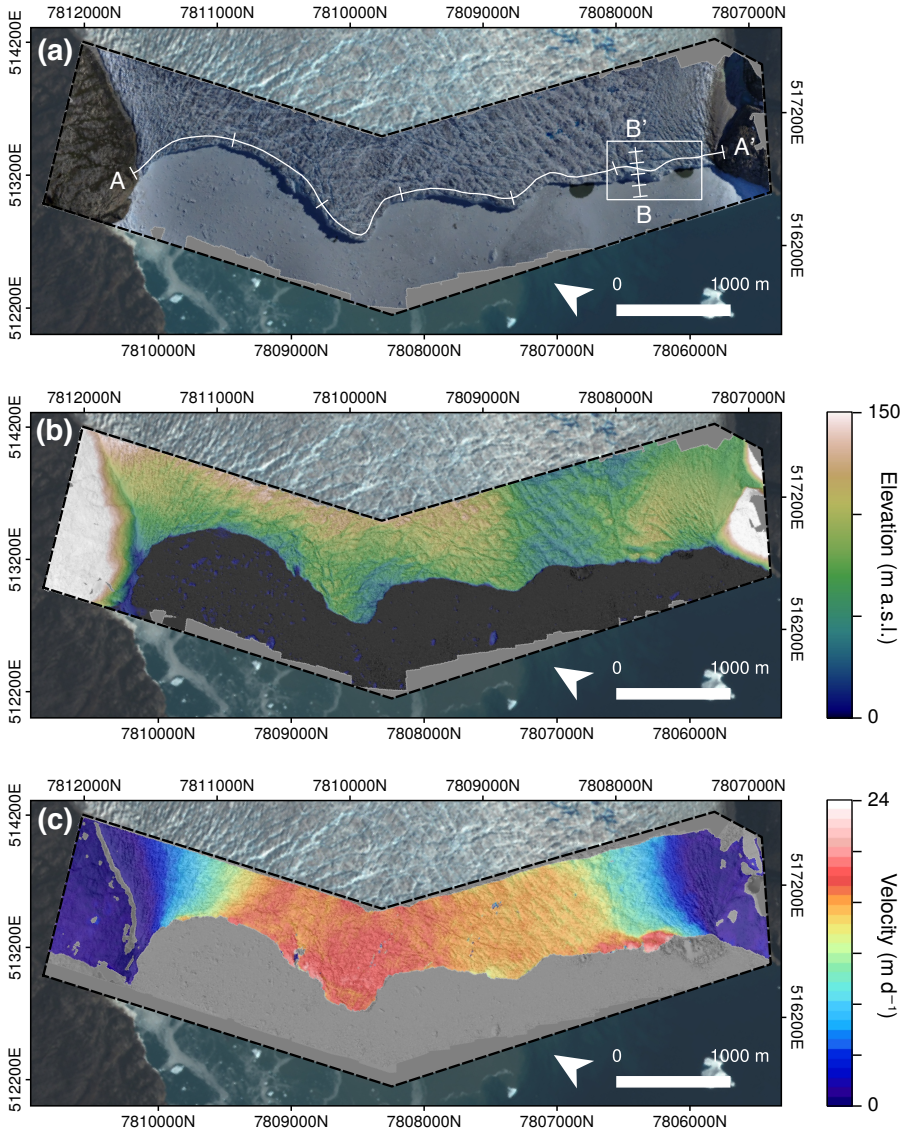

Fig. 3.3 Example data output from calving front. (a) 0.15 m orthophoto, collected 10:15 12th July 2017. (b) 0.2 m DEM from same flight. (c) 6-hour separation velocity field (s_v = ±0.69 m) from 16:15–22:15 on the 12th July. Transects in (a) refer to Figure 3.4. Box refers to location of Figure 3.5

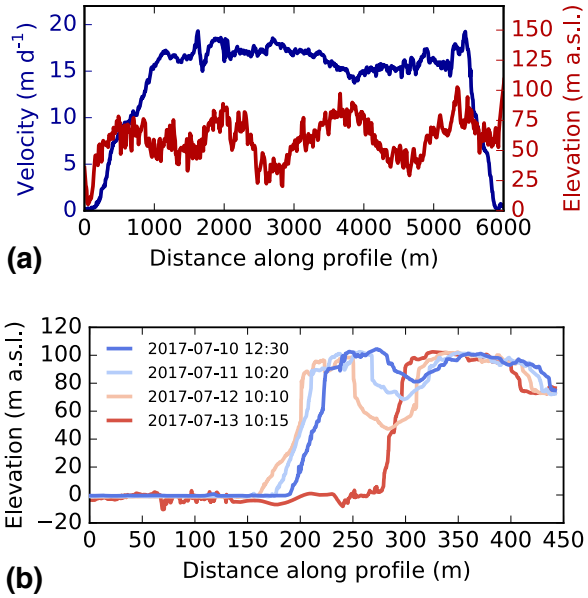

Fig. 3.4 (a) Transect of A-A′ in Figure 3.3(a), displaying velocity (blue) and elevation (red). (b) Transect of B-B′ in Figure 3.3(a), displaying elevation profiles of the calving front through the study period. A large-scale calving event occurs between the 12th and 13th of July.

calving front are shown in Figure 3.3, including orthophoto, DEM, and velocity field.

Our method reproduces both small- and large-scale aspects of the calving front in fine detail. At glacier-wide scales, the side of the calving front is known to have a prominent surface depression, an expression of a retreated grounding line and section of the front at floatation (e.g. Ryan et al., 2015; Todd et al., 2018). This is captured well by the GNSS-AT photogrammetry (Figure 3.3b; 3.4a). At local scales this method is accurate enough to capture the opening of crevasses over periods of days (Figure 3.4b; 3.5d–e), although reconstruction of crevasse depth continues to be problematic due to low illumination and inefficient sensor orientation within crevasses (Ryan et al., 2015).

The GNSS-AT method can also be successfully used to derive velocity fields of the calving front at high resolution and accuracy (Figure 3.3b; 3.4a). The velocity field, derived from displacements detected over a six-hour period between 16:15 and 22:15 on the 12th July 2017 (s_v = 0.69 m d^{-1}), shows that velocities are generally uniform (15 m d^{-1}) across much of the central calving front, with localised peaks

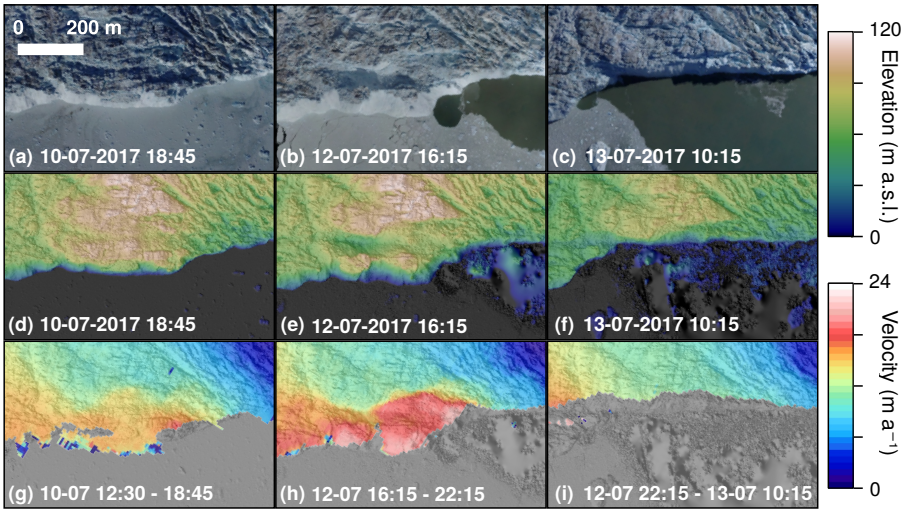

Fig. 3.5 Orthophotos (a–c), DEMs (d–f) and velocity fields (e–i) showing the lead-up and aftermath of a calving event that occurred on the south side of Store Glacier between 22:15 on the 12th July and 10:15 on the 13th July. Location is marked by outline in Figure 3.3a. NB. the poor reconstruction of open water visible in DEMs and hillshades of figures e, f, h, and i.

of 20 m d^{-1} (Figure 3.3c; 3.4a; 3.5h). Our method is sensitive to dynamic changes at the calving front: in particular, the areas of highest velocity at the very lip of the calving front – such as regions ∼1.8–2 km and ∼5.2–5.4 km along profile A (Figure 3.4) – all mark areas of ice that undergo calving events in the next 24–48 hours. One particular calving event, occurring between 22:15 on the 12th July and 10:15 on the 13th July on the southern side of Store Glacier, is detailed in Figures 3.4b and 3.5. The calving zone, measuring ∼150 000 m^2, occurs in a region of high shear strain in a region bordering the floating section of Store. More than 48 hours before calving, deformation in the calving zone is anomalous relative to the surrounding area: up to 20 m d^{-1}, whilst the region immediately behind the zone is <10 m d^{-1} (Figure 3.5g). Over the following two days, a plume becomes visible in front of the calving zone, opening up a region of open water in the ice melange (Figure 3.5a–b). The crevasse becomes deeper and wider during this time (Figure 3.4b): across transect B-B′ (Figure 3.3a), the crevasse increases from ∼57.5 m wide and ∼19.2 m deep at the first observation (2017-07-10 12:30) to ∼73.5 m wide and 49.6 m deep at the final observation before calving (2017-07-12 22:20). The crevasse is not obviously water filled in this period (Figure 3.5b), but is filled with ice debris that has dry calved off the interior face of the crevasses (Figure 3.4b; 3.5b), so

the depths are reported above are underestimated, and water may exist beneath the debris. In the hours prior to calving, the calving zone reaches deformation rates up to 24 m d^{-1} (Figure 3.5h). The calving event itself resulted in the loss of an ice section ~400 m in length extending ~100 from the front of the glacier. Assuming the calving front is at floatation in this region of the glacier front (Todd et al., 2018), we estimate from elevation models that the total ice lost to be 9.5 x 10^7 m^3 (~0.1 km^3). After calving, displacement rates at the glacier fronts return to levels consistent with the surrounding area (Figure 3.5i).

Uncertainty analysis

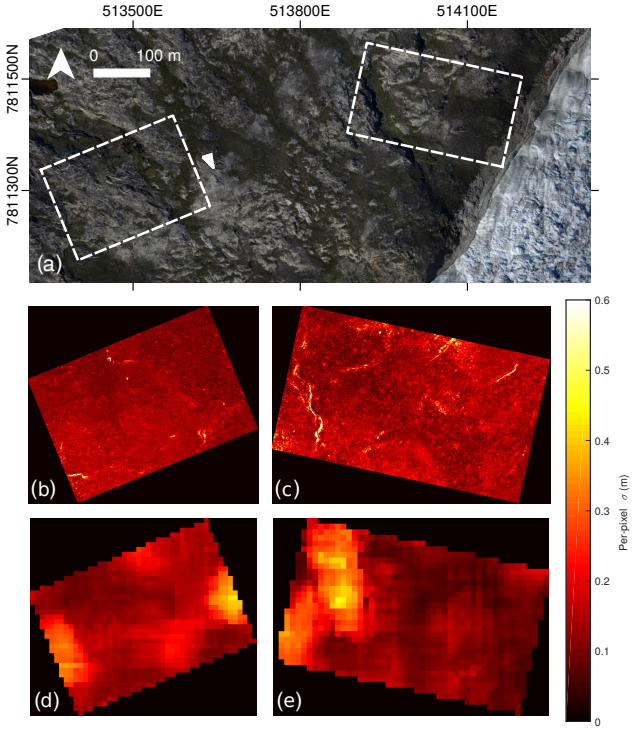

Fig. 3.6 Error assessment at the calving front: (a) location of two validation sites at the calving front shown on UAV-derived orthophoto; (b-c) standard deviation in Z axis derived from DEMs (d-e) standard deviation in XY axes derived from horizontal displacement fields.

To estimate the error of the technique, we sampled a total of 0.1 km^2 of bedrock across two zones close to the glacier margin where reconstruction quality matched that of the glacier surface across all DEMs (Figure 3.6a). We selected eight DEMs

and eight displacement fields of these sample areas, produced by feature tracking consecutive hillshaded DEMs.

The uncertainties derived from assessment of these DEMs is $s_z = \pm 0.14$ m and $s_{xy} = \pm 0.12$ m. This amounts to ∼1.1 times the GSD (∼11 cm) in the horizontal and ∼1.3 GSD in the vertical. The per-pixel standard deviation in the vertical axis (Figure 3.6b–c) shows that vertical deviation is relatively consistent across the image. The areas of highest deviation (visible as bright yellow-white bands in Figure 3.6c) are pixels that are located at steep topographic cliffs, where slopes are close to vertical and thus any horizontal error will compound the reported deviation in the vertical axis. The per-pixel standard deviations in the horizontal (Fig 3.6d–e) reveal clustered 'hotspot' regions of high variation. However, close inspection of individual displacement fields shows that these hotspots are an artefact of individual anomalies in the displacement fields, and that areas of high deviation are not spatially consistent between displacement fields. Hence, although horizontal uncertainty is spatially variable, the variability is not dependent on factors such as surface texture or roughness, which would invalidate the assumption that a single uncertainty value can be assigned uniformly to an entire DEM.

With a displacement uncertainty $s_{RMSE} = 0.17$ m (∼1.5 GSD) and the ability to capture ice flow accurately, even along the relatively slow moving (1-5 m d^{-1}) sides of the glacier calving front, these uncertainty tests validate our ability to use GNSS-AT derived UAV-photogrammetry to produce accurate DEMs and velocity fields of glacier motion.

3.3.2 Ice sheet interior

Because feature tracking is able to successfully track decimetre-scale displacements at the calving front, the same hardware and methodological approach should be sufficient to measure daily velocity in the ice sheet interior, even where there are no exposures of bedrock for GCPs and ice flow is considerably slower. The interior study area is located 30 km inland from the calving front, where ice flows at a speed of 2 m d^{-1}. The location of the flight paths was motivated by the presence of a large subglacial trough identified in BedMachine v3 data, and the presence of two supraglacial lakes 28 and 31 km inland (Lake 028 and Lake 031

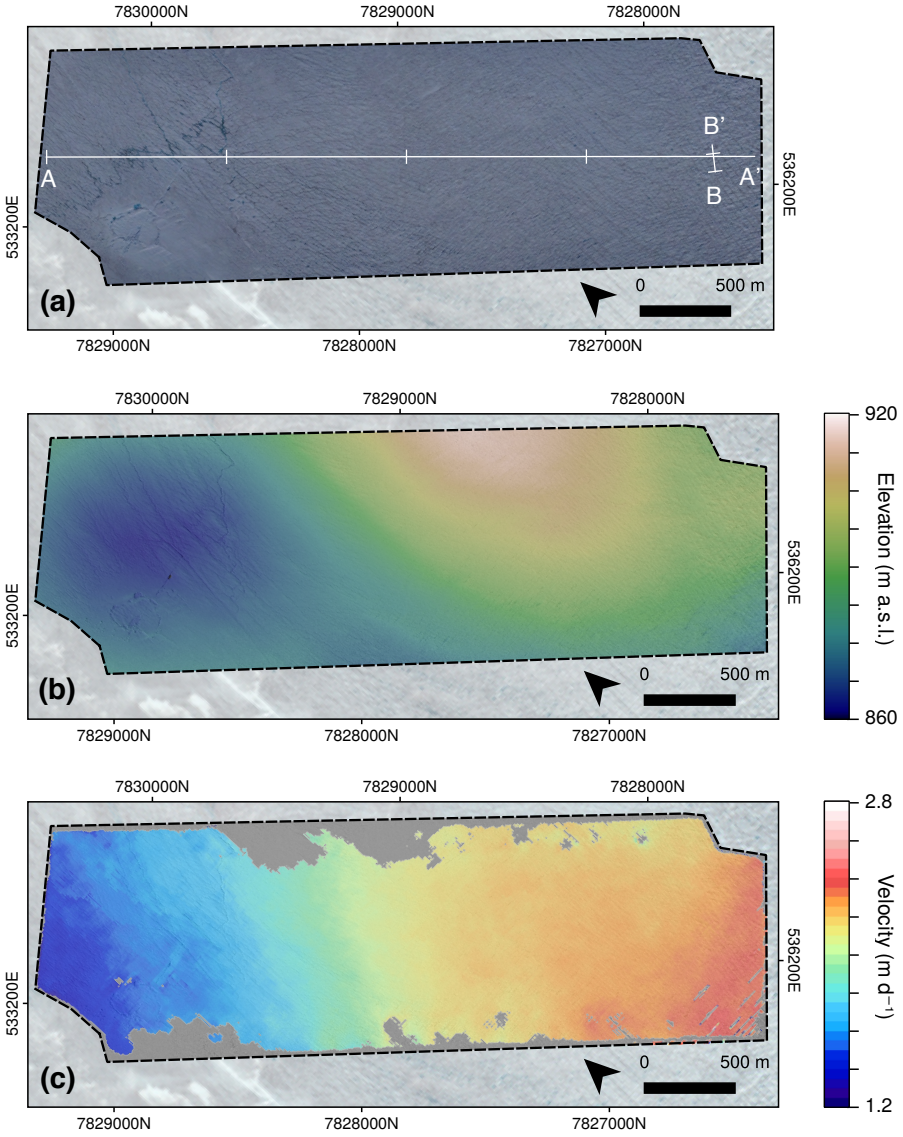

Fig. 3.7 Example data output from the ice sheet interior. (a) 0.15 m orthophoto collected 15:15 22nd July 2017. (b) 0.2 m DEM from the same flight. (c) Velocity field (s_v = $\pm$0.05 m) from 15:15 22nd – 19:30 26th July 2017

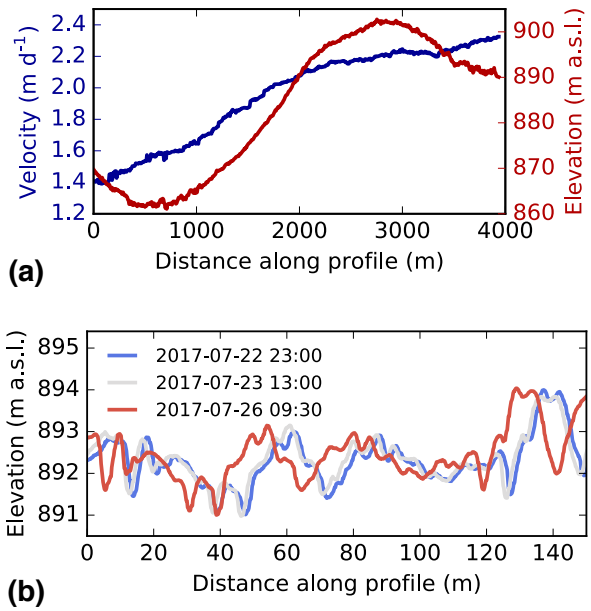

Fig. 3.8 (a) Transect of A-A' in Figure 3.7(a), displaying velocity (blue) and elevation (red). (b) Transect of B-B' in Figure 3.7(a), displaying elevation profiles of a crevasse field through the study period.

– see Figure 3.1c). Typical UAV-derived glaciological products for the ice sheet interior (flight zone 'DT' – see Figure 3.1c for location) are shown in Figure 3.7, including orthophoto, DEM, and velocity field.

Although flight zone DT was designed to capture Lake 028, it is apparent from orthoimagery that the lake had drained prior to the beginning of the study (Figure 3.7). Sentinel-2 imagery shows the drainage to occur between the 19th June and the 7th July, although Lake 031 remained filled during the study period. Lake 031 overflows into a supraglacial stream which terminates in a large (>10 m diameter) moulin formed from the hydrofracture of Lake 028. This distinct hydrological network is visible in the former lake bed (Figure 3.7a), which is clearly seen as a depression in the surface DEM produced by SfM-MVS (Figure 3.7b). Figures 3.7a–b capture two historical features of lake drainage. The first is the fracture and moulin from the 2017 lake drainage, as already described. The second is the remnant lake ice from the 2016 lake, which did not drain and is still visible as a lighter patch of ice in the western corner of Figure 3.7a.

Figure 3.7c shows a velocity field derived by feature tracking displacements on two DEM hillshades produced from orthophotos with four days separation, from

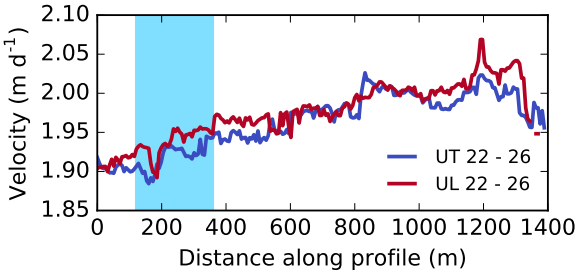

Fig. 3.9 Comparison between two velocity fields obtained from different flight paths at comparable times between the 22nd and 26th July 2017. Blue shading marks where the transect crosses Lake 031. Transect is visualised as transect F9 in Figure 3.1c.

22nd – 26th July 2017 (s_v = 0.05 m d^{-1}). To our knowledge, this represents the first published UAV-derived velocity field of an ice sheet interior, constructed without the use of GCPs. Feature-tracking has successfully reconstructed the full range of velocities across the interior region in which ice flow gradually increases from ~1.4 m d^{-1} in the west to ~2.4 m d^{-1} in the east (Figure 3.8a). We interpret this difference to occur due to differences in bedrock topography: to the southeast, ice is flowing over a bedrock rise, the peak of which is centred approximately 2 km southeast of the study region (Figure 3.1). This change in dynamics is expressed in the ice surface as an increasing frequency of deep and open crevasses (Figure 3.7a; 3.8b).

We can test the robustness of the inland surveys by comparing contemporaneous velocity fields from independent flights. Figure 3.9 shows a 1.4 km velocity profile of two velocity fields, constructed for the same time period (22nd – 26th June) but from two different flight paths (paths UT and UL in Figure 3.1c). Despite being derived from entirely different datasets, the velocity products show remarkable agreement as they clearly fall within our estimated s_v uncertainty of ±0.05 m d^{-1} (section 3.2.5). Hence, cross-comparison of different datasets appears to show that velocity products are robust between varying SfM-MVS input data. Additionally, the velocity products appear to be consistent even when tracking features through water, when tracking through Lake 031 (Figure 3.10). Thus, although refraction at the water surface influences SfM photogrammetry in the z-axis without corrective measures (e.g. Mulsow et al., 2018), these data suggest that the horizontal accuracy of bathymetry generated by SfM-MVS photogrammetry is sufficient to

measure horizontal displacement through (non-turbid) water such as supraglacial lakes.

3.4 Discussion

3.4.1 Comparison with prior methods

In this study we have estimated that, in a glacial environment flying at ∼450 m a.g.l., SfM-MVS photogrammetric products supported by GNSS-AT geolocation can be accurate to ±0.12 m (∼1.1 GSD) and ±0.14 m (∼1.3 GSD) in the horizontal and vertical respectively. With well-constrained geolocation, horizontal (vertical) accuracies can be as high as 0.5-1.0 GSD (1.5-2.0 GSD) (Benassi et al., 2017). Our estimated accuracies are very close to these theoretical values – in fact, our vertical accuracy is even higher. Our lower accuracy in the horizontal is likely due to the fact that s_{RMSE} includes feature tracking error. Common estimates of the latter can be up to 0.5 pixels (e.g. Quincey et al., 2015), which if assumed in our use case would bring the s_{xy} estimate down to as little as ∼0.5 GSD. Our estimated accuracy values agree well with previously reported GNSS-AT derived estimates. For instance, Fazeli et al. (2016) report horizontal (vertical) accuracies of 0.6 (1.0) GSD using a low-cost customised multirotor UAV. Our accuracies also align with reported horizontal (vertical) accuracies of commercial fixed-wing drones, which offer similar performance to our low-cost alternative at a considerably higher price. Studies using the eBee RTK have reported horizontal (vertical) accuracies of 1.0 (1.2) GSD (Roze et al., 2014), and 0.6-1.2 (0.8-4.0) GSD (Benassi et al., 2017), and 0.8 (1.8) GSD (van der Sluijs et al., 2018), whilst the WingtraOne PPK has reported horizontal (vertical) accuracies of 1.3 (2.3) GSD (Ng and Buchheim, 2018). As a result of this level of accuracy, feature tracking can be used to reliably resolve decimetre-scale displacement (s_{RMSE} = 0.17 m, ∼1.5 GSD) in the ice surface without the use of GCPs. For the investigation of glacier dynamics, where installing and surveying GCPs is logistically demanding, GNSS-AT therefore represents an especially significant technical advance. The method reported here can be directly compared to analogous UAV studies of Greenland glacier dynamics where both methods and uncertainty assessments have been rigorously reported.

The first example is that of Ryan et al. (2015) for Store Glacier, who were amongst the first to use UAVs in a study of Greenland Ice Sheet dynamics. Ryan et al. (2015) geolocate imagery in a two-stage procedure. First, external calibration in the SfM-MVS process was performed camera coordinates provided by an on-board autopilot navigational GPS receiver, which had an accuracy ±5 m. Flying at ∼500 m a.g.l. (GSD ∼0.18 cm) provided a DEM with relative errors up to ±17.12 m horizontally (∼95.5 GSD) and ±11.38 m vertically (∼63.2 GSD), with notable warping in sea-level. A secondary stage of processing used a single GCP at the glacier margin, 3-D co-registration of DEMs using visible common control points such as boulders and promontories, as well as a number of sea level control points given nominal values of zero m a.g.l.. These secondary step reduced measured RMSE across bedrock margins to ±1.41 m horizontally (∼7.8 GSD) and ± 1.90 m vertically (∼10.6 GSD). Hence, Ryan et al. (2015) show that it is possible to achieve scientifically valuable results even without strong ground control. However, an error >1 m is of limited use to assess displacement on slower-flowing glaciers, or over short time periods – indeed, the velocity fields of Ryan et al. (2015) have notable artefacts in slow-flowing (<5 m d^{-1}) sectors of the calving front. The GNSS-AT method shown here provides an order-of-magnitude improvement in accuracy, as well as eliminating an additional processing step. Despite this study using a shorter time interval between flights (6 hours compared to 24 hours) – and hence evaluating velocity from a smaller magnitude of displacement – the velocity fields in this study are more accurate, permitting detection of changes in the slow-flowing sections of the ice margin. The method also successfully reconstructs a flat sea level (this can be seen in the first three transects displayed in Figure 3.4b – the final transect is disrupted by poor reconstruction of open water). The previous failure to reconstruct a flat sea surface of constant elevation in the first processing pass of Ryan et al. (2015) is likely a 'bowing' effect from radial lens distortion error in the fixed or self-calibrated camera calibration (James and Robson, 2014), a feature that can be reduced significantly with precise georeferencing (James et al., 2017).

Further work on UAV dynamics studies of calving fronts was developed by Jouvet et al. (2018, 2017) for Bowdoin Glacier in North Greenland. They report an improved horizontal accuracy of 10-20 cm (∼1.4-2.9 GSD), a value that improves on Ryan et al. (2015), and approximately double that in this study. They achieve this level of accuracy using ten GCPs on each side of the 3 km-wide calving front, as well as two GCPs on the glacier surface recorded using repeat dGPS positioning,

with absolute positions of on-ice GCPs during each flight linearly interpolated. They also fly at a lower altitude (∼300 m a.g.l.; GSD ∼7 cm) than that of Ryan et al. (2015) and this study (450-500 m a.g.l.), which improves the quality of photogrammetric reconstruction whilst limiting the total area able to be assessed in a single flight (Bowdoin is ∼3 km across, whilst Store is ∼5 km). Hence, Jouvet et al. (2018, 2017) show that it is possible to work with moving on-ice GCPs to provide viable products. However, the logistical effort is still considerable, and as a result GCP density is sparse, with large distances (up to 2 km) between GCPs, which likely leads to significant errors at points far from GCP location (Gindraux et al., 2017; Tonkin and Midgley, 2016). Additionally, linearly interpolating moving GCPs on the calving front: (i) requires that the calving front is a safe space to operate in logistically; and (ii) assumes that the glacier is moving at a constant velocity, which is a non-optimal assumption especially when studying glacier dynamics. The GNSS-AT approach applied here allows for the ability to resolve decimetre-scale displacements without depending on a GCP network. This resolves large logistical challenges at marine-terminating calving fronts, where collecting GCPs on both sides of the calving front and on the ice itself would likely require a safe operating environment, considerable time investment, and/or helicopter access, all of which are downsides that UAVs are in some way meant to alleviate.

Whilst the method described here greatly reduces the logistical requirements of working with a network of GCPs, it does not ultimately change the nature or limitations of the SfM-MVS process. For instance, the identification of key points or common features during the 3-D reconstruction process will still struggle to reconstruct low texture environments such as fresh snow (Gindraux et al., 2017) or open water (visible in Figure 3.5e–f and the final transect of Figure 3.4b), as well as the true depth of crevasses (Ryan et al., 2015). Image collection should still be conducted according to best practice, including careful consideration of image overlap and flight geometry (James and Robson, 2014).

3.4.2 Applications

The case studies of a calving front and ice sheet interior provided in this study show two different applications of the GNSS-AT method: one in a calving front environment where UAVs have previously been used, and one in an ice sheet inte-

rior, where UAVs have not to date been used to assess ice dynamics. The first case study highlights that existing observations of, for instance, calving events (Jouvet et al., 2018, 2017; Ryan et al., 2015) can be successfully replicated using GNSS-AT methods (Figure 3.5). However, the second case study, deriving surface velocity of an ice sheet interior, has not previously been possible using UAV-SfM methods. Instead, UAV-based ice sheet studies have largely focused on non-dynamic aspects of surface glaciology, such as albedo (e.g. Burkhart et al., 2017; Ryan et al., 2017).

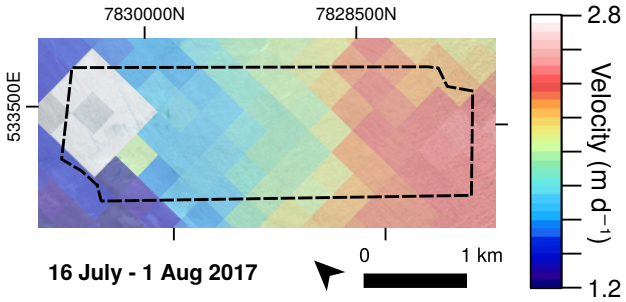

Fig. 3.10 Landsat 8 OLI-derived velocity field of the study area between 16th July and 1st August 2017. Data is from GoLIVE project (Fahnestock et al., 2016, resolution = 300 m), overlaid onto Sentinel-2 optical imagery. Black outline marks the extent of the study zone in Figure 3.7. Note that feature tracking has failed over the site of the former lake bed.

Inland, opportunities for measurement of ice velocity are currently restricted to either: high-resolution in-situ GNSS measurements (e.g Doyle et al., 2015), which can capture ice velocity at extremely high temporal resolution and accuracy but only for point measurements; or satellite remote sensing techniques (e.g. Tedstone et al., 2015), which can offer regional coverage at the expense of spatial and temporal resolution (and often an inherent trade-off between the two). The opportunity for broad spatial coverage of ice velocity at high temporal resolutions (e.g. daily) is extremely limited, and often restricted to opportunistic or targeted observations where repeat intervals occur at adequate frequencies (e.g. Minchew et al., 2017; Palmer et al., 2011). UAV-based techniques allow for high-resolution velocity fields to be obtained by field researchers in targeted areas without dependency on high temporal resolution satellite observations, and with a much higher quality product than that available from global datasets and products. This quality improvement is apparent when we compare the inland velocity product in this study to a GoLIVE (Landsat-8 derived) product (Figure 3.10; Fahnestock et al., 2016). While the satellite-derived data captures the overall variation of ice flow in the study re-

gion, the acceleration from west to east is considerably less detailed. The reduced temporal resolution (16 days) results in a failure of the feature tracking algorithm to capture changes over the former lake bed, where changes in the supraglacial hydrological network disrupted feature tracking (Figure 3.10). The ability to create field-based velocity fields provides new opportunities to study the spatial variation in short-term (daily-weekly) velocity variations on ice sheets, such as those provided by supraglacial lake drainages, or variation in moulin inputs in response to rainfall or melt events.

3.4.3 Future directions

Although our method shows an improvement in accuracy relative to prior glaciological studies, this is in part due to the sub-optimal GCP placement of prior studies that is a necessary by-product of working in glacial environments where access is restricted in many places. When optimally arranged, Benassi et al. (2017) show that a dense network of ground control points still provides a better accuracy than GNSS-AT methods, particularly vertically ($\sim$30% improvement in the horizontal and $\sim$60% in the vertical). However, it has been shown that the error of a GNSS-AT-derived product can be further constrained by the reintroduction of at least one GCP, with a final vertical accuracy only slightly worse than traditional GCP networks (Benassi et al., 2017). Whilst constructing a comprehensive network of GCPs might be difficult on glacial terrain, the introduction of one GCP, either in the form of an existing continuous GPS station, or a single target measured on a per-flight basis or interpolated linearly as per Jouvet et al. (2018, 2017), is far more achievable than a large, dense network of GCPs. The method as described here also lacks the incorporation of directional data in the camera coordinate positions, and hence is referred to as GNSS-AT rather than full DSO (section 3.2.3). The navigational IMU on-board the autopilot was not precise nor accurate enough with regards to time tagging to allow full DSO. The introduction of a more precise IMU – analogous to the improvement in precision between SPS and PPK geolocation in this study – would allow full DSO geolocation in the SfM-MVS process (Cucci et al., 2017) using a low-cost UAV system. However, we are not aware of any applied use of UAV-based DSO in the geosciences at the time of writing.

The UAV system and payload used in this study can be constructed for under £1500, which means our core hardware pushes the boundary of UAV applications in polar and other extreme environments whilst conforming to the low-cost ethos of much geoscientific UAV work. However, the full method we have described here deviates from that ethos by virtue of the dependence on dual-frequency carrier-phase GNSS base station receivers for the differential processing of GPS data, which can often have high costs. Dual-frequency recievers are necessary for carrier phase GNSS correction over distances > 10 km, and hence as long as the UAV is equipped with a single-frequency receiver, there is a necessity for a local (< 10 km) base station to be running in parallel during the flight period. Fortunately, there has been a recent availability of cost-efficient (< USD1000) dual-frequency receivers such as the Piksi Multi (https://www.swiftnav.com/), the Tersus BX305 and BX316R (https://www.tersus-gnss.com/), and the ComNav K501G and K708 (http://www.comnavtech.com/). These receivers present three potential innovations on the method presented here. Firstly, the integration of these low-cost systems would reduce the initial capital cost of projects that do not already have access to an expensive dual-frequency GPS receiver. Second, these GPS receivers are small and light enough to fit on small-sized UAV airframes, and hence allow for (i) an improved flight baseline and accuracy, and (ii) direct kinematic correction against an off-ice reference station (i.e. the removal of the need for processing the intermediate base station 'B1' in ice sheet environments). Finally, these receivers could act as affordable on-ice base stations that could be distributed with a high enough density to act as low-cost 'continuous' on-ice GCPs, allowing for reduced error (as above) and validation of the final point cloud output.

3.5 Conclusions

We have presented the application of an alternative SfM-MVS geolocation method known as GNSS-supported aerial triangulation, which uses an on-board carrier-phase GNSS receiver to geolocate SfM-MVS point clouds while significantly reducing the need for GCPs. Using the calving ice front of a large Greenlandic outlet glacier as a test case, we have shown that uncertainties in the reconstruction of the glaciers surface can be reduced to ± 0.12 metres horizontally ($\sim$1.1 GSD) and

$\pm$0.14 m vertically ($\sim$1.3 GSD), when flying at $\sim$450 m a.g.l. These values compare favourably with those obtained in previous studies, which used networks of GCPs for geolocation. The elimination of ground control allows us to assess ice displacement at an inland site and to produce, to our knowledge, the first example of velocity fields derived from UAV methods at an ice sheet interior site.

The nature of studies of glacial environments inherently limits the ability of users to collect dense networks of GCPs. GNSS-AT will be of interest to those wishing to use UAV photogrammetry to obtain high-precision measurements in all glacial contexts, but will be of particular value for operation in the interior of larger ice masses, such as ice sheets, where operation away from exposed bedrock makes the collection of stable GCPs a nearly impossible task. This method has further applications, both within studies of the cryosphere – for example, in studies of sea ice – but more broadly in all geoscience applications where UAV operation occurs in hazardous environments.

Chapter 4

Results II: Assessing the dynamic impacts of a supraglacial lake drainage

In the previous chapter, it was demonstrated that the GNSS-AT workflow is suitable for obtaining accurate measures of glacier velocity without the use of extensive ground control. Inland surveys from the 2017 ablation season also mapped in detail the empty lake basin of the rapidly draining Lake 028 (Fig. 3.7). Field-based studies of rapidly draining lakes are rare, and in particular no observations have been taken in marine-terminating sectors of the GrIS. Although remote-sensing studies have examined occurrences of rapid drainage in the Store Glacier drainage basin (Cooley and Christoffersen, 2017; Williamson et al., 2018b), the challenges of observing the effects of rapid drainage from remote sensing data (Fig. 3.10) means that observations of the spatial variability of the dynamic efffects of lake-drainage have been limited to slow-flowing sectors (Joughin et al., 2013). This context means that there were gaps in the literature relating to (i) high-resolution, spatially distributed observations of lake drainage events; and (ii) a focus on a fast-flowing, marine-terminating sectors. This chapter therefore uses the workflow developed in Chapter 3 to examine the spatial variability and underlying mechanism of the drainage of Lake 028 in the ablation season of 2018.

Chapter published in **Proceedings of the National Academy of Sciences**, December 2019.

Citation Chudley, T.R., Christoffersen, P., Doyle, S. H., Bougamont, M., Schoonman, C. M., Hubbard, B., and James, M. R. (2019). **Supraglacial lake drainage at a fast-flowing Greenlandic outlet glacier.** *Proceedings of the National Academy of Sciences*, 116 (51), 25468-25477. https://doi.org/10.1073/pnas.1913685116

Contributions Tom Chudley and Poul Christoffersen designed the study; Tom Chudley collected and processed photogrammetry and analysed data;. Sam Doyle collected and processed GPS ground station and pressure transducer data, with post-processing by Tom Chudley; Marion Bougamont modelled subglacial routing; Charlie Schoonman collected and processed seismic data; Bryn Hubbard assisted with structural interpretation; Mike James assisted with photogrammetry; Tom Chudley wrote the paper with input from all authors. Two anonymous reviewers reviewed this manuscript for *Proceedings of the National Academy of Sciences*.

Abstract

Supraglacial lake drainage events influence Greenland Ice Sheet dynamics on hourly to interannual timescales. However, direct observations are rare and, to date, no *in-situ* studies exist from fast-flowing sectors of the ice sheet. Here, we present novel observations of a rapid lake drainage event at Store Glacier, West Greenland, in 2018. The drainage event transported 4.8×10^6 m^3 of meltwater to the glacier bed in ~5 hours, reducing the lake to a third of its original volume. During drainage, the local ice surface rose by 0.55 m and surface velocity increased from 2.0 m d^{-1} to 5.3 m d^{-1}. Dynamic responses were greatest ~4 km downstream from the lake, which we interpret as an area of transient water storage constrained by basal topography. Drainage initiated, without any precursory trigger, when the lake expanded and reactivated a pre-existing fracture that had been responsible for a drainage event one year earlier. Since formation, this fracture had advected ~600 m from the lake's deepest point, meaning the lake did not fully drain. Partial drainage events have previously been assumed to occur slowly via lake overtopping, with a comparatively small dynamic influence. In contrast, our findings show that partial drainage events can be caused by hydrofracture, producing new hydrological connections that continue to concentrate the supply of surface meltwater to the bed of the ice sheet throughout the melt season. Our findings therefore indicate that the quantity and resultant dynamic influence of rapid lake drainages are likely being under-estimated.

4.1 Introduction

Variation in the rate of meltwater input into the subglacial system of the Greenland Ice Sheet forces dynamic responses at a range of scales, from hourly (Das et al., 2008; Doyle et al., 2013; Stevens et al., 2015) to seasonal (Bartholomew et al., 2010; Moon et al., 2014; Sundal et al., 2011) and longer (Doyle et al., 2014; Tedstone et al., 2015). A notable source of meltwater delivery is via rapid supraglacial lake drainages, whereby lakes drain to the bed of a glacier or ice sheet in the space of a few hours. The large volume of water delivered rapidly to the bed during drainage results in hydraulic ice-bed separation, which is expressed at the surface as decimetre-scale ice uplift (Dow et al., 2015; Doyle et al., 2013; Sugiyama

et al., 2008). These evacuations induce short-term ice-flow accelerations via a reduction in basal traction (Das et al., 2008; Doyle et al., 2013; Tedesco et al., 2013), modifying the seasonal efficiency of the subglacial system (Andrews et al., 2018; Hoffman et al., 2011; Sundal et al., 2011), and opening new surface-to-bed connections (Hoffman et al., 2018) that can then continue to deliver meltwater to the bed (Catania and Neumann, 2010). Since the advent of satellite records in the 1970s, supraglacial lakes have formed in greater numbers, at higher elevations, and at larger sizes in response to warmer summers (Cooley and Christoffersen, 2017; Fitzpatrick et al., 2014; Howat et al., 2013). However, the net effect of an increasing meltwater supply on the dynamics of the Greenland ice sheet is the subject of ongoing debate (Bougamont et al., 2014; Doyle et al., 2014; Meierbachtol et al., 2013; Sole et al., 2013; Tedstone et al., 2015).

Satellite observations show that 28%-45% of all supraglacial lakes in West Greenland drain rapidly (Cooley and Christoffersen, 2017; Fitzpatrick et al., 2014), although multi-year studies indicate that even lakes that exhibit rapid drainage behaviour do so in fewer than half of years (Morriss et al., 2013; Selmes et al., 2013). Rapid drainage occurs when water opens a surface-to-bed connection via hydraulic fracture (Das et al., 2008; Doyle et al., 2013; Stevens et al., 2015). However, the exact timing of hydrofracture is seemingly stochastic, with studies failing to support the hypothesis that the drainage of lakes can be explained by any critical thresholds relating to lake hydrology (depth, volume, or morphology), glaciological setting (hypsometry, velocity, or strain) or meteorological conditions (Fitzpatrick et al., 2014; Williamson et al., 2018b). Lakes often drain in clusters (Fitzpatrick et al., 2014) because the transfer of water to the base of the ice sheet when one lake drains increases the tensile stresses near other lakes, triggering further hydrofractures (Christoffersen et al., 2018). Recent research has hypothesised that most lakes drain in these cascading events (Christoffersen et al., 2018) and that pre-existing weaknesses in the ice may play a role (Stevens et al., 2015; Williamson et al., 2018b). However, field studies capturing rapid drainage are limited and have only previously been conducted on slow-flowing ($\sim$100 m a^{-1}) land-terminating regions of the ice sheet (Carmichael et al., 2015; Das et al., 2008; Doyle et al., 2013; Stevens et al., 2015; Tedesco et al., 2013). It is unclear the extent to which knowledge of subglacial hydrology at land-terminating margins may be applied to fast-flowing marine-terminating systems (Nienow et al., 2017)

where supraglacial lakes are equally numerous (Cooley and Christoffersen, 2017; Williamson et al., 2018b).

Here, we present field measurements of the rapid drainage of the supraglacial lake 'Lake 028' (70.57°N, 50.08°W; Fig. 4.1) located ∼30 km from the marine terminus of Store Glacier (*Sermeq Kujalleq*) in West Greenland, at a site where annual ice flow averages ∼600 m a^{-1}. We combine data from repeat Uncrewed Aerial Vehicle (UAV) photogrammetry with *in-situ* geophysical observations from pressure transducer, dual-frequency GPS, and seismometers. The addition of high-resolution photogrammetry data allows the spatial distribution of dynamic response to be assessed, and aids detailed structural interpretation of the drainage event. We present observations at high spatial and temporal resolutions, describe the lake drainage mechanism, interpret the dynamic effects and structural history of the lake drainage, and discuss the larger-scale significance of the observed mode of lake drainage.

4.2 Methods

By the 2018-07-07 drainage event, Lake 028 was instrumented with a GPS receiver, seismometer, and pressure transducer sensor (Fig. 4.1a). A dual-frequency GPS was installed ∼600 m upstream of the lake in July 2017, and by July 2018 had advected into a position immediately south of the lake. A seismometer was installed in May 2018, and a water-level sensor on 2018-07-04. From this date, regular UAV surveys (See Appendix B, Table B.1) were performed over the lake and surrounding environments. Lake 028 drained three days later, on 2018-07-07 between approximately 18:00 and 23:00 (Fig. 4.1b). All times are expressed in Coordinated Universal Time (UTC).

4.2.1 Pressure Transducer

A pressure transducer (Solinst 3001 Levelogger) was installed on the 2018-07-04, logging at 2-minute intervals. The record was corrected for changes in atmospheric pressure using hourly surface pressure data from ERA-5 reanalysis data (Copernicus Climate Change Service, 2017). A depth-volume relationship was

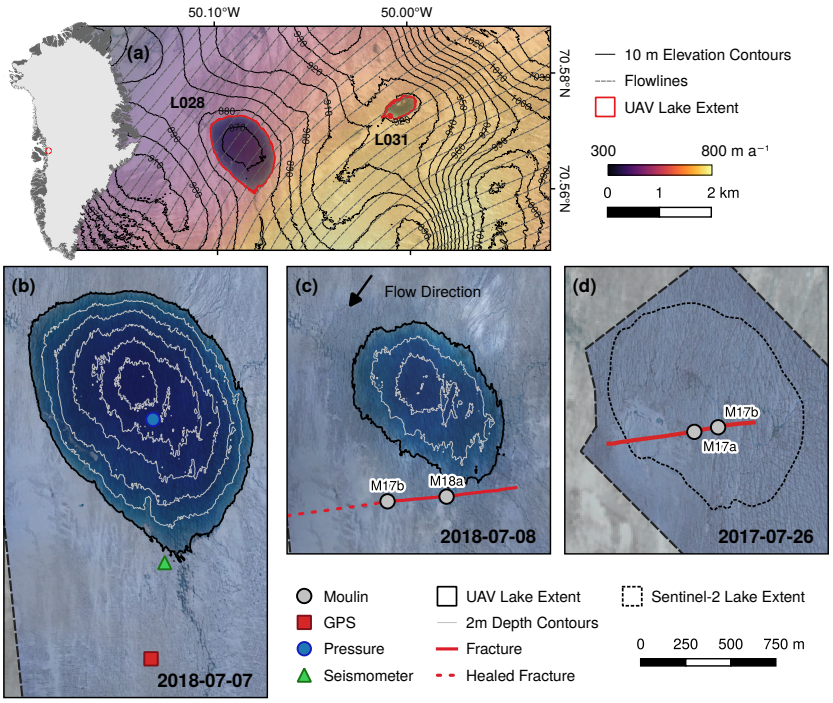

Fig. 4.1 (a) Location of Lake 028 and Lake 031 (red outlines). Sentinel-2 image from 2018-07-07 overlaid with the MEaSUREs 2017 velocity dataset (Joughin et al., 2010) and contour lines from ArcticDEM (Porter et al., 2018) (inset: location of Store Glacier in Greenland). (b) Lake 028 on 2018-07-07, ∼5 hours prior to the onset of drainage, with instrument locations highlighted. (c) Lake 028 on the 2018-07-08 ∼4 hours after peak drainage, with ∼1-km-long fracture marked in red, and moulins marked as white dots. (d) Bed of fully-drained Lake 028 on 2017-07-26, with maximum observed lake margin (from 2017-06-26) outlined with dashed black line.

established using a bathymetry map of the lake at 0.2 m resolution produced from depth-corrected UAV-derived DEMs (see Appendix B, Supplementary Text). Time series of lake volume (V), discharge (Q), and rate of change in discharge (dQ/dt) were calculated from this depth-volume relationship.

4.2.2 GPS

We measured ice surface velocity and uplift using a Trimble NetR7 dual-frequency Global Positioning System (GPS) receiver logging continuously at 0.1 Hz using a Trimble Zephyr Geodetic III Antenna. We processed dual-frequency GPS data kinematically (King, 2004) using the differential carrier-phase positioning soft-

ware, Track v. 1.30 (Chen, 1998, http://geoweb.mit.edu/gg/) and final precise ephemeris from the International GNSS Service (Dow et al., 2009). The data were processed against an off-ice reference system, a Trimble NetR9 receiver located on *Qarassap Nunata* (70.4 °N, 50.7 °W). We discarded solutions where carrier-phase ambiguities were not fixed to the current integer, where an insufficient number (<4) of double-difference calculations were made, or where position standard deviation exceeded 0.035 m. High-frequency noise was filtered with a two-pole, low-pass Butterworth filter with a 30-minute cutoff period (Doyle, 2014). This 30-minute window was chosen based on a worst case horizontal positional uncertainty of 0.035 m and a base ice velocity of $\sim$650 m a^{-1}, following from which assumptions the period over which velocities can be resolved is $\sim$0.5 hours. Uncertainty was calculated based on a conservative estimate of the positional uncertainty of $\pm$1 cm propagated through the velocity calculation.

4.2.3 Seismometers

Seismic monitoring was conducted using a passive HG-7 10 Hz geophone deployed in a shallow (3 m) borehole. Recordings were taken at 400 Hz using a DiGOS DATA-CUBE. Changes in seismic energy were studied using the normalised root mean square amplitude. Data were decimated to 100 Hz and a 2-pole, zero-phase bandpass filter (10-50 Hz) was applied to eliminate instrument and high-frequency noise. The normalised RMS amplitude was then calculated for 60 s time windows. The normalised cumulative amplitude was also calculated to identify rapid changes in seismic energy.

4.2.4 UAV Photogrammetry

We acquired aerial imagery using a custom 2.1 m fixed-wing UAV (Chudley et al., 2019a). The survey plan, designed with the assistance of the 5 m resolution ArcticDEM mosaic, provided a consistent flight altitude of $\sim$450 m, with a ground-level image footprint of $\sim$660 x 440 m and a ground sampling distance (GSD) of 11 cm. Digital imagery was acquired by a Sony α6000 24 MP camera with a fixed 16 mm lens. Imagery was captured every 90 m along flight lines spaced 240 m apart, in order to achieve an >80% (>60%) overlap along (between) flight lines for pho-

togrammetry purposes. The point cloud was geolocated via GNSS-assisted aerial triangulation, using an on-board Emlid Reach single-frequency carrier-phase GPS receiver (recording at 10 Hz) postprocessed using the Emlid RTKLIB b27 software suite against 10 Hz data from a ground-based NetR9s (Chudley et al., 2019a). A total of 11 surveys were performed over the study period between 2018-07-05 and 2018-07-28 (See Appendix B, Table B.1).

Photogrammetric outputs were calculated from images and camera positions using AgiSoft Metashape v.1.4.3 (http://www.agisoft.com), apart from the DEM difference fields displayed in Fig. 4.4a, which were calculated using the updated Agisoft Metashape 1.5.1. Camera calibration was performed automatically in the bundle adjustment process. From the final dense point clouds, we produced orthophotos at 0.15 m resolution and geoid-corrected DEMs at 0.2 m resolution. Horizontal velocity fields were derived by feature tracking 0.2 m resolution multidirectional hillshade models (produced using GDAL 2.2) using OpenPIV feature tracking software (Taylor et al., 2010), using an interrogation window size of 320x320 pixels and a spacing of 32 pixels (final resolution: 6.4 m). We filtered erroneous values using manually chosen upper and lower thresholds for velocity, signal-to-noise ratio (SNR), and divergence from mean annual flow direction. Uncertainties in the velocity field were calculated based on a displacement uncertainty of 0.17 cm, following Chudley et al. (2019a).

When calculating uplift from DEM differencing, we assume the vertical uncertainty to be $\pm$ 0.2 m (Chudley et al., 2019a), which is close to the scale of uplift explored. However, validation against the observed GPS uplift gives some confidence, with a reported GPS uplift of 0.31 cm between the survey periods comparing with a mean UAV-derived uplift of 0.34 ± 0.05 m across a 6 m^2 sample area around the GPS location. Survey precision estimates (James et al., 2017) were centimetric, so uncertainty was likely dominated by survey-wide systematic biases, giving confidence to this validation measurement.

4.2.5 Hydrological Routing

As surface water reaches the ice bed, we assume that it flows following gradients in hydraulic potentials. These are calculated using a multiflow direction algo-

rithm, where the flow is diverted to multiple downslope cells in proportion to the slope between them (Freeman, 1991; Quinn et al., 1991). The gradients in hydraulic potential surface are calculated over the catchment of Store Glacier using:

$$\nabla\theta = \rho_w g \nabla Z_b + \alpha \rho_i g \nabla H \tag{4.1}$$

with $\nabla\theta$ the gradient of the hydraulic potential surface (Pa), ρ_w and ρ_i the density of water and ice respectively (kg m^{-3}), and g the constant of gravitational acceleration (m s^{-2}). The glacier geometry is defined with the gradient of bed elevation (∇Z_b, m) and the gradient of ice thickness (∇H, m), taken from BedMachine V3 (Morlighem et al., 2017) at 150 m spatial resolution. The coefficient α is a floatation fraction, here set to 1 with the assumption that the subglacial water pressure is equal to the ice overburden pressure. Note that the routing of water in our study region remains similar if we assume that the pressure in the hydrological system is just less than the overburden value (α =0.9).

In order to derive discharge from mapped hydraulic potential, we use, as input to the subglacial system, gridded total daily runoff from regional climate model RACMO2. A slightly updated model is used relative to that presented in (Noël et al., 2018): no model physics have been changed, but the spatial resolution of the model has been increased to 5.5 km from 11 km (although output is downscaled to 1 km). Data for the day of drainage was not available at the time of the study. Instead, we use data for 2017-07-26 (a day where a large rainfall event was observed at the study site) as a proxy for a period when high total water input was entering the subglacial system. Discharge was mapped extending ∼140 km inland from the calving front, although only a small section of this is presented in Fig. 4.4c.

4.2.6 Optical satellite imagery

Where optical satellite images were downloaded for RGB visualisation, Sentinel-2 imagery was downloaded from the Copernicus Open Access Hub (scihub.copernicus.eu) and Landsat 8 OLI imagery from the USGS Earth Explorer (earthexplorer.usgs.gov). Long-term lake drainage history for Lake 028, Lake F, and North Lake

were produced using imagery visualised with the Google Earth Engine Digitisation Tool (GEEDiT; Lea, 2018).

4.2.7 Ice Surface Strain Rates

First and second principal strain rates and directions were calculated from MEaSUREs velocity data for 2017 (Joughin et al., 2010). We compute the horizontal part of the strain rate tensor, with derivatives approximated by finite difference of the horizontal velocity field (Alley et al., 2018; Jouvet et al., 2017). The first principal strain rate was calculated as the highest eigenvalue of the strain rate tensor, and the associated eigenvector is the first principal direction. The second principal strain rate (direction) was the lowest eigenvalue (eigenvector).

4.3 Results

4.3.1 2018 Lake Drainage Event

Records from a pressure transducer installed at the bed of Lake 028 on 2018-07-04 were converted into time-series of volume and discharge (Fig. 4.2a-b) using lake bathymetry derived from UAV photogrammetry (see Appendix B, Supplementary Text). These data indicate that in the three days prior to drainage, the volume of Lake 028 was increasing at a rate between 1-10 $m^3\ s^{-1}$. At its maximum extent on 2018-07-07, Lake 028 was 1.25 km^2 in area, 7.3×10^6 m^3 in volume, and fed by three supraglacial streams. A single outflow channel emerged at the southern lake shore (Fig. 4.1b). The lake reached its maximum size immediately prior to drainage, which began on 2018-07-07 17:42 UTC (Fig. 4.2a). Rapid discharge (defined following Doyle et al. (2013) as >50 $m^3\ s^{-1}$) initiated at 18:32 UTC, accelerated notably at approximately 19:58 (Fig. 4.2b), and reached its peak (924 $m^3\ s^{-1}$) at 21:20 UTC. After this, discharge decayed exponentially. 23:22 UTC marked the end of rapid (Q >50 $m^3\ s^{-1}$) drainage, which lasted $\sim$5 hours in total. Lake volume continued to decline for the remainder of the record as flow into the moulin continued: at 2018-07-08 00:00, the lake volume was 2.2×10^6 m^3, but by 2018-07-24 18:00

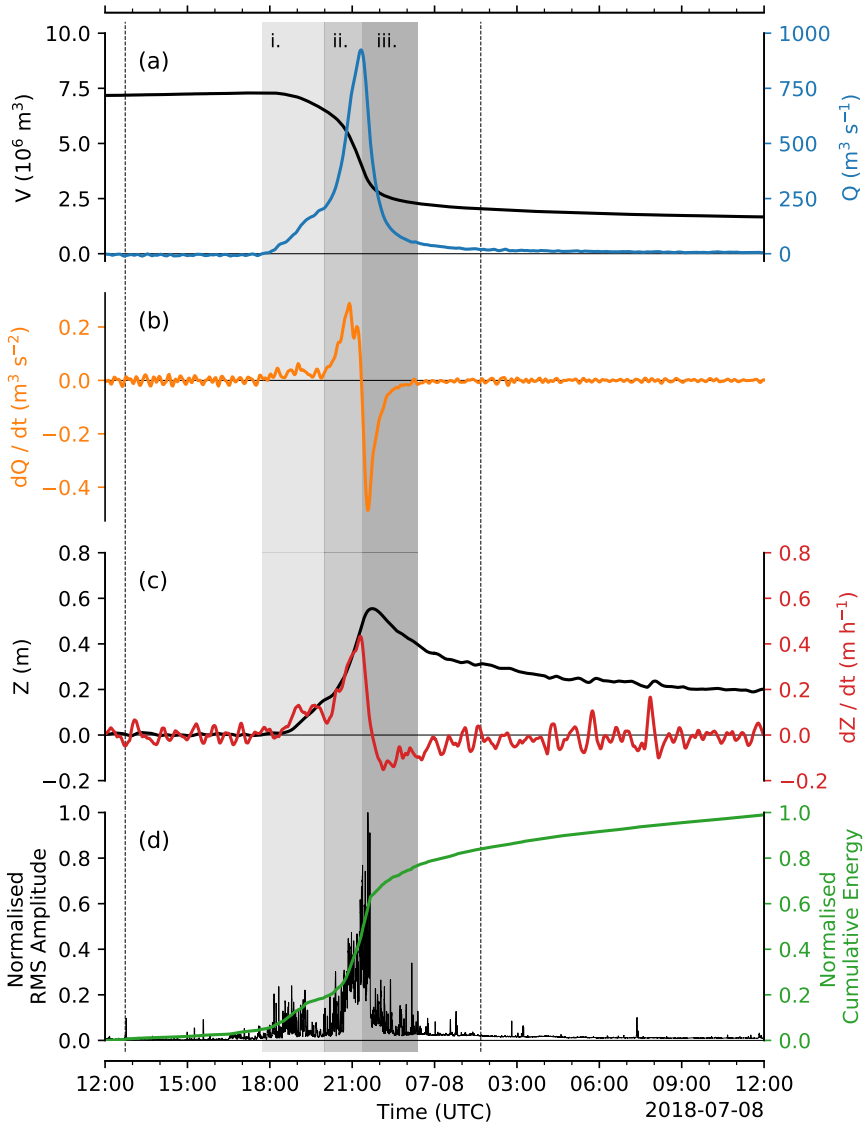

Fig. 4.2 Time-series of (a) lake volume (V) and discharge (Q); (b) rate of change of discharge (dQ/dt); (c) surface uplift (Z) and rate of uplift (dZ/dt); and (d) normalised root mean square (RMS) seismic amplitude, and normalised cumulative energy at Lake 028. Dashed lines at 12:45 and 01:40 mark the timing of pre- and post-flight drainage UAV surveys shown in Fig. 4.1b and c. Shading marks the three phases of rapid drainage outlined in the discussion. A version of this figure cropped to the time of rapid discharge is available as part of Appendix B, Movie B.1.

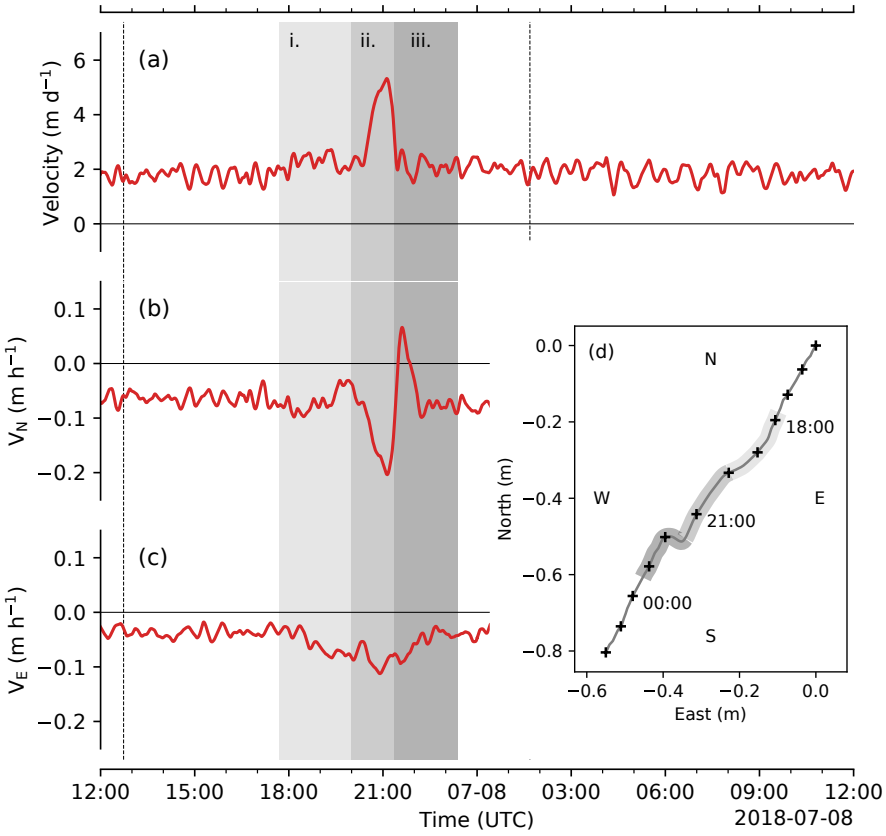

Fig. 4.3 Time-series of location data obtained from GPS instrumentation located ~750 m downflow of Lake 028 (Fig. 4.1b), including (a) resultant horizontal velocity and the (b) northerly (V_N) and (c) easterly (V_E) components of velocity, together with (d) mapped horizontal displacement between 2018-07-07 15:00 and 2018-07-08 02:00, with hourly locations marked with crosses. Dotted lines at 12:45 and 01:40 mark the timing of pre- and post-flight drainage UAV surveys shown in Fig. 4.1b and c. Shading marks the three phases of rapid drainage outlined in the discussion.

was 3.1 $\times 10^5$ m^3. A small ($\sim$200 m diameter) lake was still present in Sentinel-2 imagery by the end of the ablation season, and had frozen over by November 2018.

In addition to discharge measurements, we recorded ice uplift (Fig. 4.2c), seismic activity (Fig. 4.2d), and horizontal ice velocity (Fig. 4.3) using a GPS and seismometer located to the south of the lake (Fig. 4.1b). At approximately 18:30 UTC, coincident with the start of rapid (Q >50 m^3 s^{-1}) drainage, ice uplift initiated at a rate of $\sim$0.1 m h^{-1}. This rate increased, in tandem with discharge, to a maximum rate of $\sim$0.4 m h^{-1} at 21:17 (contemporaneous with maximum discharge). Peak surface uplift of 0.55 m occurred at 21:43 UTC. Subsequently, the ice surface did not return to a pre-drainage elevation, instead settling $\sim$0.2 m above pre-drainage levels (Fig. 4.2c) for the rest of the summer melt season. Trends in seismic data are consistent with those in discharge and surface uplift records. Following low-level (0-0.2 normalised RMS amplitude) activity in the initial drainage period, activity accelerated rapidly after 19:58, reaching a maximum amplitude at 21:34 UTC (coincident with maximum deceleration in discharge), at which point seismic activity returned abruptly to levels <0.3 for the remainder of the drainage period. Ice velocity was relatively consistent until 20:20 UTC, at which point rapid acceleration was observed, from a background velocity of $\sim$2.0 m d^{-1} to a peak of 5.33 m d^{-1} at 21:07 UTC (Fig. 4.3a). Termination of the event was equally rapid, and by 21:27 UTC velocities had returned to normal levels. However, this resultant velocity hides anomalous directional movement (Fig. 4.3b–d). In the early stage of drainage (prior to the step accelerations observed in other data at $\sim$20:00 UTC), the ice velocity trended in a westward direction (parallel with fracture orientation), unaccompanied by any significant change in magnitude. Coincident with the period of most rapid drainage, an anomalous southward displacement initiated (perpendicularly away from the fracture), peaking at a rate of 0.2 m h^{-1} at 21:07 UTC. Following this, a sharp northward anomaly occurred at 21:36 UTC, coincident with maximum negative discharge rate and peak seismic activity.

4.3.2 Spatially distributed uplift and ice flow dynamics

Repeat UAV photogrammetry captured at approximately daily intervals before and after the lake drainage event (See Appendix B, Table B.1) provides novel records of the spatial distribution of the ice sheet's response to drainage in the re-

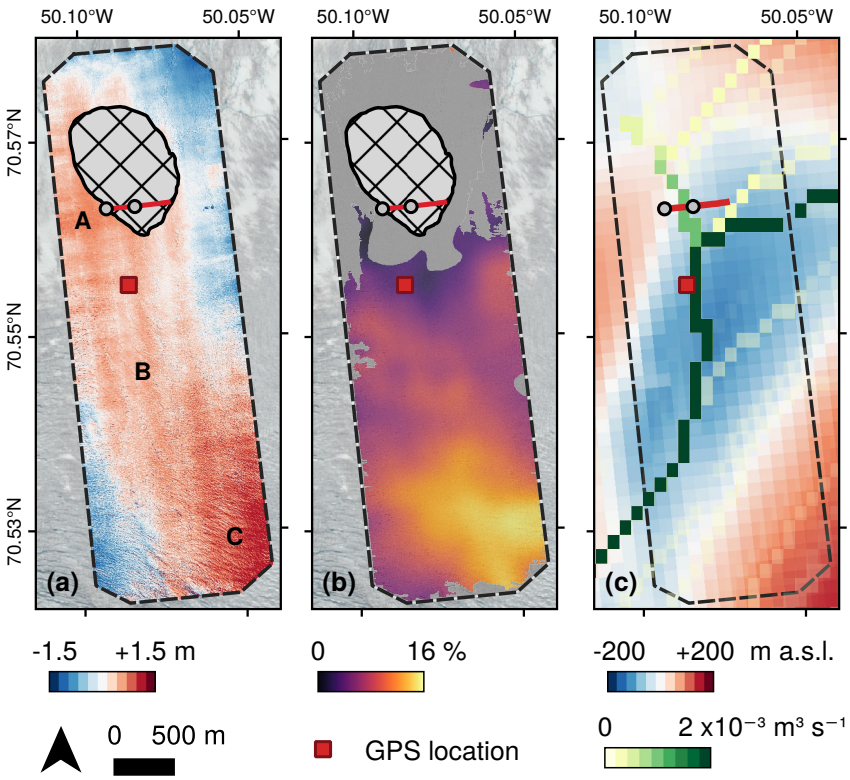

Fig. 4.4 **(a)** Absolute uplift post-drainage at 2018-07-08 01:44 relative to 2018-07-06 16:39 control, with regions A, B, and C referred to in the text labelled. **(b)** Relative acceleration over the period 2018-07-06–09 relative to 2018-07-18–24 control. The grey region marks area of insignificant change based on estimated uncertainty (see methods). **(c)** Modelled water routing, showing contours of discharge following an input of water to the system.

gion surrounding Lake 028 (Appendix B, Table B.1). An immediate post-drainage survey at 2018-07-08 01:45 UTC – ∼2 hours after the termination of rapid drainage – allow us to map drainage-induced uplift (Fig. 4.4a). We identify three distinct regions of uplift. The first major region of uplift (region A) was located surrounding the fracture, on the southwest side of the lake basin. A second major region of uplift (region C), was located at a distal site 4 km S-SE of the fracture. They are linked by a region of lower-magnitude uplift (region B).

Velocity fields are derived from repeat UAV surveys. We compare two velocity fields, one over the lake drainage period (2018-07-06–09) and one from a late-season control period (2018-07-18–24) to highlight regions of anomalous ice velocity during drainage (Fig. 4.4b). These data show that the short-term (on a scale

of hours) acceleration observed in the immediate vicinity of Lake 028 (Fig. 4.3c) is not visible on a multi-day timescale. In contrast, considerable acceleration was observed at the distal site (region C), where ice velocity increased by up to 15% relative to the late-season control period. This suggests that ice velocity here was persistently elevated through the observation period, compared to only short-term acceleration around the lake site itself. This distal region also corresponds to an area of uplift in the elevation difference data.

4.3.3 Inception and propagation of fractures

The 2018 fracture was a direct continuation of a fracture formed during the complete rapid drainage of Lake 028 in 2017 (Fig. 4.1d). Two notable moulins occurred along the 2017 fracture (Fig. 4.5b): one larger (M17a in Fig. 4.5a) and one smaller (M17b in Fig. 4.5a), the latter of which became the dominant drainage moulin for the rest of the 2017 season. By 2018, this pre-existing fracture had advected $\sim$500 m southwest (Fig. 4.5a; c), and both moulins, as well as the fracture, had closed. Between the 2018-07-04 and 2018-07-06, Lake 028 overtopped and began filling M17a (Fig. 4.5c, top-left inset). By the 2018 drainage event, the maximum extent of Lake 028 was coincident with the location of M17b (Fig. 4.5c): post-drainage, this moulin showed evidence of reactivation as it was no longer water-filled (Fig. 4.5c, bottom-right inset). M17a must also have been reactivated, as it was empty of water post drainage (Fig. 4.5c, top-left inset).

Extending from M17b, the western extent of the 2018 fracture was dominated by uneven edges and grabens (Fig. 4.5e). This section of the lake bed is also a region where a number of smaller, pre-existing surface crevasses occur (on the order of 10 m long and 0.5 m wide). The edges of the western extent of the 2018 fracture can be matched directly to these pre-existing crevasses (red lines in Fig. 4.5d), suggesting that the crevasses were exploited during drainage to form the larger fracture. The eastern extent of the 2018 fracture was typified by clean, linear fracturing (Fig. 4.5e), an appearance distinct from the western extent.

The orientation of the fractures in both years was at $\sim$45° to the direction of flow. Comparing this orientation to principal strain rates (Fig. 4.6a) shows that the fractures occurred perpendicular to the direction of first principal strain, indicating

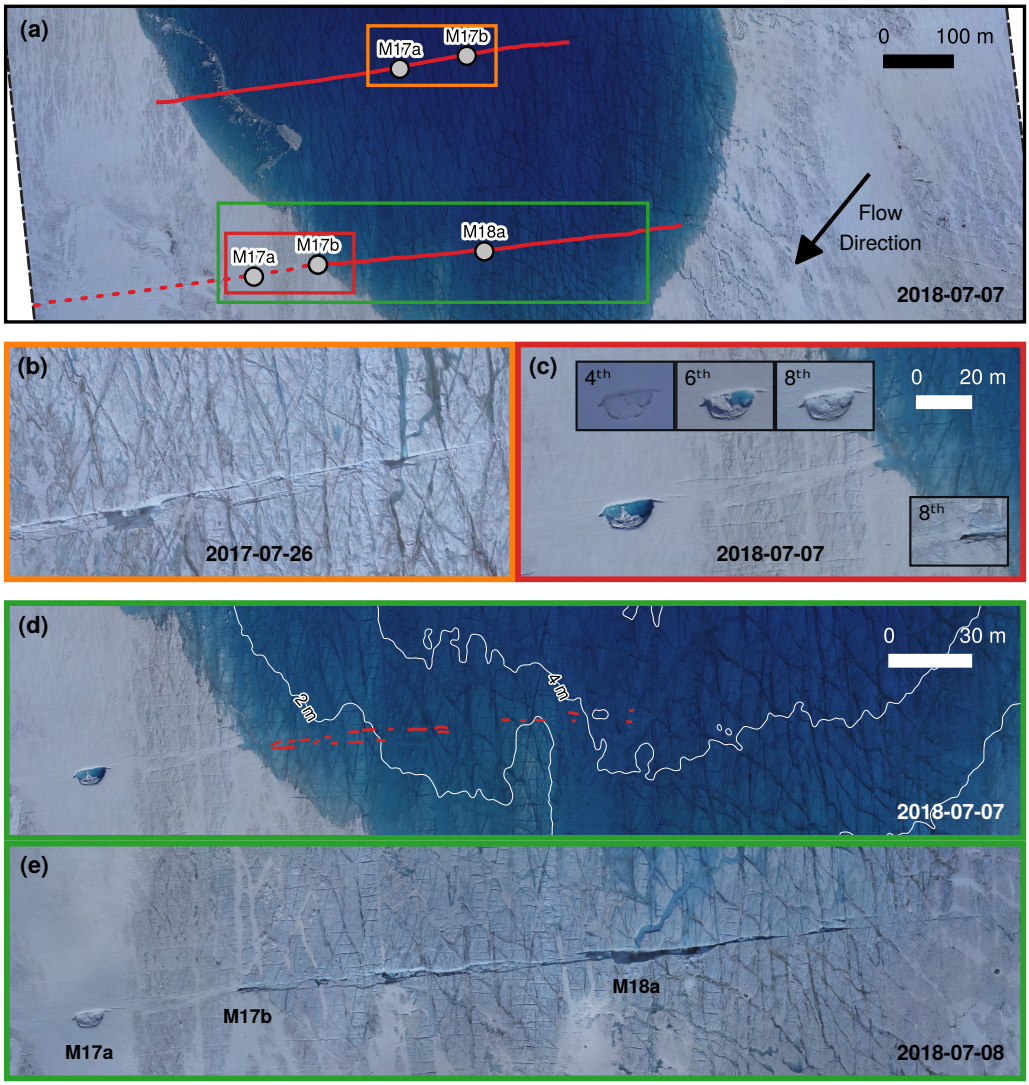

Fig. 4.5 UAV orthophotos of Lake 028 identifying key geomorphological features. (a) Locations of the main drainage fracture (red lines) in 2017 (top) and 2018 (bottom) are marked, along with associated moulins. Dashed red line marks the location of the healed 2017 crevasse in 2018. Coloured boxes indicate locations of panels b–e. (b) The 2017 crevasse and associated moulins 17a and 17b in 2017. (c) 2017 crevasse and associated moulins on 2018-07-07 immediately prior to drainage. The insets show moulin 17a on 2018-07-04, 2018-07-06, and 2018-07-08 (top left) and moulin 18a on 2018-07-08 after drainage (bottom right). (d) Region of Lake 028 subsequently fractured on 2018-07-07, prior to drainage. 2m depth contours are marked in white and crevasses exploited during drainage are in red. (e) Fracture of Lake 028 on 2018-07-08.

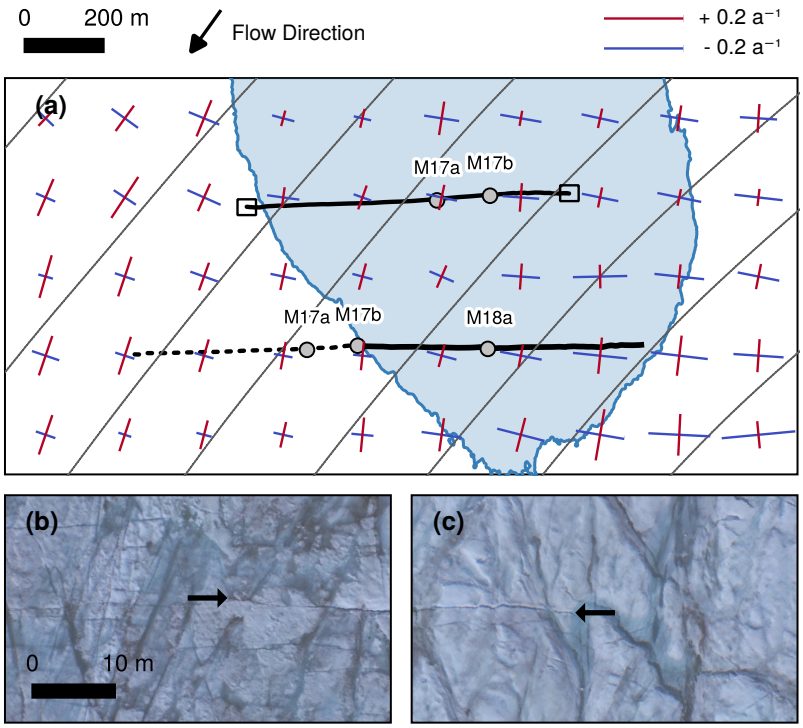

Fig. 4.6 (a) Surface principal strain rates (red and blue lines) derived from 2017 annual MEaSUREs velocity data (Joughin et al., 2010). 2018-07-08 maximum lake area is marked in blue, and flowlines are marked in grey. Black lines define the drainage fracture in 2017 (top) and 2018 (bottom), with the dotted line showing the location of the healed 2017 crevasse in 2018. Black boxes, from left to right, mark locations of UAV orthophotos in panel (b) showing presence of crevasses surrounding western edge of fracture, and (c) showing lack of crevasses around eastern edge of fracture. Black arrows identify the fracture limit.

that the drainage fracture is a Mode I extensional fracture. In 2017, there were no obvious closed moulins or healed fractures to exploit. Instead, the fracture most likely initiated at its western edge, where numerous small surface crevasses occur due to the extensional strain regime (Fig. 4.6b) that could be exploited by hydrofracture. This hydrofracture could then propagate into the compressive lake basin due to inflow of water, first from the supraglacial stream network along the western lake shore and ultimately from the lake itself, leading to full column penetration by hydrofracture. The compressional strain regime on the northeastern (i.e. upflow) side of the lake (Fig. 4.6a), evidenced by a lack of crevasses in the area (Fig. 4.6c), is likely to have have limited the eastern extent of the hydrofracture in both 2017 and 2018.

4.4 Discussion

4.4.1 Lake drainage mechanism

Observational evidence suggests that the drainage of Lake 028 in July 2018 initiated via the refilling of a closed moulin formed during the 2017 lake drainage, and subsequent reactivation of the 2017 hydrofracture. Between UAV surveys on 2018-07-05 (02:00) and 2018-07-06 (16:40) Lake 028's shoreline reached the location of the former moulin M17b. At this point, neither M17a nor M17b was open, as evidenced by the filling of moulin M17a between 2018-07-06 (16:40) and 2018-07-07 (12:45) (Fig. 4.5c, inset). In the hours prior to rapid drainage, minor seismic activity began (Fig. 4.2d), indicative of the episodic hydro-mechanical re-opening of the moulins. In the post-drainage survey (2018-07-09 16:15), these moulins were empty (Fig. 4.5c, inset), indicating that they had connected hydraulically, most likely to the glacier's bed, during the drainage event. Lake drainages have previously been proposed to exploit pre-existing moulins (Doyle et al., 2013; Stevens et al., 2015). Evidence suggests that water entering the subglacial system through pre-existing moulins can trigger hydrofracture by inducing localised acceleration and hence a transient extensional flow regime in a 'precursor' event (Alley et al., 2005; Stevens et al., 2015). However, there is no evidence of precursory acceleration or surface-to-bed connection at Lake 028. Furthermore, there is no evidence of any precursory uplift indicating a triggering upstream drainage event (Christoffersen et al., 2018; Doyle et al., 2013). We suggest that high background tensile stresses were likely sufficient for a surface-to-bed connection to commence as soon as the lake overtopped the pre-existing moulin. Taking the previously studied Lake F (Doyle et al., 2013) as a contrasting example, first principal strains (See Appendix B, Fig. B.1) are an order of magnitude lower than at Lake 028 (Fig. 4.6a), and are not clearly aligned with fracture direction, suggesting that background stresses do not exert a strong control in slow-flowing regions. This observation sheds new light on the proposition that supraglacial lakes can drain in a 'cascading' chain-reaction (Christoffersen et al., 2018). While this mechanism may explain how hydrofracture in low stress regimes can occur in response to upstream drainage, there is still no explanation for the triggering of the upstream events themselves. We propose that lakes like Lake 028 can act as 'trigger lakes', i.e. situated in stress regimes where the simple intersection of an expanding lake

with a pre-existing moulin is enough to trigger hydrofracture. In contrast, lakes from previous *in-situ* studies may be considered 'response lakes', i.e. lakes which require a precursory event in order to drain.

Following drainage initiation, we interpret geophysical activity as representing three clear phases (Doyle et al., 2013): Phase i (17:42–19:58), drainage onset, Phase ii (19:58–21:22), fracture opening, and Phase iii (21:22–23:22), fracture closing (these phases are highlighted in Figures 4.2 and 4.3). Phase i began with the initiation of drainage at 17:42. It was characterised by discharge, uplift, acceleration, and seismic activity that was relatively low compared to later drainage. We suggest that, in phase i, water was delivered to the bed exclusively through the reactivated M17b, and discharge rates increased via the mechanical or thermal erosion of the moulin and the remnant 2017 fracture. This mechanism would explain the distinctive morphology of the western extent of the 2018 fracture, characterised by the exploitation of pre-existing crevasses to form distinctive graben structures (Fig. 4.5e).

Phase ii of Lake 028's drainage began at 19:58 with a step increase in discharge (Fig. 4.2a–b). A sudden and rapid southwards ice displacement is visible in the GPS record at this time (Fig. 4.3b). Given the GPS location 900 m south of the east-west oriented fracture, we interpret this as strong evidence of mechanical fracture opening (Doyle et al., 2013). We interpret the clean, linear fracturing distinctive of the eastern half of the 2018 fracture (Fig. 4.5e) as indicating that the fracture propagated via hydrofracture rather than by mechanical or thermal erosion. This hydrofracture mode began once the fracture propagated into depths greater than 4 m (Fig. 4.5d). As such, this depth likely represents the point at which – in this particular setting – hydrostatic pressure was sufficient to initiate full-column hydrofracture. The westernmost extent of the new hydrofracture was also coincident with the location of M18a, suggesting that hydrofracture initation allowed M18a to connect to the bed. The formation of M18a at this point would have coincided with, and thus explains, the dramatically increased water discharge from Lake 028 at the beginning of phase ii (Fig. 4.2a). This inference is supported by a marked increase in the intensity of seismic activity in this period (Fig. 4.2d), as well as peak horizontal velocity, likely forced by hydraulic jacking. Phase ii terminated at the point of peak discharge (Fig. 4.2a), which was coincident with the beginning of fracture closure as indicated by the GPS data (Fig. 4.3b).

Phase iii is defined from the beginning of negative *dQ/dt* at 21:22. Throughout this period, decreasing discharge was observed: fourteen minutes into the period, at 21:34 UTC, maximum deceleration in discharge occurred (Fig. 4.2b). This timing coincided with a maximum in seismic activity, and three minutes later (21:37 UTC), the northwards anomaly in the GPS record reached a maximum (the northwards anomaly occured from 21:28 – 22:14 UTC). We interpret these closely spaced events as strong evidence of rapid fracture closure occurring in this period. This period of lake drainage was captured with 10 s time-lapse photography from a location to the southeast of the lake (See Appendix B, Movie B.1). This footage shows that early Phase iii, when discharge declined most rapidly (∼21:30–22:15 UTC), occurred simultaneously with the lake level dropping beneath that of the fracture. At this point, a plume of water vapour developed at the fracture mouth as the fracture transitioned from being fully water-filled to a water-air mix. When the fracture was filled to the surface, water pressure exceeded ice overburden pressure and allowed the fracture to remain open. As water content in the fracture reduced, water pressure also lowered and led to fracture closure, lower water inputs, and the subsequent cessation of uplift and acceleration. Therefore, the triggering event for termination of the short-term dynamic response to drainage was the drop in lake water level beneath that of the fracture elevation.

Although we define the end of Phase iii at 23:20 based on the termination of drainage >50 m^3 s^{-1}, there is a long tail to observed hydrological activity. By the time of the post-drainage UAV survey at 2018-07-08 01:45 UTC, the edge of the lake was still proximal to the fracture, and eight seperate channels were flowing into the fracture. By the time of the subsequent UAV survey (2018-07-08 15:15 UTC), only three channels remained, and 24 hours later (2018-07-09 16:15 UTC) one supraglacial channel and associated moulin remained, which dominated for the rest of the melt season.

The elevation time-series from the GPS located to the south of the lake shows a persistent post-drainage surface uplift of ∼0.2 m above the pre-drainage level (Fig. 4.2c). Previous studies have reported a similar phenomenon (Das et al., 2008; Doyle et al., 2013; Stevens et al., 2015; Tedesco et al., 2013), interpreting it as transient water storage at the bed or reverse dip/slip faulting (Doyle et al., 2013). We did not observe any evidence of reverse faulting, so we favour the hypothesis that the persistent uplift is indicative of changes to the subglacial system. Substan-

tial surface lowering (>1 m) was observed in the northeast area of the study site (Fig. 4.4a). Given this lowering was spatially confined and observed over only ∼33 hours, it cannot be explained by surface melt alone. We hypothesise that this excess lowering could relate to a loss of subglacially stored water or sediment in this region following lake drainage. Hence, this pattern of persistent uplift downstream of the lake and surface lowering upstream could be explained some combination of rerouting of the subglacial hydrological system (Lindbäck et al., 2015) leading to increased water storage beneath the location of the GPS, and/or the redistribution of subglacial sediment during rapid lake drainage (Livingstone et al., 2019).

4.4.2 Spatial distribution of dynamic response

The northwest region of ice uplift (Region A in Fig. 4.4a) was located proximal to the fracture. We interpret this to be a result of hydraulic jacking in the region surrounding the direct injection of water to the bed. In modelling studies, this has been interpreted as a turbulent sheet or water 'blister' (Dow et al., 2015) spreading radially from the moulin injection point. Measured uplift here peaked at ∼0.8 m, which is consistent with previous studies (Das et al., 2008; Doyle et al., 2013; Stevens et al., 2015; Tedesco et al., 2013). Uplift was focused to the southwest of the lake centre (Fig. 4.4a), in contrast to previous studies of alpine and ice sheet lake drainages which have speculated that ice uplift is greatest near the centre of lakes (Das et al., 2008; Doyle et al., 2013; Sugiyama et al., 2008). This likely reflects the location of surface-to-bed hydrological connections: the fracture and moulins reported here were located offset in this direction from the lake centre, whereas previous studies of lake drainages have been of lakes that hydrofractured at their centre.

The area of lower-magnitude uplift observed in Region B (Fig. 4.4a), correlates with the predicted peak subglacial discharge pathway (Fig. 4.4c) derived from modelled subglacial hydrological routing (see methods). We interpret uplift at Region B to have resulted from hydraulic jacking – and subsequent concentration of water – along preferential flow routes as lakewater was routed away from the injection site. The > 1 km wide region over which this uplift is distributed leads us to envisage the subglacial hydrology as a turbulent sheet or blister rather than a

single efficient channel. Uplift similiar to that observed at Region B has not been observed previously, but our interpretation agrees with modelling results (Dow et al., 2015), which found that large and efficient subglacial channels do not form rapidly as a result of rapid lake drainage. Instead, water flows downstream once blister growth is restricted by basal topography.

In contrast, the distal area of high-magnitude uplift located in Region C has not been observed or predicted previously. It does not correlate with subglacial flow routes predicted by modelled hydrological routing, which continues along the bedrock trough (Fig. 4.4c). One option to explain this divergence between the inferred and modelled water routing pathways could be due to errors in BedMachine v3, which has reported uncertainty in excess of 50 m around Region C. However, whilst this would explain a simple divergence between inferred and modelled pathways, it does not explain why the uplift of Region C is greater than at regions A or B. We suggest that (assuming the modelled hydrological routing is correct), Region C constitutes an area of less efficient subglacial drainage, which resulted in higher water retention and enhanced hydraulic jacking.

The pattern of water routing described above may also explain why ice acceleration over the drainage period (Fig. 4.4b) was concentrated in region C, whilst acceleration elsewhere, particularly at the lake site itself, was less pronounced. The velocity field in Fig. 4.4b represents a three-day period, and, as such, the significant short-term ($\sim$hours) accelerations observed in the GPS data are likely averaged out. If the northern and central sections of the drainage system became more efficient following lake drainage and moulin formation, then there would be limited dynamic response in these areas throughout most of the velocity observation period. Meanwhile, at region C, an inefficient drainage system may have allowed continuing dynamic response to variations in water input. Dynamic response may have been greater than pre-drainage, as meltwater from the entire catchment area was then being delivered efficiently to the bed via moulin M18a, increasing discharge rates. Hence, the most sensitive response to a lake drainage event on the timescale of days-weeks was not necessarily at the location where water is injected at the bed, but instead governed by the subglacial pathway taken by the water as well as by the physical state of the hydrological system at the bed. These observations align with regional-scale remote sensing data (Joughin et al., 2013), which identified that areas of peak acceleration through a melt season co-

incide with bedrock troughs and intervening ridges, where hydraulic gradients are weak and the rate at which turbulent flow enlarges conduits through melting is low. The study identified these factors as particularly strong in areas where bedrock structures are not well aligned with regional ice flow – as occurs at region C (Fig. 4.4c). *In-situ* studies of lake drainages frequently locate ground instrumentation close to the lake site (Carmichael et al., 2015; Das et al., 2008; Doyle et al., 2013; Stevens et al., 2015). For better quantification of distributed dynamic impacts of lake drainage, future work may wish to also study potential distant 'hotspots' as informed by low hydraulic gradients in the basal environment.

4.4.3 Influence of structural history on lake drainage mode

In recent history, Lake 028 has displayed three different behaviours. Between 2011–2016, the lake did not drain rapidly at all, and froze over at the end of each melt season. In 2017, the lake was able to drain completely through a newly formed hydrofracture located in the lake centre. We hereafter call this a 'primary' hydrofracture. In 2018, the lake drained by reactivating a fracture formed during the previous year's drainage event. We hereafter call this a 'secondary' hydrofracture. However, as the fracture had advected ∼500 m southwest and was oriented 45° to the flow direction, the fracture did not cut across the deepest section of the lake and, as such, the lake failed to drain completely. Here, we make a further distinction between 'complete' and 'partial' rapid drainage. By 2019, any 2018 moulins had advected out of the lake basin entirely and, as such, secondary hydrofracture could not occur again. Instead, in 2019, Lake 028 again underwent complete rapid drainage by primary hydrofracture (See Appendix B, Fig. B.2).

The concept of rapid drainage via the reactivation of pre-existing crevasses and moulins has been proposed previously in slow-moving (∼100 m a^{-1}), land-terminating sectors of the Greenland Ice Sheet at Lake F (Doyle et al., 2013) and North Lake (Stevens et al., 2015). However, Lake 028 exhibits markedly different behaviour from previous *in-situ* studies on two counts. The first is that of interannual behaviour. Manual inspection of 32 years of available Landsat and Sentinel-2 satellite imagery between 1985–2018 suggests that Lake 028 rapidly drained 12 times (38% of years), of which two (2006 and 2018, 17% of drainages) show clear evidence of 'secondary' drainage features (See Appendix B, Figure B.3). Meanwhile,

for a parallel analysis of ten years (2009-2018) of data, Lake F (Doyle et al., 2013) and North Lake (Stevens et al., 2015) fully drained every year, except for one year each (2011 at Lake F and 2014 at North Lake) where the lakes did not fill at all. Our interpretation of these years is that moulins from the previous year remained open, preventing the lakes from forming.

The second difference is the extent of drainage. North Lake and Lake F are both described as reactivating previous moulins/fractures (Doyle et al., 2013; Stevens et al., 2015), and hence would be classified here as draining via secondary hydrofracture. However, they undergo complete rapid drainage, whereas Lake 028 only undergoes partial rapid drainage. We suggest that these differences in behaviour can be explained by two compounding factors: (i) the lower ice velocity in land-terminating sectors of the ice sheet ($\sim$100 m a^{-1}) means that relict moulins and fractures do not advect out of the lake bed after only one year, increasing the chance of drainage via secondary hydrofracture; and (ii) fractures at Lake F and North Lake are aligned parallel with flow direction, meaning that year-on-year, the reactivated fracture intersects the approximate lake centre for consecutive years, allowing for complete rapid drainage. Controls on the orientation of lake drainage fractures in a land-terminating setting have been previously considered in a modelling context (Christoffersen et al., 2018), where the variable direction of flow routing at the bed was considered to be the primary influence on fracture orientation. Here, we show that background stress regime can have strong control on fracture orientation, and as such identify the important role of pre-existing fractures (in 2018) and crevasses advected into the lake basin (in 2017) on fracture orientation, and therefore also on the degree to which rapid lake drainage is complete or partial.

As a result of the two factors described above, North Lake and Lake F consistently experience complete rapid drainage via secondary hydrofracture (Doyle et al., 2013; Stevens et al., 2015). In contrast, lakes like Lake 028, which (i) exist in fast-flowing sectors of the ice sheet where structural weaknesses are rapidly advected outside the lake-bed; and (ii) occur in strain regimes (such as regions of rapidly accelerating ice, or zones of shear) that do not create flow-parallel fractures, make secondary hydrofracture uncommon. Instead, in years without relict moulins or hydrofractures (e.g. 2017), primary hydrofracture must occur by exploiting only surface crevasses, potentially aided by other factors such as the

drainage of neighbouring lakes that trigger short-term perturbations in the regional stress/strain regime (Christoffersen et al., 2018; Fitzpatrick et al., 2014). In the absence of these factors, rapid drainage may not occur at all (e.g. 2011–2016). As a result, lake drainages may be less common (on an individual, interannual level) in fast-flowing sectors of the ice sheet. Given that multi-year remote sensing studies have found that most lakes that exhibit rapid drainage behaviour do so less than 50% of the time (Morriss et al., 2013; Selmes et al., 2013), Lake 028 could provide a representative model for these lakes' interannual behaviour.

The above discussion has implications for remote sensing studies designed to identify rapidly draining lakes automatically. The nature of partial rapid drainage appears site-specific, but if widespread in fast-flowing sectors of the ice sheet then automated lake identification routines in remote sensing studies are highly likely to be misclassifying rapid lake drainages where, like Lake 028 in 2018, only partial drainage occurs. Many classifications use a threshold of 80–90% loss in area (Cooley and Christoffersen, 2017; Morriss et al., 2013; Selmes et al., 2011) or volume (Fitzpatrick et al., 2014; Williamson et al., 2017, 2018a) within a defined period (often 2–6 days) to qualify as a rapid drainage event (i.e. drainage via hydrofracture). In this binary classification, lakes that only drain partially are also assumed to drain slowly (on the scale of ∼days) into pre-existing moulins via fast incision of a supraglacial outlet channel (Clason et al., 2015; Koziol et al., 2017; Tedesco et al., 2013). However, only 41% of area (1.25 to 0.51 km^2) and 66% of volume (7.1 to 2.3 $\times 10^6$ m^3) was lost overnight from Lake 028, meaning that this drainage would not be classified as a rapid/hydrofracture-induced drainage by published identification routines, whereas in situ records of the event clearly show that it meets this criterion in terms of flux and hydrological connection to the bed. Identifying the mode of drainage of Lake 028 in medium-resolution optical imagery can be difficult even when manual identification is used. A key identifying feature is that the configuration of surface outlet channel direction and fracture orientation is such that secondary drainage cuts off the outflow channel, which is present for the full season in years with no drainage (See Appendix B, Figure B.4). It is likely, then, that existing remote sensing routines are underestimating the number of actual rapid lake drainage events. This has important consequences when subglacial hydrological models are forced in part by these remotely sensed observations (e.g. Bougamont et al., 2014; Christoffersen et al., 2018), as these models are correspondingly underestimating the total water volume rapidly delivered to the bed, as well

as, later in the season, the locations at which water is being delivered. The identification of hydrofracture is known to be highly sensitive to the precise criteria applied (Cooley and Christoffersen, 2017), and these findings further highlight a need for more nuanced remote sensing routines to detect drainages.

If rapid lake drainages are more extensive than previously thought, wider implications exist for Greenland ice sheet hydrology and dynamics as lake hydrofracture is thought to be the primary control on moulin density and extent (Hoffman et al., 2018). Moulins are the primary mechanism by which rapid lake drainages can have a longer-term (weeks-years) influence on subglacial hydrology: while supraglacial lakes may contain only ∼3% of the total melt season runoff volume, a further ∼21% has been estimated to drain through newly opened moulins created by hydrofracture events, and an additional ∼15% through pre-existing moulins created during previous melt seasons (Koziol et al., 2017), which can remain active for many years in a row (Catania and Neumann, 2010). Furthermore, moulins act to concentrate meltwater delivery spatially, to a point source, and also temporally, as water transfer via moulin is nearly instantaneous compared to drainage through crevasse systems (McGrath et al., 2011). Our finding that partial lake drainages also occur through hydrofracture indicates that many lakes previously inferred to drain by overtopping or channel incision (Tedesco et al., 2013), in fact are establishing moulins and hydrological connections to the bed (Hoffman et al., 2018). Consequently, a larger portion of the subglacial drainage system could be subject to a persistent, yet also highly variable meltwater supply from the surface. This may mean that, early in the melt season, more of the basal system is subject to pulses in supply (from events such as high-melt days and rainfall) that are capable of overwhelming transmission capacity and therefore enhance basal sliding (McGrath et al., 2011; Schoof, 2010). Later in the season, concentrated meltwater delivery could also accelerate the formation and spatial extent of efficient channels, which have a stabilising effect on the ice sheet's flow (Hoffman et al., 2018; Schoof, 2010; Sundal et al., 2011).

Given the relationship between primary and secondary hydrofracture, we argue that consecutive years of rapid lake drainage are more likely in slow-moving sectors of the ice sheet. In fast-flowing sectors, full-depth fractures are rapidly advected out of lake basins and therefore new hydrofractures must exploit shallower surface crevasses, facilitated by a stronger extensional stress regime. Conversely,

this implies that if a lake can hydrofracture just once in a slow-flowing regime, the presence of relict fractures and moulins makes it easier for rapid drainage to reoccur year-on-year. This is a relevant factor in discussions of interannual dynamic changes in the land-terminating ablation zone (Tedstone et al., 2015), but may be especially important in inland sectors of the ice sheet (Doyle et al., 2014), where surface-to-bed connections have been proposed to be less likely (Poinar et al., 2015). However, if decadal-scale dynamic changes to the ice sheet induce even limited extensional crevassing further inland, one lake drainage via primary hydrofracture may be enough to induce consistent secondary hydrofracture in further years, as relict features are unlikely to advect out of the lake bed within only a few seasons.

4.5 Conclusions

Fast-flowing, marine-terminating glacier hydrology represents a key uncertainty in predictions of sea level rise (Nienow et al., 2017), and the long-term response of marine-terminating glaciers to climate change and lake expansion remains unknown. Our results contribute better observational understanding of ice sheet hydrology and dynamics by identifying key differences between supraglacial lakes on fast-flowing and slow-flowing sectors of the ice sheet. As rapid, hydrofracture-induced drainage can occur even at partially draining lakes in fast-flowing sectors, the increased potential density of surface-to-bed connections (Hoffman et al., 2018) has implications for subglacial drainage efficiency in both the early melt season (as a positive feedback to ice velocity) and in the long term (as a mitigating effect to increased surface melt). The observation that hydrofracture can occur without any precursory hydrologically-induced basal slip (Stevens et al., 2015) identifies for the first time a triggering mechanism for cascading lake drainage events (Christoffersen et al., 2018), which means that the style of drainage observed here could be important in initiating a chain reaction of meltwater delivery to the bed. Furthermore, an increased understanding of the necessary conditions behind year-on-year hydrofracture has significance when considering meltwater delivery to the bed in inland regions, which currently represent a large unknown in predicting future dynamic change of the ice sheet (Doyle et al., 2014; Poinar et al., 2015). Given the ongoing dominance of mass loss via dynamic losses from the

marine-terminating Greenland Ice Sheet (Mouginot et al., 2019a), improving our understanding the unique hydrology and dynamics of these sectors is key to constraining mass balance predictions into the 21st century.

Chapter 5

Results III: Links between crevasse hydrology and stress regime

Chapter 4 demonstrated that supraglacial lake drainages exhibit distinctive behaviour and consequences in marine-terminating settings, and that the style and rate of meltwater delivery to the bed was closely linked to the ice dynamic setting to the lake. It was shown that the dynamic regime of the ice sheet, and in particular the direction and magnitude of the first principal strain, appeared to control the location and orientation of hydrofracture (Fig. 4.6), and that this relationship appeared to be particularly strong in marine-terminating settings. This finding motivates a deeper understanding into how the dynamic regime of the fast-flowing ice sheet may control the delivery of meltwater to the bed via fractures. However, observational studies of the relationship between dynamic regime and hydrofracture are sparse, and numerical modelling studies largely draw on literature studying crevasse initiation to quantify critical threshold processes. This chapter takes advantage of the large spatial coverage provided by the Sentinel-2 satellite mission, complemented by UAV observations that enable high-resolution, crevasse-level observations, in order to better understand the relationship between glacier dynamics and crevasse hydrology across a 3,000 km^2 sector of the west Greenland Ice Sheet.

Chapter submitted for review, April 2020. A preprint of the submitted work is available at the **Earth and Space Science Open Archive**.

Citation Chudley, T. R., Christoffersen, P., Doyle, S. H., Dowling, T. P. F., Law, R., Schoonman, C., Bougamont, M., Hubbard, B. (*in review*). **Structural controls on the hydrology of crevasses on the Greenland ice sheet**. *Earth and Space Science Open Archive*. https://doi.org/10.1002/essoar.10502979.1

Contributions Tom Chudley and Poul Christoffersen designed the study; Tom Chudley collected the photogrammetry data and processed the photogrammetry and satellite data; Sam Doyle collected and processed GPS ground station data; Tom Dowling assisted with machine learning quality assurance; Rob Law and Marion Bougamont assisted with estimating stresses from velocity data; Charlie Schoonman, Rob Law, and Bryn Hubbard assisted with structural interpretation; Tom Chudley wrote the paper with input from all authors.

Abstract

Surface crevasses on the Greenland Ice Sheet deliver significant volumes of meltwater to the englacial and subglacial environment, but the topic has received little attention compared to supraglacial lake and moulin drainage. Here, we explore relationships between crevasse hydrology and the surface stress regime at a fast-flowing, marine-terminating sector of the Greenland ice sheet. Regional-scale observations of surface water, crevasses, and stress were made across a 3,000 km^2 region using satellite data. Contemporaneous high spatio-temporal resolution observations were obtained from uncrewed aerial vehicle surveys on Store Glacier using a supervised classifier and feature-tracked velocities. While previous studies have identified crevasses using von Mises stress thresholds, we find these are insufficient for predicting crevasse hydrology. We found that dry crevasse fields, where no ponded meltwater was observed through the entire melt season, were more likely to exist in tensile mean stress regimes, which we interpret to be due to meltwater draining continuously into the englacial system. Conversely, wet crevasse fields, hosting ponded meltwater, were more likely to exist in compressive mean stress regimes, which we interpret to be a result of closed englacial conduits. We show that these ponded crevasses drain through episodic rapid drainage events (i.e. hydrofracture). Mean stress regime can therefore inform spatially heterogeneous styles of meltwater delivery through crevasses to the bed of ice sheets, with distinct consequences for basal processes such as subglacial drainage efficiency and cryo-hydrologic warming. Thus, we recommend simple guidelines for improving the representation of crevasse hydrology in regional hydrological models.

5.1 Introduction

Surface crevasses are open fractures in glaciers and ice sheets, ranging in width from millimetres to tens of metres. As a visible expression of glacier stress regimes, the size and orientation of crevasses are closely linked to glacier dynamics, associated with extensional flow and deformation of ice through compression or shear along margins (Colgan et al., 2016). Motivations for detecting crevasses and understanding their formation include morphological insights into glacier flow

(Dell et al., 2019; Phillips et al., 2013a), the development of fracturing criteria for supraglacial lake drainage (Arnold et al., 2014; Das et al., 2008) and ice calving (Benn et al., 2017; Todd et al., 2019), and quantifying the dynamic influence of water transmitted to the bed of glaciers (Koziol and Arnold, 2018; McGrath et al., 2011).

In regions of high advection, such as fast-flowing outlet glaciers of the Greenland Ice Sheet (GrIS), crevasses form in upstream zones where extensional stress regimes favour crevasse opening, and then advect downstream into regions where compressive stress regimes result in crevasse closure, forming healed crevasses. The fracture process is generally understood in terms of simple numerical models, such as the 'zero stress' model in which crevasses penetrate to the depth at which ice creep closure (due to ice overburden pressure) equals tensile stress (Nye, 1957), or the linear elastic fracture mechanics (LEFM) approach, which further accounts for factors such as stress concentrations at fracture tips, fracture toughness, geometry, and water level (Krawczynski et al., 2009; Van der Veen, 1998). There is a growing recognition of the need to understand more complex multidimensional and mixed-mode crevasse formation (Colgan et al., 2016), but transferring mechanical understanding to higher dimensions is nontrivial (Colgan et al., 2016; van der Veen, 1999). As such, many studies that predict crevasse presence in real-world scenarios use simpler methods such as basic thresholds of first principal strain or von Mises Stress (Clason et al., 2015; Koziol et al., 2017; Poinar et al., 2015; Williamson et al., 2018b), which have been identified from observational studies to be suitable predictors of crevasse presence (Hambrey and Müller, 1978; Harper et al., 1998; Van der Veen, 1998; Vaughan, 1993).

Crevassing is an important mechanism to transfer water to the bed of the GrIS, and water itself drives the propagation of crevasses via hydrofracture (Alley et al., 2005; Krawczynski et al., 2009; van der Veen, 2007; Weertman, 1973). Once full-depth hydrofracture has occurred, water flow forms an efficient route for continued meltwater delivery to the bed in the form of moulins. To date, this meltwater pathway to the bed has largely been focussed on supraglacial lake drainage (Banwell et al., 2016; Christoffersen et al., 2018; Hoffman et al., 2018). Crevasse hydrology has been included in only a few recent numerical modelling studies (e.g. Clason et al., 2015; Koziol et al., 2017; Koziol and Arnold, 2018), but is understood to capture as much as half of seasonal surface runoff (Koziol et al., 2017; McGrath

et al., 2011). Despite the apparent importance of crevasse hydrology, there are few studies of the transfer of water to the bed of ice masses through crevasse fields, and the limited number of studies that do exist describe variable – and often contradictory – processes. Some studies observe discrete drainage of crevasses (Cavanagh et al., 2017; Lampkin et al., 2013), which appear to result from episodic full-depth hydrofracture and display similarities to supraglacial lake drainages. In contrast, other studies conceptualise crevasse fields as continuously, but inefficiently, transmitting a low water flux to the subglacial system without the need for full-depth hydrofracture (Colgan et al., 2011; McGrath et al., 2011). However, no studies have attempted to account for this spectrum of observations and the assumptions surrounding crevasse hydrology, nor attempted to explain where and why these types of drainage occur. Given this lack of information, previous modelling studies have assumed that crevasse drainage occurs in a uniform manner, and use existing thresholds intended to predict crevasse presence to instead predict crevasse hydrology (Clason et al., 2015; Everett et al., 2016; Koziol et al., 2017). To date, no observational studies exist to guide such choices.

This study aims to better understand crevasse hydrological behaviour by relating the presence of crevasses and water to stress regimes in the ablation zone of the GrIS at two different spatial scales. The first utilises large-scale, satellite-derived data to examine crevasses in a $\sim$3000 km^2 sector of west Greenland, including five major marine-terminating outlet glaciers . The second uses high-resolution photogrammetric datasets collected by uncrewed aerial vehicles (UAVs) to closely examine crevasses in a 7 km^2 area of fast glacier flow within this sector, allowing us to validate large-scale data and record processes occurring at the scale of individual crevasses. Our goal is to understand how glacier dynamics relate to the spectrum of observed crevasse hydrology, and thereby develop guidelines to allow hydrological models to account for the heterogeneity of crevasse hydrological behaviour.

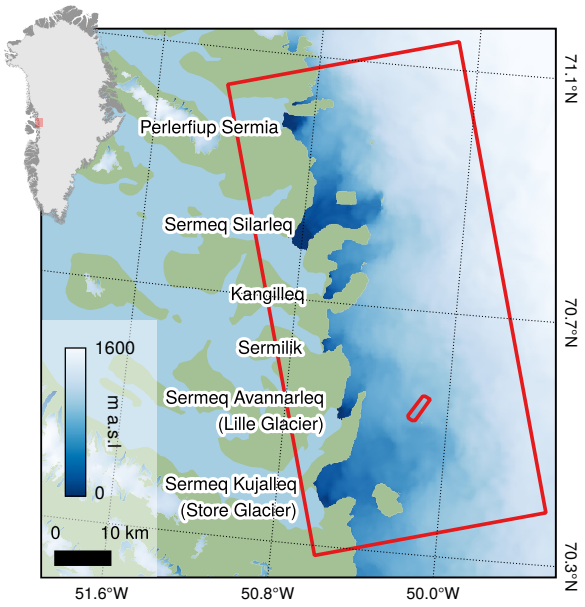

Fig. 5.1 Map of study region. Small red box outline indicates the extent of UAV surveys. Large red box outlines the extent of satellite image analysis. Marine-terminating outlet glaciers are labelled, with the Danish/English name in brackets where applicable. Surface elevation shown in colour is from ArcticDEM v3 (Porter et al., 2018).

5.2 Methods

5.2.1 Study area

We assess satellite-derived data over a ∼3000 km^2 sector of the western GrIS (Figure 5.1), extending ∼90 km from Sermeq Kujalleq (Danish/English: Store Glacier; 70.4°N 50.6°W) in the south to Perlerfiup Sermia (71.0°N, -50.9°W) in the north. Within this large-scale region of interest (the 'satellite ROI'), we use UAV surveys and Structure-from-Motion with Multi-View Stereo (SfM-MVS) photogrammetry to assess, at high resolution, a crevasse field in the Store Glacier drainage basin, 25 km from the calving front (the 'UAV ROI'). The UAV ROI is 1.5 km wide and 5 km long, and was chosen based on its coverage of an initiating crevasse field, ranging from areas with no visible crevasses to areas with crevasses greater than 50 m wide.

5.2.2 Satellite data

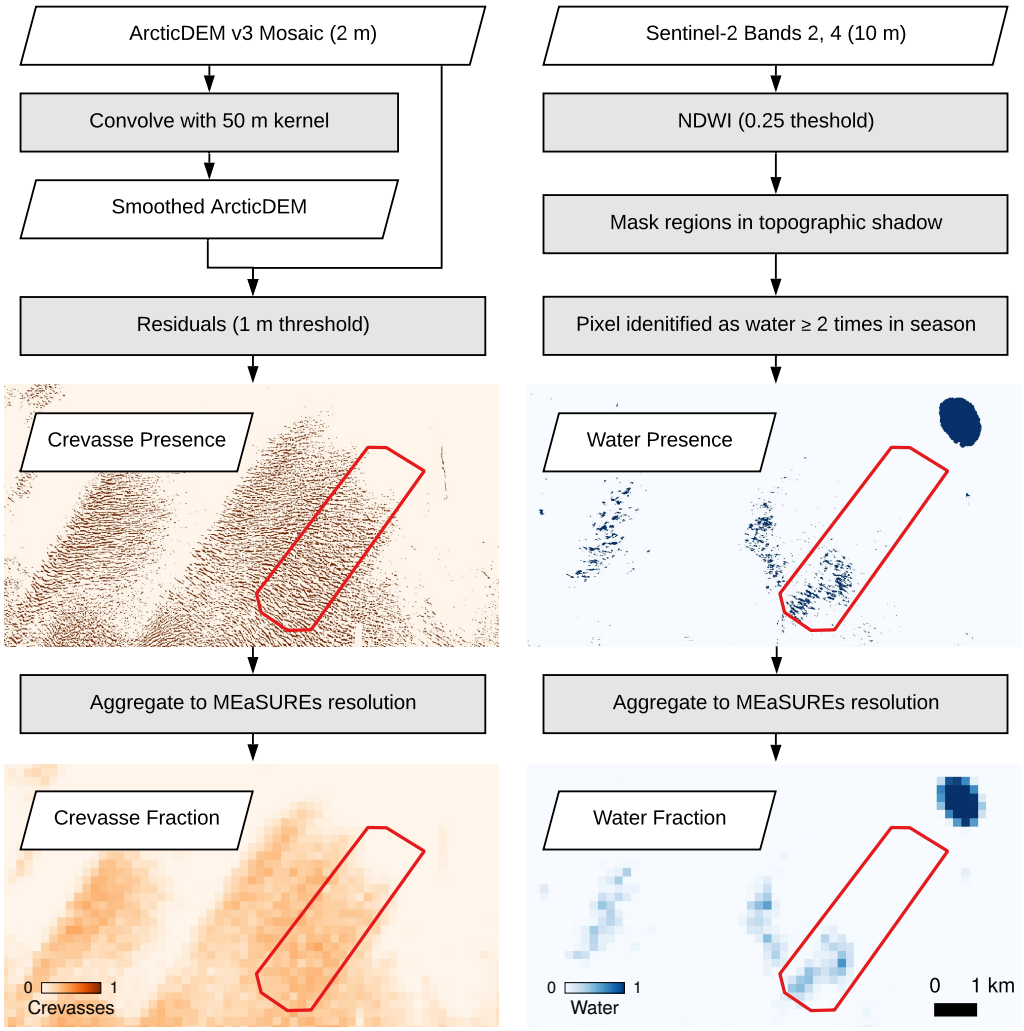

Fig. 5.2 Flow diagram visualising the production of crevasse fraction data from ArcticDEM (left) and water fraction data from Sentinel-2 optical imagery (right). Red box outlined in maps marks the extent of the UAV ROI.

Crevasse classification

A binary crevasse mask (Figure 5.2) of the satellite ROI was produced from ArcticDEM v3 mosaic data at 2 m resolution (Porter et al., 2018). Crevasse identification from digital elevation models can be approached in a variety of ways (Florinsky and Bliakharskii, 2019), but we use a simple method identifying crevasses from

the residuals between the original and a smoothed elevation model. We limit our analysis to the outer 40 km of the ablation zone (Figure 5.1), where snow-filled crevasses are rare, in order to reduce the number of false negatives in the final dataset. We performed these operations in Google Earth Engine (GEE; Gorelick et al., 2017), which allows for efficient computation and rapid evaluation over a large study area. We first cropped the ArcticDEM to the GIMP ice mask (Howat et al., 2014), before smoothing the elevation model by convolving the raster with a circular kernel of 50 m radius. Residuals greater than 1 m between the smoothed and raw elevation values were identified as crevasses. To compare with stress estimates, the 2 m dataset was aggregated into grid cells to match the resolution (200 m) and projection (NSIDC sea ice polar stereographic north) of the velocity grid. Aggregated values ranged from 0–1, representing the fraction of grid cell area classified as crevasses.

Because relict crevasses can advect through a variety of stress regimes (Mottram and Benn, 2009), we further identified crevasse initiation zones. We manually identified the upstream boundary between crevasse fields and bare ice from the 2 m crevasse dataset. Then, we used a 200 m buffer to identify pixels in the 200 m dataset that should be classified as being in crevasse initiation zones.

Water classification

We produced a binary map of water presence across the satellite ROI through the 2018 melt season (Figure 5.2) using Sentinel-2 imagery in GEE. The ablation season of 2018 was chosen for analysis to match the timing of the UAV surveys on Store Glacier. We first identified all Sentinel-2 scenes with < 40% cloud cover and < 70° solar zenith angle between May-October 2018, selecting a total of 360 images. We clipped the images to the GIMP ice mask (Howat et al., 2014) and converted digital number values to top of atmosphere (TOA) reflectance. TOA reflectance values have been shown to be suitable for identifying surface water in Greenland with Landsat 8 OLI imagery (Pope, 2016), and have been used for surface water classification in Sentinel-2 data (Williamson et al., 2018a). We then calculate the normalised difference water index (NDWI) from bands 2 (blue) and 4 (red) for all images: following Williamson et al. (2018a) for the Store Glacier region, we use an NDWI threshold of 0.25 to create binary water classification maps for each

Sentinel-2 image. In order to avoid false positive identification of shaded regions, we mask areas in topographic shadow with the GEE hillShadow function, using the ArcticDEM for topography and the solar zenith angle from Sentinel-2 image metadata. Finally, we sum the image stack to count the number of times through the 2018 melt season that a pixel was identified as water. In order to reduce the chance of false positive classification (e.g. cloud shadow, ephemeral slush zones at the beginning of the melt season) we classify as water any pixel that was identified as water in ≥ 2 images through the melt season. As for crevasse maps, we aggregate this data onto the velocity grid with a unit of fractional coverage of water within each grid cell.

Stress classification

Although some previous studies have used strain rate thresholds to predict crevasse location (Poinar et al., 2015; Williamson et al., 2018b), we follow the recommendations of Colgan et al. (2016) to use estimated stress thresholds as a robust and generalisable criterion across glaciers of widely varying thermal regimes. Studies exploring relationships between crevassing, hydrology, and surface dynamics have used a multitude of 2-D stress measures. In order to test this variation, we calculate: (i) the first and second principal stresses (σ_1 and σ_2 as applied by Poinar et al. (2015) and Williamson et al. (2018b); (ii) the longitudinal stress (σ_l; as used by Clason et al., 2015); and (iii) the von Mises yield stress (σ_v; as used by Clason et al., 2015; Everett et al., 2016; Koziol et al., 2017). We were also motivated to test further measures of stress, as σ_1, σ_2, and σ_l consider stress in only one axis, whilst σ_v considers only the deviatoric component of the stress tensor. Hence, we calculated the mean stress (σ_m, also referred to as the hydrostatic stress), and the signed von Mises Stress (σ_{sv}). Both of these measures account for the normal components of the stress tensor.

Stresses were estimated using surface strain derived from MEaSUREs (Making Earth System Data Records for Use in Research Environments) gridded GrIS velocity data for 2018 (Joughin et al., 2010), with Glen's flow law as the constitutive equation following Clason et al. (2015). We first calculated the surface strain rate tensor $\dot{\epsilon}_{ij}$ from the horizontal components of velocity u and v (in grid directions x and y):

$$\dot{\epsilon}_{ij} = \begin{bmatrix} \frac{\delta u}{\delta x} & \frac{1}{2}(\frac{\delta v}{\delta x} + \frac{\delta u}{\delta y}) \\ \frac{1}{2}(\frac{\delta v}{\delta x} + \frac{\delta u}{\delta y}) & \frac{\delta v}{\delta y} \end{bmatrix} = \begin{bmatrix} \dot{\epsilon}_x & \dot{\epsilon}_{xy} \\ \dot{\epsilon}_{xy} & \dot{\epsilon}_y \end{bmatrix} \tag{5.1}$$

We approximated the derivatives using the finite difference of the velocity field (Alley et al., 2018). We calculated longitudinal strain rate ($\dot{\epsilon}_l$) by resolving strain-rate components relative to the local flow direction according to Bindschadler et al. (1996):

$$\dot{\epsilon}_l = \dot{\epsilon}_x \cos^2 \alpha + 2\dot{\epsilon}_{xy} \sin \alpha + \dot{\epsilon}_y \sin^2 \alpha \tag{5.2}$$

where α is the flow angle defined anti-clockwise from the x axis. Stresses approximated from strain rates following Nye (1957):

$$\sigma_{ij} = B\dot{\epsilon}_e^{(1-n)/n}\dot{\epsilon}_{ij} \tag{5.3}$$

Where $\dot{\epsilon}_e$ is effective strain, calculated following Cuffey and Paterson (2010):

$$\dot{\epsilon}_e = \sqrt{\frac{1}{2}[\dot{\epsilon}_{xx}^2 + \dot{\epsilon}_{yy}^2] + \dot{\epsilon}_{xy}^2} \tag{5.4}$$

and n is the flow law exponent with value 3. B is a viscosity parameter, which we follow Clason et al. (2015) in assigning a value of 324 kPa $a^{1/3}$ (based on an assumed ice temperature of -5 °C).

The first principal stress (σ_1) was calculated as the highest eigenvalue of the stress tensor σ_{ij}, and second principal stress (σ_2) as the lowest eigenvalue (Jouvet et al., 2017).

We calculate the von Mises yield criterion (σ_v) according to Vaughan (1993):

$$\sigma_v = \sqrt{(\sigma_1\sigma_1) + (\sigma_2\sigma_2) - (\sigma_1\sigma_2)} \tag{5.5}$$

We calculate the mean stress (σ_m) as follows:

$$\sigma_m = \frac{1}{2}[\sigma_1 + \sigma_2] \tag{5.6}$$

Finally, the signed von Mises stress (σ_{sv}) is a simple modification of the von Mises stress, calculated as the magnitude of σ_v with the sign of σ_m:

$$\sigma_{sv} = \mathrm{sgn}(\sigma_M) \cdot \sigma_V \tag{5.7}$$

5.2.3 UAV data

UAV photogrammetry and velocity

We acquired aerial imagery across a 13-day period in July 2018 (Table S1) utilising a custom-built, fixed-wing UAV with 2.1 m wing span. Imagery was collected using a Sony α6000 24 MP camera with a fixed 16-mm lens, processed using Structure-from-Motion with Multi-View Stereo (SfM-MVS) photogrammetry, and used to derive velocity fields within the UAV ROI as described by Chudley et al. (2019a). In brief, photogrammetry was performed using AgiSoft Metashape v.1.4.3 software, and geolocated by using an on-board L1 carrier-phase GPS unit (post-processed against an on-ice ground station) to locate the position of aerial photos. Outputs from the photogrammetric process were 0.15 m resolution orthophotos and 0.2 m DEMs. Horizontal velocity fields were derived by feature-tracking topographic hillshades using OpenPIV (Taylor et al., 2010). Stress fields were derived as outlined in Section 2.2.3, with a 5 x 5 pixel median-filter on the input velocity fields introduced as an additional preprocessing step to reduce noise.

Surface classification

To date, UAV-based crevasse detection has been based on DEM-based topographic analysis (Florinsky and Bliakharskii, 2019; Ryan et al., 2015). Whilst these methods have been shown to be useful from a hazard assessment perspective (Florinsky and Bliakharskii, 2019), DEM-based methods alone cannot be used to identify features such as water-filled or healed crevasses, and crevasse detection is sensitive to threshold choice and ultimately the resolution of the DEM (Florinsky

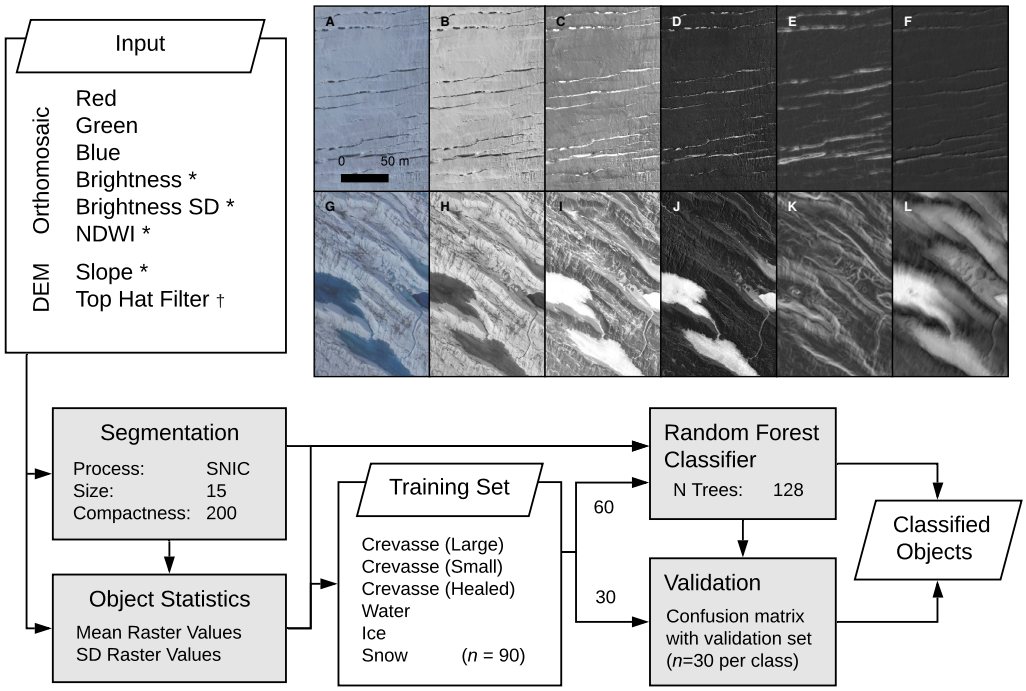

Fig. 5.3 Flowchart of method used to classify UAV imagery. Variables appended with an asterisk were calculated from input data within GEE, while those appended with a cross were calculated separately in Matlab. Inset shows examples of OBIA input data for regions dominated by small (a-f) and (g-l) large crevasses. (a and g) RGB orthophotos. (b and h) Brightness. (c and i) Standard deviation of RGB values. (d and j) NDWI. (e and k) Slope, with hillshade overlaid. (f and l) Black-top-hat filtered DEM, with hillshade overlaid.

and Bliakharskii, 2019; Jones et al., 2018). To take advantage of the high spatial resolution and multi-dimensional outputs of UAV surveys, we used a combination of object-based image analysis (OBIA) and supervised classification. OBIA is based not on the numerical characteristics of individual pixels but of objects (i.e. groups of meaningfully similar pixels segmented based upon spectral homogeneity (Blaschke, 2010)). This has been used successfully in a glaciological context by Kraaijenbrink et al. (2018, 2016b) for mapping cliff/pond systems and emissivity on a debris-covered glacier. We again used GEE to perform the full segmentation and supervised classification workflow (Figure 5.3).

We identified a number of variables that could be used as inputs for a supervised classification algorithm to identify crevasse field surface features. This included: the red, blue, and green values of the orthophoto (Figure 5.3a;g); the 'brightness'

(mean RGB values; Fig 5.3b;h) as per Kraaijenbrink et al. (2016b); the standard deviation of the RGB values, which highlighted water, small crevasses, and healed crevasses (Figure 5.3c;i); the NDWI, from blue and red pixel values (Figure 5.3d;j); the DEM slope, which effectively highlighted small crevasses on the order of a few metres (Figure 5.3e;k); and DEM values black-top-hat filtered with a 30 m structuring element (Kodde et al., 2007), which were useful in identifying large crevasses on the order of tens of metres (Figure 5.3f;l). A black top-hat filter morphologically closes the glacier surface at scales smaller than the structuring element, before subtracting the closed surface from the original data. This process was performed in Matlab prior to ingestion into GEE.

We performed image segmentation using Simple Non-Iterative Clustering (SNIC) (Achanta and Susstrunk, 2017), a computationally efficient implementation of superpixel-based clustering. Rather than segmenting an image into semantically-meaningful objects, superpixel-based segmentation simplifies the image into small, uniform, and compact clusters of similar pixels ('superpixels'), with a focus on boundary adherence. The variables described above are used as the input to the segmentation algorithm. We manually selected a seed spacing of 15 pixels (2.25 m) and a high compactness factor of 200. This resulted in superpixels small enough to display strong boundary adherence to small and healed crevasses at the scale of metres, whilst still clearly delineating the margins of larger features such as water bodies. As an input to the supervised classification, we calculated the average and standard deviation of values in each superpixel from the variables described above, as well as the perimeter-to-area ratio of the superpixel, and normalised the results.

We adopted a supervised classification approach to surface classification (Kraaijenbrink et al., 2018, 2016b; Ryan et al., 2018) by training a random forest classifier in GEE. In order to reduce the amount of redundant information used to train the random forest classifier, we performed a non-parametric mutual information (MI) test on our training data as a proxy for the predictive power of each input variable. Rejecting input variables beneath the median MI value (see Appendix C, Figure C.1) did not notably reduce the accuracy of the output data (see Appendix C, Figure C.2). Therefore, we used only the nine most significant variables as input to the random forest classifier. We constructed training datasets of 90 points each for six distinct surface types: bare ice, snow, healed crevasses, 'small' crevasses, 'large'

crevasses, and water. We seperated 'small' and 'large' crevasses (those with a diameter of metres vs. tens of metres) into two training datasets as they displayed distinctly different values for properties such as brightness, slope, and the top hat filtered DEM (Figure 5.3). We trained the random forest classifier on two-thirds of the dataset (60 points per classification) and retained one-third (30 points per classification) for validation. Output classification performed well visually (see Appendix C, Figure C.3) and validation data showed that a > 95% accuracy was observed for all surface types (see Appendix C, Figure C.2), apart from for snow and bare ice, which for our purposes was not important. Although we identified six surface types, for this analysis we were only interested in three distinctions: crevasses (combining 'small' and 'large' crevasses), ice (combining bare ice, snow, and healed crevasses), and water.

5.3 Results

5.3.1 Satellite results

From ArcticDEM elevation, Sentinel-2 optical imagery, and MEaSUREs surface velocity (Figure 5.4a), we created maps of crevasse fraction values (Figure 5.4b), water fraction values (Figure 5.4c), and stress estimates (Figure 5.4d–i) respectively.

Despite an intuitive relationship between first principal stress (σ_1) (Figure 5.4d; 5.5a) and crevasse formation, the measure is not a good predictor of crevasse state, i.e. whether a crevasse is initiating, dry, or wet. An analysis of the distribution of stresses shows that although all crevasse types occur at higher values of σ_1 than non-crevassed regions (Figure 5.6a), the three states display similar median values (wet 47 kPa; dry 48 kP; initiating 50 kPa), suggesting that σ_1 alone is not a strong control on crevasse hydrology. In contrast, second principal stress (σ_2; Figure 5.4e) displays a clearer relationship with crevasse state, with crevasses initiating in areas of highest σ_2 and ponding in areas of lowest σ_2 (Figure 5.5b). Initiating crevasses have the highest median σ_2 (-13 kPa) and are the most common crevasse state in regions of positive σ_2 (Figure 5.6b). In contrast, wet crevasses have the lowest median σ_2 (-58 kPa), and dry crevasses are intermediate between the two

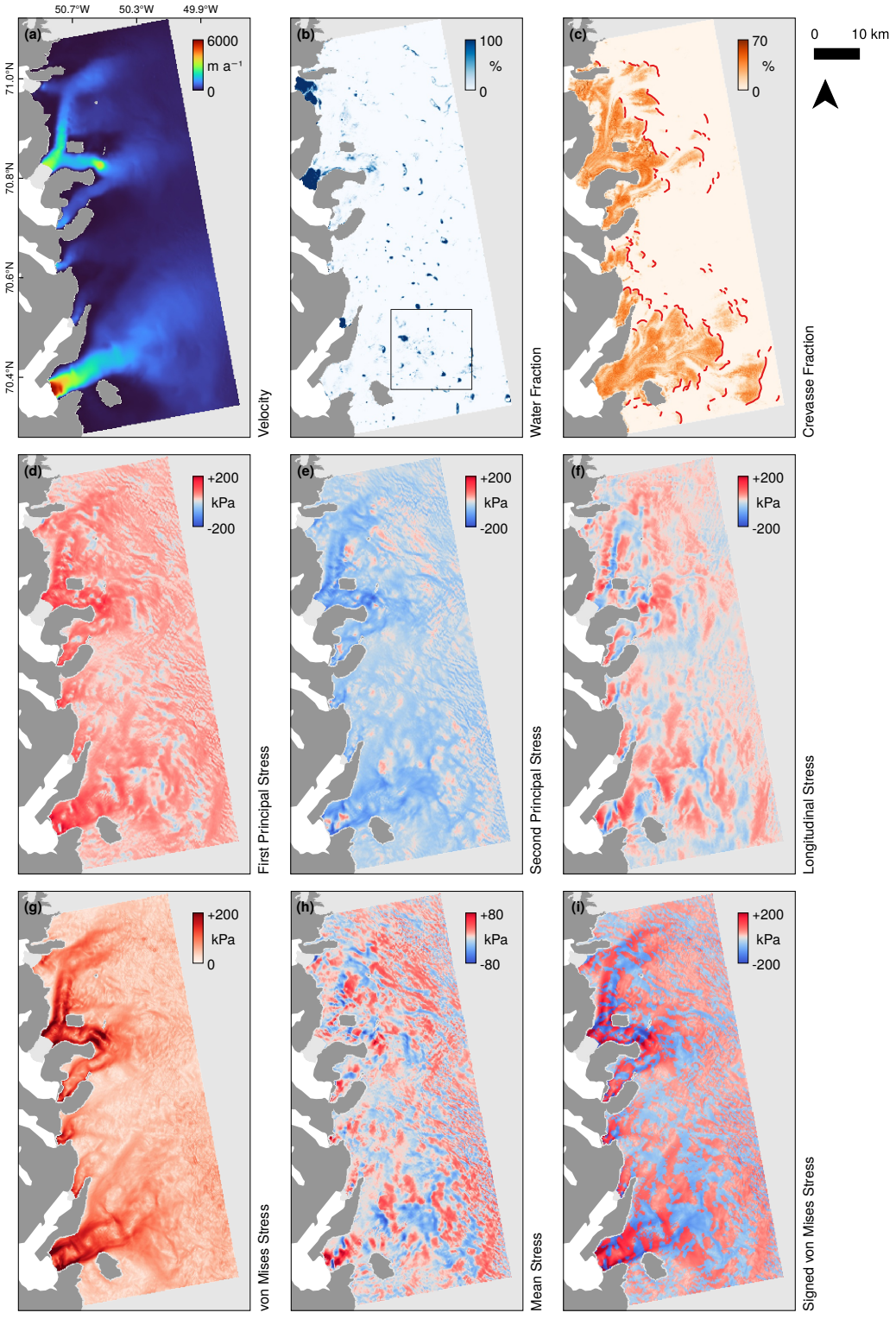

Fig. 5.4 (a) Map of MEaSUREs 2018 velocity data over the study region; (b) observed 2018 water fraction; (c) observed crevasse coverage, with manually identified crevasse initiation zones marked in red; (d) first principal stress, (e) second principal stress, (f) longitudinal stress; (g) von Mises Stress, (h) mean stress, and (i) signed von Mises Stress. Black box in (b) shows the location of Figure 5.5.

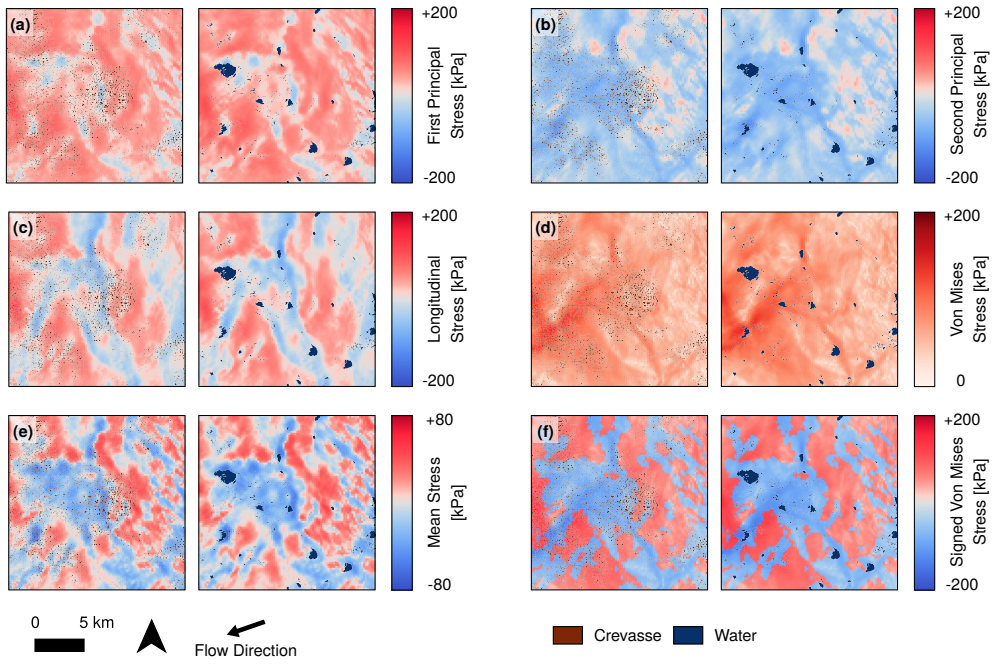

Fig. 5.5 Close-up of stress fields overlaid with observed crevasses (left) and water (right): (a) first principal stress, (b) second principal stress, (c) longitudinal stress; (d) von Mises Stress, (e) mean stress, and (f) signed von Mises Stress.

(-38 kPa). Longitudinal stress (σ_l; Figure 5.4f), is more successful at distinguishing crevasse state (Fig 5C; median wet 6 kPa; dry 18 kPa; initiating 33 kPa) than σ_1, but not as successful as σ_2 as it displays a narrower spread of median values, and dry and wet crevasse states display very similar distributions (Figure 5.4c). The effective performance of σ_2, and less effective performance of σ_1 and σ_l, suggest that structural controls on crevasse hydrology are distinct from those traditionally understood to control crevasse formation.

Stress criteria that encompass both σ_1 and σ_2 provide further insights into crevasse hydrology. Von Mises (σ_v; Figure 5.4g; 5.5d) has different median values for crevasse states (wet 88 kPa, dry 67 kPa, initiating 57 kPa), but with a counter-intuitive relationship given that the highest stresses appear to be the most likely to be water-filled. Additionally, dry and wet crevasses display a strong positive skew (Figure 5.6d), making it difficult to differentiate the two based on a single threshold. In contrast, σ_m values (Figure 5.4h; 5.5e) capture a distribution for each of the crevasse states: crevasse initiation is most likely to occur at the highest σ_m values (median +20 kPa), whilst water-filled crevasses are the only surface type to occur

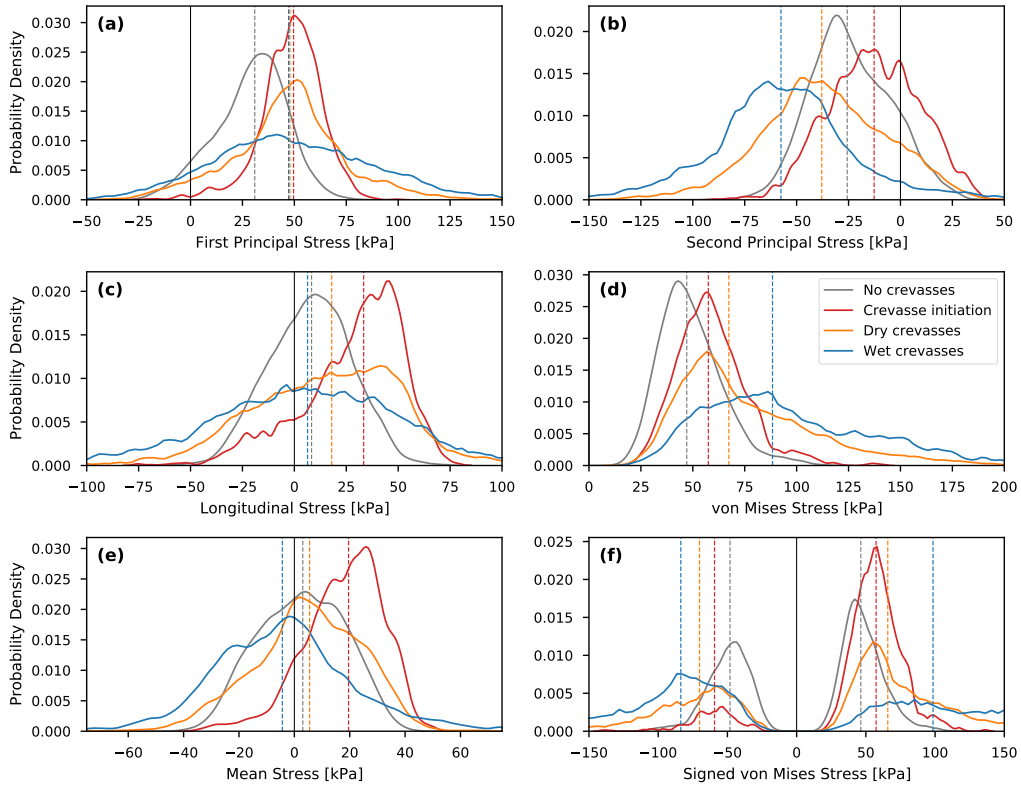

Fig. 5.6 Kernel density estimate distribution plots of different surface classifications for (a) first principal stress, (b) second principal stress, (c) longitudinal stress, (d) von Mises stress, (e) mean stress, and (f) signed von Mises Stress. Median values for different surface classifications are shown as dashed vertical lines. A crevassed grid cell is defined by > 1% crevasse fraction, and a wet crevassed grid cell is a crevassed grid cell with any water observed (> 0%).

with a median negative σ_m (-4 kPa). Qualitative assessment (Figure 5.4e) shows that saturated crevasse zones align with regions of negative σ_m and crevasse initiation zones align with strongly positive σ_m. However, σ_m is still not convenient for predicting crevasse state as the distributions of crevasse states display high overlap (Figure 5.6e) such that simple thresholding based on σ_m alone would not delineate crevasse state successfully.

In order to combine the relative strengths of σ_v and σ_m approaches, we use σ_{sv} which is derived as the magnitude of σ_v but with the sign of σ_m (Figure 5.4i). This measure allows for a more refined differentiation for whether a stress regime is compressive or extensional. Crevasse initiation zones display a particularly narrow distribution (Figure 5.6f) almost exclusively in positive σ_{sv} regimes (median

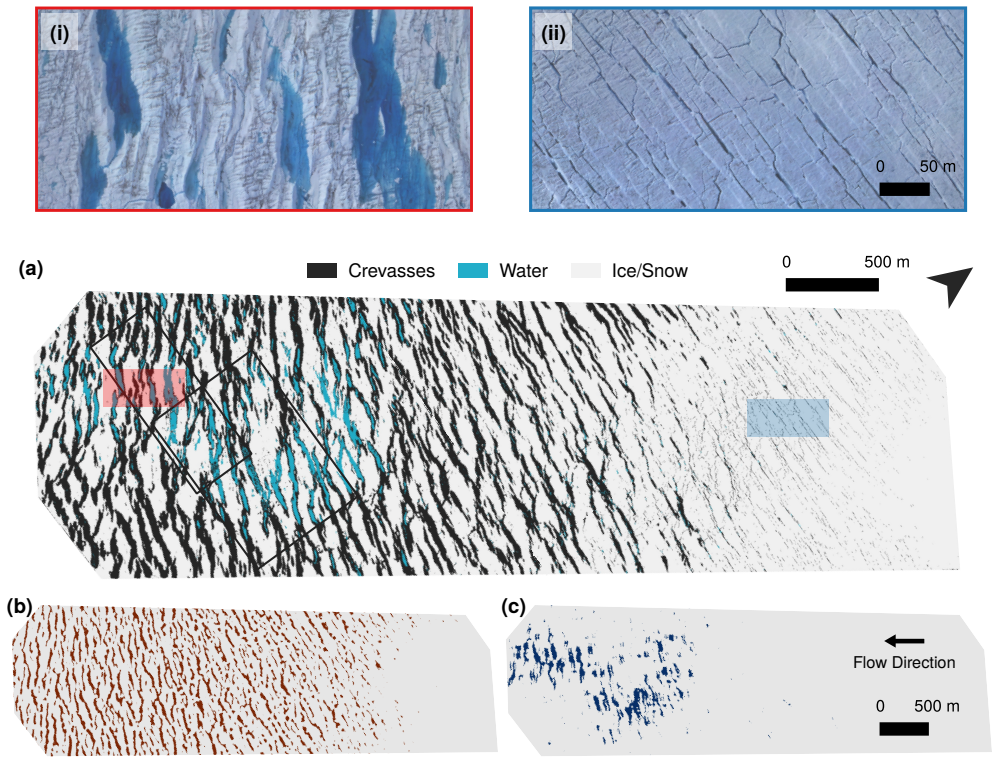

Fig. 5.7 Output of (a) UAV random forest classification, with insets (shaded in red and blue) showing (i) an area with large (50-60 m) crevasses, and (ii) small (2-3 m) crevasses. Satellite-derived data, shown for comparison, include (b) ArcticDEM-derived crevasse classification, and (c) Sentinel-2 derived water classification. Black boxes in (a) mark extents of Figure 5.9.

+57 kPa). Wet and dry crevasses can also be differentiated, even though these data exhibit a similarly skewed distribution in σ_v. When σ_{sv} is highly compressional (i.e., less than -50 kPa), wet crevasses are more likely than dry crevasses; above this value, the probability of crevasse state is approximately equal. Conversely, dry crevasses are more likely than wet crevasses to exist in extensional σ_{sv} regimes from low to high stress (up to 120 kPa). In very high positive σ_{sv} regimes (greater than 120 kPa), wet crevasses are once again more likely to exist.

5.3.2 UAV results

Analysis and comparison to satellite data

UAV surface classification (Figure 5.7a), based on high resolution orthophotos (0.15 m) and DEMs (0.2 m), was able to differentiate crevasses, water, and ice surfaces to a level of accuracy exceeding 90% (see Appendix C, Figure C.2). This suggests that the UAV SfM-MVS is highly suitable as ground verification for the coarser satellite-derived data, especially given the logistical difficulties of ground-based verification within hazardous crevasse fields. Comparison with satellite-derived crevasse classification (Figure 5.7b) and water classification (Figure 5.7c) shows that the datasets agree closely in terms of the distribution of surface features. Manual comparison between the two datasets suggests the cutoff width below which crevasses are unable to be identified from ArcticDEM v3 data is approximately 10 m , corresponding to 5 pixels. Although this means the satellite data do not capture the smallest crevasse fields, the resolvable size of a crevasse is approximately equal to the resolution of the Sentinel-2 bands used for NDWI calculation (10 m), which gives confidence that the two datasets are comparable. While our ArcticDEM mosaic is derived from multitemporal data (individual tiles across the study area range from 2009-2017), crevasse sizes and patterning observed in 2018 UAV surveys were consistent with the 2009-2017 ArcticDEM (Figure 5.7a cf. 5.6b). This suggests that, even though individual crevasses advect, interannual variation in crevasse fields is relatively small, and that the assumption that 2009-2017 crevasse distribution can be compared to 2018 surface water distribution is valid. Sentinel-2 water and UAV-derived water also agree (Figure 5.7a cf. 5.6c). Individual water-filled crevasses are able to be co-located between the satellite and UAV datasets. Sentinel-2 data additionally identifies additional crevasses that are water-filled across the span of the season yet not filled on the date of the UAV survey.

Stress components evaluated from UAV velocity data, including σ_m (Figure 5.8a) and σ_{sv} (Figure 5.8b), reveal a highly heterogeneous stress regime, where changes can be seen even between neighbouring crevasses. However, in general, an extensional regime dominates in the northeast (right-hand side of Figures 5.6 and 5.7) and a compressive regime in the southwest. As with satellite-derived data, there are clear relationships between the nature of the positive/negative mean stress

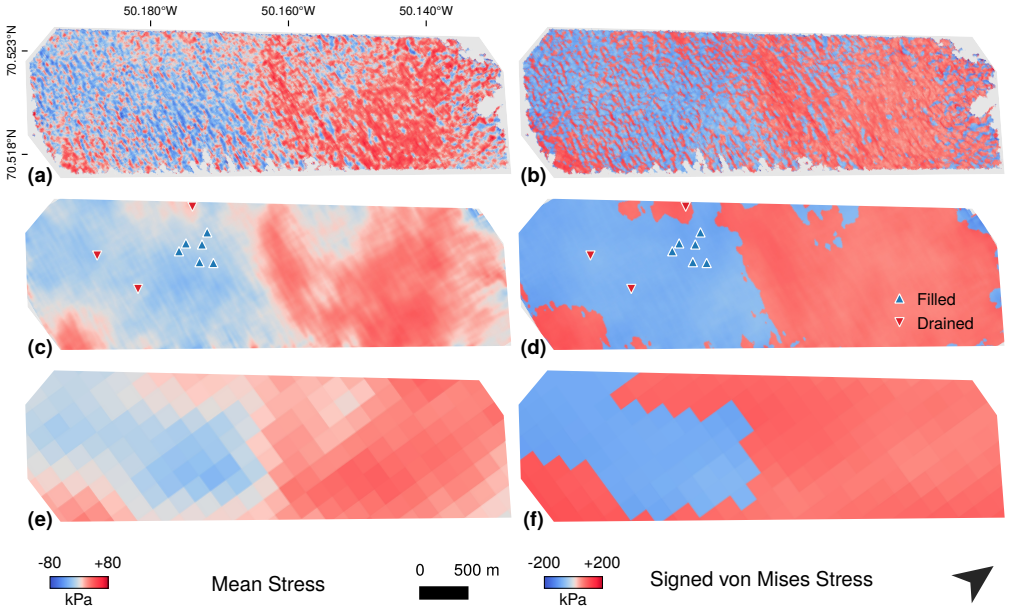

Fig. 5.8 UAV-derived stress outputs for mean stress (left column) and signed von Mises stress (right column). (a–b) shows raw output, (c–d) shows 200 m mean average, and (e–f) shows MEaSUREs-derived output for comparison. Triangles in (c–d) show the locations of crevasse systems that were observed to fill (blue) or drain (red) across the UAV survey period.

regime and that of crevasse initiation and water distribution. Crevasses tend to initiate - or at least become identifiable in the decimetre resolution data - in the upstream kilometre of the study zone (Figure 5.7a). In the next kilometre down-glacier, crevasses open from < 3 m wide to full size (∼10–60 m wide) by the centre of the study zone (Figure 5.7a insets). Crevasse initiation and opening is coincident with a zone of highly positive mean stress, consistent with satellite-derived observations (Section 5.3.1). In the southwestern sector of the study zone, crevasse size remains relatively stable, but crevasses transition from dry to water-filled in the down-glacier direction (Figure 5.7a). This region of water-filled crevasses is seen where the mean stress regime is negative (Figure 5.8a–b), which is again consistent with satellite datasets.

The stress regime as estimated from UAV-derived velocity fields is highly variable on the scale of tens of metres, making it difficult to compare to the stress regime estimated from MEaSUREs data. To address this, we apply a 31 pixel (198.4 m) mean filter across the UAV stress fields (Figure 5.8c–d) to approximate the 200 m

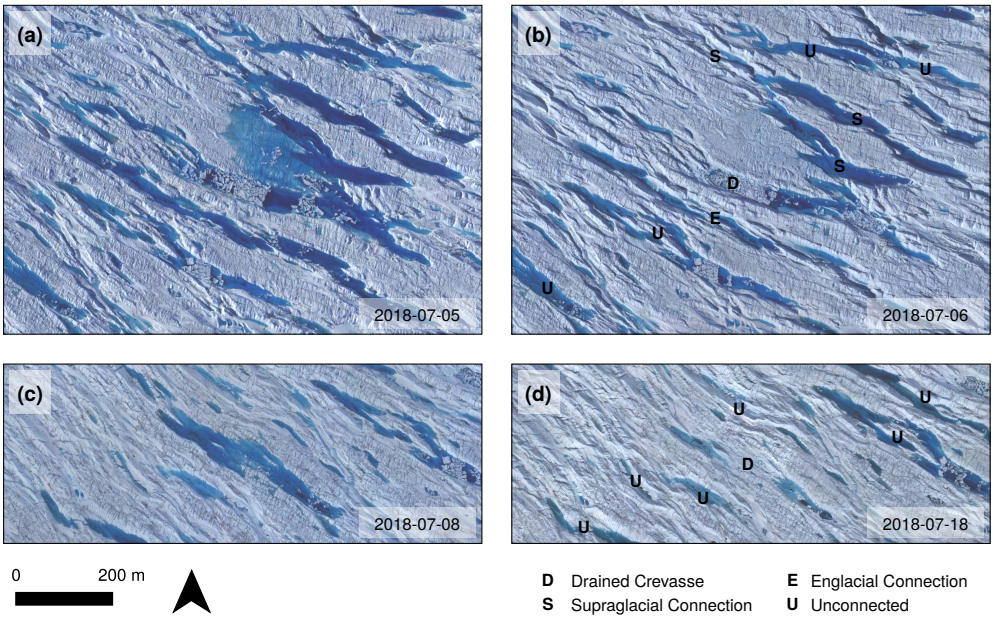

Fig. 5.9 Examples of crevasse drainage when (a–b) a draining crevasse is supraglacially and/or englacially connected to adjacent crevasses and (c–d) when no connections are present. Interpretations are marked where crevasses underwent direct drainage (D), drained via supraglacial connection to a draining crevasse (S), drained via englacial connection to a draining crevasse (E), or remained unconnected to a draining system (U).

resolution of the MEaSUREs stress field (Figure 5.8e–f). The results show that the UAV and MEaSUREs data are in close general agreement, despite the different spatial resolution (6.4 m vs 200 m) and timescales over which velocity was captured (10 days vs 1 year composite). This reveals that crevasse fields exhibit high local variability in surface stresses (on the scale of 10s of metres) that cannot be captured by satellite observations. For instance, in the southwestern sector of the study zone, there are many localised areas of positive stress, despite the fact that MEaSUREs data is consistently negative. This suggests that one source of uncertainty in the satellite analysis is the degree to which localised variability occurs within its 200 m grid cells.

Water routing in ponded crevasse fields

Satellite-derived analysis (Section 5.3.1) identified regions of wet crevasses in compressive mean stress regimes, but did not provide information as to whether or how water is routed to the bed in these areas. Over the 13-day period in July 2018 over which repeat UAV surveys were undertaken (see Appendix C, Table C.1), three crevasse systems in the UAV ROI were observed to drain, and six underwent significant filling. The locations of these events are correlated with mean stress regime (Figure 5.8c–d). For instance, crevasse water filling was observed in a region that had recently advected from a net extensional into a net compressive zone. Elsewhere, crevasse drainage was observed in a region that had recently advected from a net compressive area (where $\sigma_m < 0$) into a net extensional area ($\sigma_m > 0$), and also in locations where the 200 m-resolution stresses were observed to be negative but local stresses displayed high heterogeneity (cf. Figure 5.8a–b; c–d). This suggests that, in general, crevasses fill with water when advecting into a negative mean stress regime, and display a higher propensity to drain when advecting into a region of positive mean stresses.

Closer analysis of these draining crevasses revealed two key observations regarding water routing. First, there was little evidence to suggest that surface water was routed for significant distances between crevasses in crevasse fields. Where supraglacial streams existed, connecting larger crevasses, they were easily identified in the imagery (see Appendix C, Figure C.4a), but this is not common across the survey zone. In one case, a crevasse system that was overflowing with water (Figure 5.9a) formed local supraglacial networks, and upon one crevasse draining, water levels across the entire network dropped (Figure 5.9b). This event appeared to result in the formation of incised channels in the days following drainage (see Appendix C, Figure C.4b–c). It was less common for adjacent crevasses to drain when no surface routing was visible (Figure 5.9b), and indeed individual crevasses were able to drain without affecting water levels in the surrounding crevasses at all (Figure 5.9c–d). This suggests that supraglacial and englacial hydrological connections between crevasses may be rare. Second, crevasse drainages appear to be rapid. Of the three drainages we identified, two represent crevasses that were stable or filling in sequential imagery prior to drainage, before losing a majority of water between two adjacent images (e.g. Figure 5.9c–d). One crevasse system lost a substantial volume of water in less than 24 hours (Figure 5.9a–b),

and water levels continued to drop for the rest of the survey period (see Appendix C, Figure C.4b–c). This suggests that either a moulin had formed, and that water therefore continued to drain into the subglacial system, or that small open fractures continued to transfer water inefficiently into the englacial system.

5.4 Discussion

5.4.1 Relationships between surface stress and observed crevasse hydrology

Our findings show that stress measures previously used to predict water drainage through crevasses - including the first principal stress (Poinar et al., 2015; Williamson et al., 2018b), longitudinal stress (Clason et al., 2015), and von Mises stress (Everett et al., 2016; Koziol et al., 2017) – are not good at estimating the hydrological state of crevasses. Longitudinal stress (σ_l) is effective at predicting where crevasses initiate, which aligns with the assertion that crevasses can be considered as Mode I fractures that open up perpendicular to the direction of flow when stress in this direction exceeds a certain threshold. However, the fact that both first principal stress (σ_1) and σ_l are poor at predicting crevasse hydrology, whilst second principal stress (σ_2) performs better, suggests that the full range of normal stress, and not only the stress acting in the direction of flow, affect the ability of water to drain englacially. The von Mises (σ_v) criterion, which accounts for only the deviatoric stress, does not clearly distinguish crevasse hydrological state compared to alternative measures which incorporate the full first invariant stress (e.g. mean stress). Additionally, σ_v displays an inverse relationship to hydrology, whereby higher σ_v values are more likely to see water ponding occur (Figure 5.6d). This is counter-intuitive when considering σ_v as a planform equivalent to a σ_{xx} in an LEFM framework, where high positive σ_{xx} values (tensile stress) are associated with greater fracture propagation (Van der Veen, 1998). We suggest this is because the von Mises stress does not differentiate between a compressive or extensional stress regime. In contrast, stress measures that account for the magnitude and direction of the full first invariant stress (i.e. mean stress, σ_m, and signed von Mises stress, σ_{sv}) were better at predicting surface crevasse hydrology. Surface crevasses

that were identified to be water-filled through the 2018 ablation season were more likely to exist in regions where mean surface stress was negative (i.e. compressive). In contrast, surface crevasses where no water was observed were more likely to exist in positive (i.e. extensional) mean stress regimes. To explain this link, we interpret that in negative mean stress regimes, hydrological pathways between the surface and active englacial system will likely be subject to enhanced closure. This will be the case regardless of the stress acting in the direction perpendicular to crevasse orientation (Section 5.4.2.1).

There has been limited consideration of the role of the full first invariant stress in crevasse hydrology, with most studies focussed on first principal or longitudinal stress. A few studies have considered the role of σ_2 in crevasse formation (Cuffey and Paterson, 2010; Hambrey and Müller, 1978), and indirectly in studies of Mode II (van der Veen, 1999) and Mode III (Colgan et al., 2016) shear in mixed-mode crevasse formation. Whilst LEFM modelling can, in theory, be extrapolated to two or even three dimensions (van der Veen, 1999), this is nontrivial (Colgan et al., 2016). As a result, studies modelling water transmission to the bed have tended to extrapolate from 1-D LEFM models by directly replacing the σ_{xx} stress term with pre-existing measures that have been recommended for crevasse formation - in particular, the von Mises stress, following Vaughan (1993). Our work suggests that this can be improved upon, and that accounting for crevasse hydrology requires a more complete consideration of stresses, i.e. both surface-parallel principal stresses.

5.4.2 Crevasse drainage mechanisms

Wet crevasses

A number of drainage processes could be consistent with observations of water-filled crevasses. For instance, water-filled crevasses in compressive regions can be part of an active supraglacial network, with water being routed to a moulin elsewhere in the system (Poinar, 2015). However, the UAV data presented here suggests that, where crevasses are large, significant hydrological connections between them are rare and of limited spatial extent (Figure 5.9b,d). Even where hydrological connections exist, they appear to form as a consequence, rather than

a cause, of drainage events (see Appendix C, Figure C.4b–c). If channels do not exist in many cases, the drainage of water in ponded crevasse systems cannot, for the most part, be caused by water being routed to moulins via supraglacial networks.

Given that we found little direct evidence for hydrological connections, we consider hydrofracture to the subglacial environment to be the most likely mechanism by which water-filled crevasses drain (Boon and Sharp, 2003; Krawczynski et al., 2009; van der Veen, 2007; Weertman, 1973). In negative mean stress regimes, we assume that englacial connections undergo what Irvine-Fynn et al. (2011) described as 'pinch-off', whereby crevasse closure or ice creep can isolate the ponded crevasse from the englacial drainage system. In an environment where ablation is ongoing, this will result in the filling of surface crevasses, allowing hydrofracture to occur when water depth reaches a critical level. This would be consistent with the rapid and heterogenous crevasse drainages observed in UAV data, and align with the numerous observations of hydrofracture occurring during rapid lake drainages (Chudley et al., 2019b; Das et al., 2008; Doyle et al., 2013; Stevens et al., 2015).

The state of a subglacial drainage system and subsequent ice dynamic response is known to be affected by the variability (Schoof, 2010) and distribution (Banwell et al., 2016) of meltwater inputs. Our evidence indicates that episodic crevasse drainage events should be expected to deliver distinct, isolated pulses of meltwater to the bed in the same fashion as - but likely smaller than - rapid lake drainages. The full hydrological consequences of rapid lake drainages are explored in detail elsewhere (e.g. Nienow et al., 2017), but it is apparent that similar principles can be applied to crevasse drainages. For instance, studies focussing on draining crevasse systems at the shear margin of Jakobshavn Isbrae have established that water delivery is of sufficient volume to overwhelm the capacity of the subglacial system (Lampkin et al., 2013), increasing ice mass flux across the shear margin and enhancing glacier discharge (Cavanagh et al., 2017; Lampkin et al., 2018). However, there may be several features of crevasse drainages that are distinct from better-studied lake drainage events. After hydrofracture, ongoing meltwater delivery via the newly open moulin is an important hydrological component of lake drainages (Hoffman et al., 2018; Koziol et al., 2017) but, given the smaller catchments that individual crevasses have, this effect is likely less important in crevasse

drainage scenarios. Unlike lakes, it appears to be relatively common that crevasse systems can drain multiple times through a single ablation season (Cavanagh et al., 2017). However, the net effect of this has yet to be properly considered.

Dry crevasses

As water is never observed to pond in the crevasses we classify as 'dry', surface meltwater produced within the crevasse catchment must either (i) drain via moulins to the glacier bed, or (ii) drain less efficiently into the englacial system, but still rapidly enough that water is never collecting at a rate sufficient to fill the crevasse. We argue that the second interpretation is more likely. Whilst it seems unlikely that discharge rates are sufficient to maintain open moulins, positive mean stress regimes may mean that, unlike in compressive environments, creep closure does not close narrow hydrological pathways to the englacial system. This is consistent with the view of crevasse systems on temperate valley glaciers as continually, albeit inefficiently, hydraulically connected to englacial and/or subglacial drainage systems through a linked network of small fractures (Fountain et al., 2005).

This conceptual model of inefficient, continuous crevasse drainage has previously been applied to the Greenland Ice Sheet by Colgan et al. (2011) and McGrath et al. (2011). Both studies assumed that water reaches the bed, albeit slower than through moulins. Colgan et al. (2011) suggested the difference may be 200-fold between the two types of surface-to-bed connection ($\sim$1 hour for a 1 m^2 moulin vs. $\sim$12 hours for a 0.1 m wide crevasse), whilst McGrath et al. (2011) suggested that crevasses may slow englacial drainage to such an extent that a diurnal cycle of meltwater input can be damped to a quasi-steady-state discharge on the timescale of hours-days. This sustained inefficient delivery of meltwater to the glacier bed through crevasses would be less likely to overwhelm the transmission capacity of the subglacial system. Therefore, they argue that regions of the bed subject to continuous inefficient delivery are less likely to exhibit enhanced basal sliding compared to regions experiencing episodic, efficient meltwater pulses.

There is no direct evidence, however, that water draining inefficiently through crevasses is able to reach the bed of the Greenland Ice Sheet. Another likelihood is that much of this water does not make it to the bed, and instead freezes englacially. This has consequences for the thermal structure of glaciers, as it has been argued

that widespread, inefficient meltwater delivery through open crevasses would facilitate cryo-hydrologic warming relative to regions fed by discrete moulins (Colgan et al., 2011). This is because a dense spacing of hydrological pathways increases the volume of ice warmed by the latent heat release of englacial freezing, and hence can act to enhance ice velocity via deformation (Lüthi et al., 2015; Phillips et al., 2010). In contrast, episodically-draining, water-filled crevasses may focus cryo-hydrologic warming into the upper few hundred metres of the ice column (Poinar, 2015), and open moulins provide little latent heat to the surrounding ice (Lüthi et al., 2015). As such, it is likely that crevasses that drain continuously into the ice sheet may act to enhance latent heat delivery relative to other hydrological pathways. Colgan et al. (2011) concluded that increased crevasse coverage on an accelerating ice sheet would increase the area of the bed experiencing enhanced cryo-hydrologic warming. Based on the findings presented here, it might be expected that an accelerating ice sheet would result in a transition of some crevassesed regions from episodic to continuous drainage if the mean stress were to become positive (extensional). If this is the case, some areas of the bed could experience a transition to enhanced cryo-hydrologic warming, even in regions where crevasse fields already existed.

5.4.3 Implications for large-scale ice sheet modelling

Neither of the two states of crevasse drainage described above is new, with both episodic full-depth hydrofracture and continuous englacial drainage having numerous examples of observations and model implementations in literature focusing on the Greenland Ice Sheet. Nevertheless, in the past, regional models of ice sheet hydrology and dynamics have rarely included crevasse drainage (Arnold et al., 2014; Banwell et al., 2016, 2013). Recent 2-D regional hydrological models have begun to include the process, but have yet to account for heterogeneous drainage styles. Clason et al. (2015) incorporated crevasse drainage in a manner similar to the episodic hydrofracture described above. They identified crevassed regions based on a σ_v threshold, which were then allowed to fill and hydrofracture according to an LEFM model (van der Veen, 2007). Once a crevasse fractured to the full ice thickness, a moulin formed and water was transferred continuously to the bed. More recently, Koziol et al. (2017) based their model on the principle of

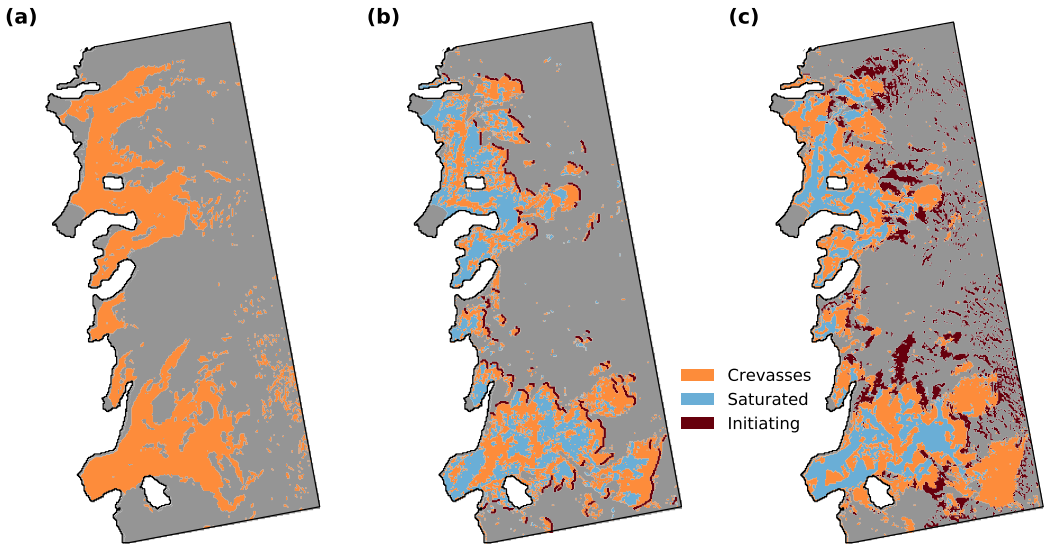

Fig. 5.10 Comparisons of methods of using stress thresholds to identify crevassing. (a) Predicted distribution of crevassing using a von Mises yield threshold of 67.5 kPa. (b) Observed distribution of crevasse-filled pixels (crevasse fraction > 1%) , crevasse-filled pixels where water is observed , and manually identified crevasse initiation zones. (c) Predicted location of water-filled crevasses and crevasse initiation zones based on signed von Mises thresholds.

continuously draining crevasses, whereby meltwater produced at the surface of crevasse fields (again identified according to a σ_v threshold) drained immediately without requiring hydrofracture. This water was assumed to reach the bed of the ice sheet without freezing englacially. These two studies, reflecting a paucity of observations, assumed that all crevasse drainage falls into one of the end-members of crevasse hydrology observed and described here.

Given the above, we are able to use the findings of this study to provide recommendations as to how future studies may be able to account for a wider diversity of crevasse hydrology whilst keeping inputs and classifications as simple as possible. We compare our results to the common method of crevasse field prediction via a qualitatively identified von Mises stress threshold. A threshold yield strength of 67.5 kPa was determined to result in the best visual match between predicted (Figure 5.10a) and observed (Figure 5.10b) crevasse fields. This method provides a reasonable first-order estimate but is (i) poor at predicting marginal cases including zones of false negative results in regions of relict crevasses, and (ii) cannot distinguish between zones of episodic and continuous drainage as iden-

tified in this study. Accepting that zero stress models cannot account for relict crevasse advection (Mottram and Benn, 2009), we retain the use of our own direct observations rather than using stress thresholds to predict crevasse location (Figure 5.10c). This is achievable for future studies as the method we use is simple and relies only on ArcticDEM data. Then, based upon the stress distribution of surface types (Figure 5.6f) and visual matching with observed distribution (Figure 5.10b), we prescribe that water-filled crevasses exist in MEaSUREs grid cells where σ_{sv} is less than -65 kPa or greater than +140 kPa (Figure 5.10c). On a pixel-by-pixel level, these thresholds are able to predict the presence or absence of water in 63% of crevassed grid cells correctly. Visual comparison shows that this thresholding technique provides a good match with broad trends in crevasse ponding. This includes the diagonal band of ponding across the tongue of Store Glacier, a bias of ponding towards the shear margins of the northern tributary of Perlerfiup Sermia, and even some of the specific localised patterns further upstream into the drainage basin at Store Glacier. This suggests that simple thresholding such as this could be used as input to regional hydrological models to investigate the seasonal and long-term effects of spatial heterogeneity in crevasse hydrology on the subglacial dynamics of the ice sheet (see, for example, Poinar et al., 2019).

In another example of implementing signed Von Mises stress as an improved simple stress threshold, we use the distribution of stresses in manually identified crevasse initiation zones (Figure 5.4e) to prescribe a yield criterion of +55 kPa for crevasse initiation (Figure 5.10c). This falls within the 30-90 kPa bounds predicted by (Van der Veen, 1998), but is lower than the 67.5 kPa we prescribed for von Mises stress alone, as well as those thresholds used by other studies (e.g. Clason et al., 2015; Koziol et al., 2017). By using a directional measure of stress, a relatively low critical yield criterion can be prescribed without enhancing regions of false positive identification in compressive stress regimes. Initiation zones are clustered where anticipated, at the upstream margins of crevasse fields, which gives us confidence in this threshold. There also exist scattered initiation zones at the farthest inland regions of the study area, where crevasses are not observed in our ArcticDEM-derived dataset. However, examination of higher-resolution Sentinel-2 data reveals that there are visible crevasse features here, not identified within the study due to either being too small to appear in ArcticDEM data or snow-filled.

The regional observations presented in this study utilise bulk analysis of annual velocity and seasonal water presence to identify potential links between crevasse hydrology and stress regime. Future work should explore opportunities to better define this relationship using time-series datasets. For example, the proliferation of remote sensing platforms has allowed for the production of ice velocity datasets at extremely high temporal resolutions (e.g. Minchew et al., 2017), as well as the ability to track the filling and drainage of individual hydrological systems on the surface of ice sheets (Williamson et al., 2018a). These advances highlight the possibility of being able to relate the behaviour and drainage of crevasses with time-variable stress regimes induced by short-term instabilities in ice dynamics - as has been previously proposed from a modelling perspective for supraglacial lake drainage events (Christoffersen et al., 2018) - and hence provide new insights into the relationship between crevasses and the delivery of meltwater to the bed of ice sheets.

5.5 Conclusions

In order to be able to model and predict the response of GrIS dynamics to increasing runoff, it is necessary to understand where and how water is transferred to the bed of the ice sheet. Our results indicate that surface stresses, and in particular the mean normal stress, determines whether crevasses drain episodically via hydrofracture, influencing basal sliding, or drain inefficiently into the englacial system, enhancing cryo-hydrologic warming via refreezing. Our observations suggest that crevasse drainage state exists on a spectrum that is controlled by spatially heterogeneous surface stress. We find that these behaviours cannot be distinguished based upon the yield criterion previously used to predict crevasse distribution, suggesting that controls on crevasse hydrology are distinct from controls on crevasse initiation. Simple thresholds obtained from visual analysis remain, however, a suitable approach to predict the first-order distribution of crevasse hydrological state. Hence, we can recommend mean stress thresholds as a simple and practical method for improving the representation of crevasse hydrology in regional hydrological models, which is necessary to be able to accurately model the spatially variable impact of seasonal ice sheet hydrology on the thermal regime and ice dynamic behaviour of the Greenland Ice Sheet.

Chapter 6

Synthesis and Conclusions

In the preceding three chapters, this thesis has attempted to address the fundamental aim of developing and exploring the potential of UAVs to gain further understanding of the relationship between the hydrology and dynamics of the marine-terminating GrIS. The three goals were set in Chapter 1: to (i) develop a new method of inferring short-term, high-resolution glacier velocity fields that are not typically wells-served by traditional satellite nor GNSS method; and to use this method to investigate hydro-dynamic interactions at (ii) lake and (iii) crevasse environments. These goals were addressed in Chapters 3–5 respectively. This chapter aims to place these developments into a broader context, identify the limitations of the work, and suggest directions for future research. The first section deals with the methodological implications of the workflows developed in this thesis, and the second the glaciological implications of the findings, before a final summary and conclusion is made.

6.1 UAVs

6.1.1 Advances made in this study

The first objective of this thesis was to establish and validate a method of UAV photogrammetry suitable for producing short-term (∼daily) glacier velocity fields in areas where GCP networks are impractical, if not logistically impossible. This

was motivated by the degree to which traditional techniques for measuring ice motion prove logistically challenging at marine-terminating glaciers, which are more difficult to access and operate on than slow-flowing, land-terminating sectors of the ice sheet. In Chapter 3, a viable alternative option, utilising carrier-phase GPS to geolocate camera positions in the SfM-MVS workflow, was described. It was shown that this allows for precise and robust observations of short-term glacier dynamics, sensitive to ∼decimetre-scale displacements (∼1.1 × the GSD horizontally ∼1.3 × vertically) in environments that would be unsuitable for ground-based observations, including calving fronts and crevasse fields.

One major advantage of the method developed in this study is that, at approximately GBP 1500 unit^{-1}, it continues to utilise the low-cost, self-built ethos that has characterised the use of UAVs in the earth and environmental sciences. This was partly out of necessity: at the beginning of this project, no commercially available UAVs were available with on-board carrier-phase GNSS receivers that could provide kinematic correction capability. However, as of 2020 it is now standard for companies providing commercial UAVs for surveying to offer a kinematic option - fixed-wing examples include the QuestUAV DATAhawk^{PPK}, the WingtraOne, and the eBee Plus. This means that direct geolocation methods will now be available to research groups who are not able to dedicate the resources to maintaining in-house UAVs. This is not to say that in-house development is now defunct, as the UAVs built in this study can be produced for an order of magnitude less than the cost of an off-the-shelf kinematically-enabled UAV. As such, self-building provides a viable alternative for research groups not able to dedicate large amount of funds to an off-the-shelf option, or, as for the case in this thesis, where a hazardous operational environment means that cost-effective hardware redundancy is desirable.

Given the relatively recent proliferation of GNSS-AT as a method, there are still few published uses in glaciology outside of the work presented in this thesis. Jouvet et al. (2019) went on integrate the method of Chudley et al. (2019a) to perform large-scale precision surveys of Eqip Sermia in July 2018. They surveyed over 30 km^2 of ice, including two calving fronts and ice up to 6 km up the flowline - a scale that would be not be suitable for GCP-based geolocation. The high accuracies allowed for not only a large are to be surveyed but also for a 105-minute separation velocity field to be generated, highlighting the potential of UAVs (and in particular GNSS-AT) to capture hourly differences in velocity at fast-flowing

Greenlandic outlet glaciers. However, as identified in Chapter 3, this method opens up a variety of other sections of the cyrosphere for dynamic assessment, including the interior of Antarctica and ice caps, but also for the feature tracking of sea ice movement, which is challenging to achieve via satellite-based methods (Parno et al., 2019). Directly geolocated UAV-SfM surveys might be particularly suited for characterising glacier surge activity. Surge environments are particularly challenging for field-based operation whilst also in some instances changing on scales too rapid to qualify using satellite methods. The combination of optical and topographic data provided by UAV assessment would allow for a variety of surge parameters to be measured, from the development of crevasses through to changing dynamic parameters such as ice strain/stress.

6.1.2 Directions for future research

The primary limitation of the direct geolocation method used in this study is the dependency on single-frequency L1 GPS. This limits the baseline over which PPK can accurately determine location to $\sim$10 km, and necessitated a second on-ice base station for inland operation. Whilst this adaptation was suitable for the work performed in this thesis, ongoing advances in UAV technology allow for better endurance and the possibility of larger or more distant surveys. One recent advance is the availability of off-the-shelf lithium ion batteries (cf. less energy dense lithium polymer cells) suitable for use in UAVs, as used during the 2018 field season in this thesis. By making use of 2×16 Ah Li-Ion batteries, Jouvet et al. (2019) were able to produce a Skywalker X8 build that could fly up to three hours, or 180 km. This was used to survey the calving fronts of six outlet glaciers terminating in Inglefield Bredning in northwest Greenland. With such high endurance, flights could be based from the village of Qeqertat rather than at a field camp, saving logistical costs. However, calving fronts were located up to 25 km away, meaning that single-frequency kinematic processing was not suitable for accurate geolocation, and no GCPs were used, leading to high uncertainties that had to be partially mitigated by coregistration of scenes using stable bedrock areas. Alleviating this limitation requires the use of dual-frequency post-processing. Dual-frequency receivers are now becoming cheaper, lighter, and more widely available, particularly with the introduction of new civilian GPS frequencies in the L2C and L5 bands.

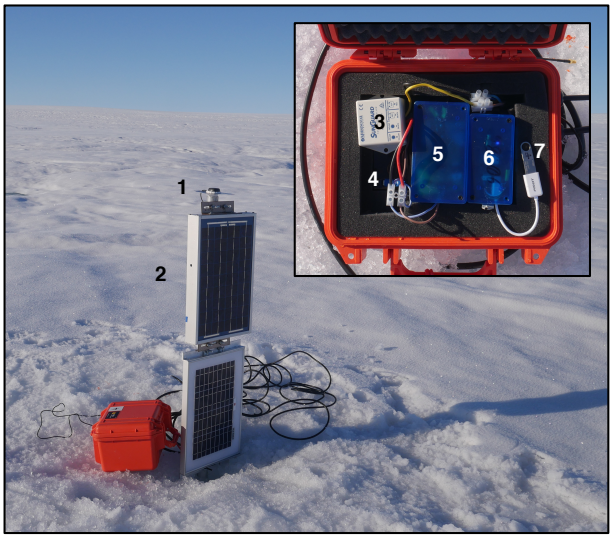

1. GPS Antenna
2. 2 x 10W Solar Panels
3. Solar Regulator
4. 12 Ah lead acid battery
5. 5V regulator and low voltage disconnect
6. GPS Receiver
7. USB Storage

Fig. 6.1 Set-up of L1 GPS receiver for measuring *in-situ* ice motion.

As identified in Chapter 3, there are now sub-USD 1000 dual-frequency receivers on the market, with some now specifically targeted at use in UAVs. These include the Piksi Multi, an L1/L2 receiver with an in-built IMU for full DSO, or the Emlid Reach M2, an L1/L2 receiver that is sub-$500. As these new low-cost receivers become integrated into UAVs, this should open up new opportunities for long-distance UAV surveying in the future, as well as reduce the cost of commercial off-the-shelf UAVs.

In the meantime, the availability of low-cost, light-weight, carrier-phase GNSS receivers provides new opportunities for integration into glaciological studies. Accurate geolocation of on-board data collection is not just useful for photogrammetry but, in combination with accurate IMU data, holds value for UAV-based LiDAR. This technique is beginning to see use in environmental science applications (Sankey et al., 2017), but requires accurate geolocation if UAV LiDAR data was to be applied to applications such as measuring surface mass balance. In an alternate application focussing on the GPS data itself, Jouvet et al. (2020) installed a single-frequency carrier-phase GPS receiver into a quadcopter. After landing in a highly crevassed region of Eqip Sermia, it acted as a ground-based GPS, measuring 70 cm of surface displacement over 4.36 hours. This shows how accurate geolocation data can open up alternate uses for UAVs, acting to deliver *in-situ* instrumentation for glacier monitoring.

Indeed, the increasing affordability of carrier-phase GPS receivers targeted at the UAV market brings into question their viability in measuring ice motion as more traditional continuous *in-situ* GPS receivers. In July 2018, four Emlid Reach units, designed for use in the UAV workflow, were installed at Store Glacier in an *in-situ* configuration (Fig. 6.1). Not only were these receivers cheaper than full dual-frequency units (sub-GBP 500 cf. >GBP 10,000), they were were smaller, lighter, and less power-intensive (and so required a smaller, lighter, 12Ah battery). Upon decommissioning in July 2019, data had been successfully collected, with only an expected data gap between November and April due to a lack of solar power in the winter. Although only single-frequency, and as such requiring correction against nearby (<10 km) base stations, the new availability of low-cost dual-frequency units holds potential for expanding this use case. Cheaper continuous GPS stations hold the potential to expand GPS coverage within a single study, for instance, by creating a 'grid' of many receivers, without increasing costs. Post-processing of the 2018–19 data to compare the final data quality against more expensive receivers is ongoing.

6.2 GrIS Hydrology and Dynamics

6.2.1 Advances made in this study

Supraglacial lake drainages

Despite over a decade of research into supraglacial lake drainages, there are still key questions surrounding their occurrence, and being able to predict the future evolution of supraglacial lake drainages on the Greenland Ice Sheet remains of ongoing value. From the observational record, it is known that lakes are responding to recent warming by advancing further inland, increasing in number and area, and draining more water (Cooley and Christoffersen, 2017; Howat et al., 2013). Although individual rapid drainage events may deliver only small fractions of total melt to the bed (Koziol et al., 2017) and induce mostly short-term dynamic accelerations (Stevens et al., 2015), research published since the beginning of work on this thesis has shown that they continue to be key in affecting the seasonal evolution of the drainage system (Andrews et al., 2018) and forming the majority of

moulins (Hoffman et al., 2018). However, studies to date have been unable to find any significant controls on lake drainage (culminating in the study of Williamson et al., 2018b), suggesting that although we may be able to model the future distribution of lakes (Ignéczi et al., 2016), translating this into predictions of rapid lake drainage may be non-trivial. By identifying additional factors modulating lake drainage, including inter-annual dependency and controls from the local strain regime, this work has identified new potential controls that may be able to be contribute to understanding how lake drainage behaviour may change in the future.

As the first study of a supraglacial lake in a marine-terminating context, this work can begin to inform the extent to which knowledge of lake drainages at land-terminating systems can be applied to faster-flowing sectors (Nienow et al., 2017). It is clear that rapid delivery of meltwater to the bed can still cause dynamic acceleration in the short-term, as has been observed in land-terminating on scales of hours to days (Doyle et al., 2013; Joughin et al., 2013; Stevens et al., 2015). Our observations of spatially distributed dynamics builds upon the acceleration observed by Joughin et al. (2013), with distributed uplift suggesting that transient water storage or localised inefficiencies may explain observed acceleration. It was also suggested that in regions of high positive background strain, lakes may be more prone to drain without requiring 'precursory activity' such as cascading transient stress perturbations from upstream (Christoffersen et al., 2018). Given that fast-flowing marine-terminating regions will experience larger regions under greater positive strain, cascading drainages may be less common in marine-terminating sectors, where more lakes can drain without requiring external influence. As discussed in detail in Chapter 4, it is possible lakes that exist in fast-flowing sectors may exhibit unique inter-annual variability due to the advection of structural weaknesses in the ice. This behaviour may also explain the inability of Williamson et al. (2018b) to find statistically significant differences between rapidly and non-rapidly draining lakes: if a significant proportion of rapidly draining lakes are controlled in part by behaviour in previous years, or are reliant on other lakes to 'trigger' drainage, looking at one year would be insufficient to identify patterns or controls. Hence, when returning to questions of glaciological controls on lake drainages, it may be more appropriate to consider the propensity of a lake to drain across a sample of years.

It is also worth considering the findings of Williamson et al. (2018b) in the context of Chapter 5. We find that different measures of stress perform variably when predicting crevasse formation and hydrology: given that the fundamental physics of hydrofracture remains the same, there is no reason to suspect this is any different for studies of supraglacial lakes. Williamson et al. (2018b) consider two measures, the first being the first principal strain rate, and the second being Von Mises stress. It may be, then, that consideration of alternative measures identified in this study, such as mean stress, may elucidate further controls on lake drainage. Additionally, they only examine the average strain/stress across the lake basin. In Chapter 4, it was shown that Lake 028 fractures from the west side of the lake where tensile strains are highest. Hence, the average strain/stress regime across the entire basin may not be relevant if hydrofracture needs only to exploit the ice under the greatest tensile strain/stress. In summary, although this study has highlighted a number of pathways forward in potential controls on rapid lake drainage, the number of complexities involved (with regards to individual lake setting, drainage history of the lake, and dependency on the behaviour of surrounding lakes) may make predicting the drainage of any specific lake in any specific year near impossible.

Crevasses

Knowledge of crevasse hydrology was, and remains, one of the most poorly understood aspects of the hydrological system of the GrIS. Whilst recent research has established that a significant plurality of meltwater makes its way the bed through crevasses (Koziol et al., 2017), it is still unclear how this varies in space and how it may vary into this future. The work in this thesis has provided new insights into the diversity and spatial distribution of crevasse hydrology, linking studies that conceptualise crevasses to inefficiently deliver water to the englacial system to those that conceptualise them to rapidly hydrofracture to the bed into a single coherent framework. This framework identifies two broad divisions: crevasses in compressive mean stress regimes, where englacial conduits undergo creep closure and water can pond, than drain episodically via rapid hydofracture to the bed; and crevasses in extensional mean stress regimes, where englacial conduits can remain open, than drain continuously but inefficiently into the englacial network. The concept that there may be spatial variation in the way meltwater is

delivered to the bed of the GrIS has not been previously considered in the published literature, and, as outlined in Chapter 5, may hold significant consequences for processes such as subglacial drainage system evolution and cryo-hydrologic warming.

This thesis has been been able to recommend simple but effective thresholds that allow for the estimation of crevasse routing style from estimations of background stress. Previous literature has used inconsistent stress measures to model crevasse drainage, including applying those used to predict crevasse presence. Chapter 5 has shown stress likely impacts the initiation and hydrological connectivity of crevasses in different ways, and alternative measures of stress may be more appropriate. This is particularly important given the recent debate surrounding the extent to which water may be able to be delivered to the bed at higher elevations of the GrIS, which has been proposed to be limited above 1600 m a.s.l. based on a threshold principal strain rate (Poinar et al., 2015). However, others have provided evidence for hydrological activity above this threshold based upon GPS (Doyle et al., 2014) and satellite (Cooley and Christoffersen, 2017) observations. It may be that alternative measures of strain/stress, as described in Chapter 5, could provide insight into limits of crevasse formation that are consistent with these observations. Better understanding of the relationship between surface stresses and crevasse hydrology is also important for building into hydrological models. At the current point in time, models that incorporate crevasses are rare (Clason et al., 2015; Koziol et al., 2017), but those moving forward will be able to utilise simple thresholds to incorporate the diverse conceptualisations of crevasse routing style. This will allow for better representation of crevasse heterogeneity into these models and allow for the quantification of the significance of spatially variable crevasse processes. Additionally, as discussed above, being able to better link surface stresses and crevasse hydrology may also prove of use when considering the spatial variability in the ability of supraglacial lakes to hydrofracture to the bed of the ice sheet.

Although Chapter 5 considered only the spatial variation of crevasse hydrology in a single ablation season, the findings are also significant when considering multi-annual variation. As crevasses are expressions of a glacier's dynamic regime, recent dynamic changes to the GrIS have resulted in parallel changes to crevasse extent. At Sermeq Avannarleq in west Greenland, crevasse extent has

been shown to have significantly increased (13% between 1985–2009) in response to ice thinning and steepening (Colgan et al., 2011). It may be the case that, if dynamic changes have introduced significant changes to the ice surface stress regime, there may also be changes to crevasse hydrology. In land-terminating regions, net slow-down (Tedstone et al., 2013; Williams et al., 2020) might be expected during a transition to an increasingly compressive regime. According to the framework developed in Chapter 5, this may result in more regions of the bed experiencing rapid, episodic delivery of meltwater via crevasse hydrofracture. In contrast, in marine-terminating sectors, where acceleration is occurring (King et al., 2018), it might be expected that crevasse fields transition to an inefficient drainage mode as extensional stresses increasingly dominate. Marine-terminating glaciers have exhibited particularly dramatic dynamic changes in recent decades (Catania et al., 2020), and so it may be that crevasse fields at marine-terminating sectors are particularly vulnerable to changes in drainage style.

6.2.2 Directions for future research

Supraglacial lake drainages

Work presented in Chapter 4 identified several previously unidentified features of a supraglacial lake drainage, including partial rapid drainage, intra-annual variation with a dependency on the previous drainage state, and a spatial distribution to dynamic uplift. However, the main limitation to these findings is the extent to which these features are generalisable across the GrIS. Upscaling these findings through the use of satellite remote sensing could help to identify what observations made in this thesis are of particular importance at an ice-sheet scale. In particular, three pertinent research directions are identified here.

The first direction is to assess the extent to which rapid supraglacial lake drainages are being under-identified due to partial drainages being discounted in previous remote sensing classifications. Cooley and Christoffersen (2017) have previously shown the sensitivity to thresholding that can occur when defining lake drainages as representing a specific proportion of area/volume loss within a set period. The work in this thesis may guide these thresholds towards prioritising water losses that are tightly temporally constrained rather than those representing high relative

losses of area/volume. This may be increasingly viable as more satellite observations become available, allowing for the integration of different datasets to provide a high temporal resolution (Williamson et al., 2018a). Alternatively, it may motivate alternate methods of remotely sensing lake drainages. It is challenging, but possible, to differentiate slow from rapid partial drainages, based on features such as visible fractures and the cutting off overflow drainage pathways (Fig. B4). Convolutional neural networks (CNNs) may be able to automate the identification of indicative features such as fractures and surface water. CNNs have only seen preliminary use in glaciological remote sensing through the identification of features such as calving fronts (Mohajerani et al., 2019), but have shown promise for object identification in a range of remote sensing applications (Alshehhi et al., 2017; Ding et al., 2018). By better refining existing methods, and incorporating new ones, it may be possible to quantify the extent to which rapid lake drainages have been underestimated.

The second direction is to properly account for the role of inter-annual variation. Few studies have produced multi-annual observations of rapid lake drainage events, and even fewer have addressed the interannual variability of rapid lake drainage events. Selmes et al. (2013) identified that, between 2005–2009, only 6% of lakes that drained rapidly did so every year, whilst 42% did so only once. Meanwhile, Morriss et al. (2013) identify that the majority of the 73 lakes they identify to drain do so in fewer than half of years. Whilst these data suggest that Lake 028's interannual variability may be more representative of many lakes than the persistently draining North Lake and Lake F, they do not address interannual variability on a lake-level scale. Deeper analysis would allow for the clarification of patterns observed at Lake 028. For instance: (i) do partial drainages occur exclusively in years following rapid drainages? (ii) Once a rapid lake drainage occurs, are drainages more like to occur in the following year? (iii) Is there a relationship between ice velocity and the occurrence of partial drainage? These questions can only be answered by looking at interannual variability on the scale of individual lakes.

The final direction is the further refining assessing the relationship between strain/stress and drainage. As discussed in Section 6.2.1, it may be the case that previous studies have not assessed all the possible ways in which strain/stress regime can affect supraglacial lake drainages. Potential routes to explore include

assessing the predictive capability of alternative stress measures such as mean stress, as well as considering the extent to which localised strain/stress state, rather than basin-wide averages, can lead to hydrofracture initiation. Additionally, no observational studies have considered the *direction* of strain/stress (be it first principal, longitudinal, etc.) in controlling drainage style. Following Chapter 4, it could be the case that, if background strain/stress rates control fracture direction rather than subglacial water flow direction (cf. Christoffersen et al., 2018), then regions where fractures initiate transverse to flow could be typified by intermittent rapid drainage. The importance of the magnitude of background stresses may also be key. Chapter 4 hypothesised that regions of high extensional flow may not require a precursory transient stress perturbation to initiate hydrofracture (allowing for the existence of 'trigger lakes'), whilst Chapter 5 showed that crevasse hydrology displays distinctly different behaviours under different stress regimes. Assessment of GrIS-wide, multi-year remotely sensed datasets will allow for these hypotheses and relationships to be tested at a regional scale.

Crevasse hydrology

Chapter 5 identified broad-scale relationships between crevasse hydrology and glacier dynamics across a single season, supported by high-resolution observations of a single crevasse field. However, a lack of detailed continuous observations of crevasse hydrology and strain/stress means that it is difficult to fully understand the mechanistic link between the two. Additionally, whilst drawing on the existing literature makes it clear that crevasses are important for both glacier hydrology and thermal regime, there is limited information as to the extent to which variation in crevasse extent and drainage style may impact ice sheet hydrodynamics. From these limitations, the following future research directions may wish to be investigated.

The first direction, as discussed in Chapter 5, relates to investigating crevasse-stress relationships at high temporal resolutions. Recently, time-series observations of lake area and volume have been collected at high ($\sim$daily) temporal resolution by taking advantage of multiple optical remote sensing platforms (Williamson et al., 2018a), and new cubesat constellations such as Planetscope provide the opportunity for daily observations at high spatial resolutions ($\sim$metres)

suitable for even smaller crevasses. These data could be paired with velocity datasets of high temporal resolutions (Minchew et al., 2017; Palmer et al., 2011) to investigate if stress thresholds for crevasse drainage could be inferred. Alternatively, field-based approaches could be taken. This may include a repeat-survey UAV campaign, or take advantage of ground-based approaches to get continuous records. Pressure transducers would be able to track water depth (see Chapter 4) and strain rates inferred from GPS measurements (Andrews et al., 2018) - perhaps taking advantage of low-cost GPS receivers in order to maximise coverage (Section 6.1.2). This will allow for an understanding of crevasse drainage dynamics at a time-variable local scale, better pairing the regional inferences made in this thesis with modelling approaches such as LEFM.

Moving from a local-scale approach, the second research direction should involve scaling up findings across multiple years and wider spatial coverage. Following Section 6.2.1, it is important to consider how changing GrIS dynamics could influence crevasse hydrology in the future. The historic record provides an opportunity to examine this, either through the use of historic aerial photography (Colgan et al., 2011) or long satellite records such as those from the Landsat programme. Changing crevasse hydrology could be linked to estimates of changing surface stress via new historic velocity datasets such as the NASA MEaSUREs ITS_LIVE project, providing velocity datasets of the GrIS back to 1985 (Gardner et al., 2019). Together, these datasets may provide some clues as to how changes may continue to occur in the future. Widening the coverage should not only be temporal, however, but also spatial. Expanding the coverage to the whole of the GrIS would allow for potential differences between land- and marine-terminating sectors to be ascertained (Section 6.2.1). Further afield, Antarctic ice shelves are another sector where there has been a close investigation into the relationship between surface stresses and meltwater penetration (Doake et al., 1998), and some of the findings raised in this thesis may also be applicable here.

Once the relationship between glacier dynamics and crevasse hydrology is better understood, the final proposed research direction would be to be able to quantify the glaciological impact using numerical modelling. 2D models of subglacial hydrology (e.g. Werder et al., 2013) are well-established for modelling the seasonal impacts of meltwater inputs to the GrIS, including through crevasses (Koziol and Arnold, 2018; Poinar et al., 2019). The opportunity to account for diversity in

crevasse hydrology using simple stress thresholds, as outlined in Chapter 5, will allow for a detailed assessment as to the degree to which subglacial hydrology may be impacted by surface stresses. Linking these models to future predictions of dynamic change may also allow for future changes to be quantified (Colgan et al., 2011). There will also be value in pairing numerical modelling of hydrology with that of thermodynamics (e.g. Lüthi et al., 2015; Phillips et al., 2013b; Poinar et al., 2017a), in order to quantify the potential variation in cryo-hydrologic warming that heterogenous crevasse hydrology may create. Between a more detailed understanding of the interaction between crevasse hydrology and surface stress, a large-scale understanding gained from the GrIS-wide historical record, and a quantification of the impacts using numerical modelling, the research directions described in this section will allow for the full consequences of the observations made in Chapter 5 to be understood, and potentially predicted into the future.

6.3 Conclusions

In this thesis, a low-cost workflow was developed for extracting UAV-derived velocity fields of glaciers and ice sheets at high spatio-temporal resolution, beyond the range of traditional satellite and GNSS methods, without requiring the use of logistically-intensive ground control. The resulting datasets were used to investigate the relationship between the hydrology and dynamics at the marine-terminating Store Gacier in West Greenland. Together with supporting data from *in-situ* instrumentation and satellite remote sensing, the causes and consequences of meltwater delivery to the bed of the Greenland Ice Sheet via lakes and crevasses were investigated at high spatio-temporal resolution.

By integrating a low-cost carrier-phase L1 GPS receiver into a fixed-wing UAV platform, images recorded as an input for SfM-MVS photogrammetry could be geolocated to centimetric accuracy. Validation showed that this technique was suitable to achieve horizontal uncertainties of $\pm$0.12 m ($\pm$1.1 $\times$ the GSD) and vertical uncertainties of $\pm$0.14 m ($\pm$1.3 $\times$ the GSD) when flying at $\pm$450 m above ground level. This level of accuracy is highly suitable for the production of glacier velocity fields with separation times of hours–days at fast-flowing sites such as marine-terminating outlet glaciers. This study was the first to integrate the GNSS-assisted

aerial triangulation for glaciological purposes, opening up new opportunities to assess glacier dynamics at spatio-temporal scales between the continuous *in-situ* measurements of ground-based GNSS receivers and the regional capability of satellite remote sensing.

The first observations of rapid drainage of a supraglacial lake in in a marine-terminating sector of the GrIS were made in July 2018 using data from repeat UAV surveys, ground-based GPS, pressure sensors, and seismometers. These data reveal several new aspects to drainage, some of which may be unique to lakes located in fast-flowing sectors of the ice sheet. UAV surveys show dynamic responses were observed to be greatest ∼4 km downstream from the lake, possibly related to regions of transient subglacial water storage. Interannual variability due to the rapid advection of fractures controlled key aspects of the drainage behaviour, including the resulting partial drainage, a feature that has previously been interpreted to result from slow (overtopping) drainage.

Investigations were made into the spatial variability of the hydrology of crevasse fields from a combination of UAV surveys and satellite remote sensing. Regions where crevasses were observed to pond through a melt seasons could be explained in terms of the mean surface stress regime, which were proposed to relate to rates of englacial conduit closure and subsequent connection the englacial drainage network. Using UAV surveys, ponding crevasses were interpreted to undergo episodic rapid drainage, whereas dry crevasses were seen to drain continuously but inefficiently to the bed. This suggests that spatially variable crevasse hydrology, as controlled by surface stresses, may have distinct consequences for subglacial hydrology and thermal regime. Simple recommendations were made as to how these findings could be directly implemented into regional hydrological models using simple stress thresholds.

Discharge from marine-terminating glaciers will remain a significant contributor to GrIS mass loss in the 21st century (King et al., 2018), and the extent to which hydrological controls will influence or modulate these changes is still largely unknown (Catania et al., 2020; Nienow et al., 2017). The observations presented in this thesis have enabled new insights into these interactions, describing new controls on, and consequences of, the delivery of meltwater to the bed in fast-flowing regions. Continued investigations are required to substantiate the extent to which

these patterns are applicable across the wider marine-terminating Greenland Ice Sheet, and to understand the extent to which they may change in the future.

References

Achanta, R. and Susstrunk, S. (2017). Superpixels and polygons using simple non-iterative clustering. In *Proceedings of the IEEE Conference on Computer Vision and Pattern Recognition*, pages 4651–4660.

Agassiz, L. (1847). *Système glaciaires, ou, Recherches sur les glaciers, leur mécanisme, leur anciènne extension et le rôle qu'ils ont joué dans l'histoire de la terre: leur structure, leur progression et leur action physique sur le sol. Nouvelles études et expériences sur les glaciers actuels. 1re partie*. V. Masson.

Alley, K. E., Scambos, T. A., Anderson, R. S., Rajaram, H., Pope, A., and Haran, T. M. (2018). Continent-wide estimates of Antarctic strain rates from Landsat 8-derived velocity grids. *Journal of Glaciology*, 64(244):321–332.

Alley, R. B., Dupont, T. K., Parizek, B. R., and Anandakrishnan, S. (2005). Access of surface meltwater to beds of sub-freezing glaciers: preliminary insights. *Annals of Glaciology*, 40:8–14.

Alshehhi, R., Marpu, P. R., Woon, W. L., and Dalla Mura, M. (2017). Simultaneous extraction of roads and buildings in remote sensing imagery with convolutional neural networks. *ISPRS Journal of Photogrammetry and Remote Sensing*, 130:139–149.

Andrews, L. C., Catania, G. A., Hoffman, M. J., Gulley, J. D., Lüthi, M. P., Ryser, C., Hawley, R. L., and Neumann, T. A. (2014). Direct observations of evolving subglacial drainage beneath the Greenland Ice Sheet. *Nature*, 514(7520):80–83.

Andrews, L. C., Hoffman, M. J., Neumann, T. A., Catania, G. A., Lüthi, M. P., Hawley, R. L., Schild, K. M., Ryser, C., and Morriss, B. F. (2018). Seasonal evolution of the subglacial hydrologic system modified by supraglacial lake drainage in Western Greenland. *Journal of Geophysical Research: Earth Surface*, 123(6):1479–1496.

Arnold, N. S., Banwell, A. F., and Willis, I. C. (2014). High-resolution modelling of the seasonal evolution of surface water storage on the Greenland Ice Sheet. *The Cryosphere*, 8(4):1149–1160.

Azzoni, R. S., Fugazza, D., Zerboni, A., Senese, A., D'Agata, C., Maragno, D., Carzaniga, A., Cernuschi, M., and Diolaiuti, G. A. (2018). Evaluating high-resolution remote sensing data for reconstructing the recent evolution of supra glacial debris: A study in the Central Alps (Stelvio Park, Italy). *Progress in Physical Geography: Earth and Environment*, 42(1):3–23.

Bamber, J. L., Westaway, R. M., Marzeion, B., and Wouters, B. (2018). The land ice contribution to sea level during the satellite era. *Environmental Research Letters*, 13(6):063008.

Banwell, A., Hewitt, I., Willis, I., and Arnold, N. (2016). Moulin density controls drainage development beneath the Greenland ice sheet. *Journal of Geophysical Research: Earth Surface*, 121(12):2248–2269.

Banwell, A. F., Willis, I. C., and Arnold, N. S. (2013). Modeling subglacial water routing at Paakitsoq, W Greenland. *Journal of Geophysical Research: Earth Surface*, 118(3):1282–1295.

Bartholomew, I., Nienow, P., Mair, D., Hubbard, A., King, M. A., and Sole, A. (2010). Seasonal evolution of subglacial drainage and acceleration in a Greenland outlet glacier. *Nature Geoscience*, 3(6):408.

Bartholomew, I., Nienow, P., Sole, A., Mair, D., Cowton, T., and King, M. A. (2012). Short-term variability in Greenland Ice Sheet motion forced by time-varying meltwater drainage: Implications for the relationship between subglacial drainage system behavior and ice velocity. *Journal of Geophysical Research: Earth Surface*, 117(F3).

Bash, E. A. and Moorman, B. J. (2020). Surface melt and the importance of water flow–an analysis based on high-resolution unmanned aerial vehicle (UAV) data for an Arctic glacier. *The Cryosphere*, 14(2):549–563.

Benassi, F., Dall'Asta, E., Diotri, F., Forlani, G., Morra di Cella, U., Roncella, R., and Santise, M. (2017). Testing Accuracy and Repeatability of UAV Blocks Oriented with GNSS-Supported Aerial Triangulation. *Remote Sensing*, 9(2):172.

Benn, D. I., Åström, J., Zwinger, T., Todd, J., Nick, F. M., Cook, S., Hulton, N. R., and Luckman, A. (2017). Melt-under-cutting and buoyancy-driven calving from tidewater glaciers: New insights from discrete element and continuum model simulations. *Journal of Glaciology*, 63(240):691–702.

Bevan, S. L., Luckman, A., Khan, S. A., and Murray, T. (2015). Seasonal dynamic thinning at Helheim Glacier. *Earth and Planetary Science Letters*, 415:47–53.

Bevis, M., Harig, C., Khan, S. A., Brown, A., Simons, F. J., Willis, M., Fettweis, X., Van Den Broeke, M. R., Madsen, F. B., Kendrick, E., et al. (2019). Accelerating changes in ice mass within Greenland, and the ice sheet's sensitivity to atmospheric forcing. *Proceedings of the National Academy of Sciences*, 116(6):1934–1939.

Bhardwaj, A., Sam, L., Akanksha, Martín-Torres, F. J., and Kumar, R. (2016). UAVs as remote sensing platform in glaciology: Present applications and future prospects. *Remote Sensing of Environment*, 175:196–204.

Bindschadler, R., Vornberger, P., Blankenship, D., Scambos, T., and Jacobel, R. (1996). Surface velocity and mass balance of Ice Streams D and E, West Antarctica. *Journal of Glaciology*, 42(142):461–475.

Blankenberg, L. E. (1992). GPS-supported aerial triangulation - state of the art. *The Photogrammetric Journal of Finland*, 13(1):4–16.

Blaschke, T. (2010). Object based image analysis for remote sensing. *ISPRS Journal of Photogrammetry and Remote Sensing*, 65(1):2–16.

Bondzio, J. H., Morlighem, M., Seroussi, H., Kleiner, T., Rückamp, M., Mouginot, J., Moon, T., Larour, E. Y., and Humbert, A. (2017). The mechanisms behind Jakobshavn Isbræ's acceleration and mass loss: A 3-D thermomechanical model study. *Geophysical Research Letters*, 44(12):6252–6260.

Boon, S. and Sharp, M. (2003). The role of hydrologically-driven ice fracture in drainage system evolution on an Arctic glacier. *Geophysical Research Letters*, 30(18).

Bougamont, M., Christoffersen, P., A L, H., Fitzpatrick, A., Doyle, S. H., and Carter, S. P. (2014). Sensitive response of the Greenland Ice Sheet to surface melt drainage over a soft bed. *Nature Communications*, 5:5052.

Box, J. E. (2013). Greenland ice sheet mass balance reconstruction. Part II: Surface mass balance (1840–2010). *Journal of Climate*, 26(18):6974–6989.

Brecher, H. (1986). Surface velocity determination on large polar glaciers by aerial photogrammetry. *Annals of Glaciology*, 8:22–26.

Brun, F., Buri, P., Miles, E. S., Wagnon, P., Steiner, J., Berthier, E., Ragettli, S., Kraaijenbrink, P., Immerzeel, W. W., and Pellicciotti, F. (2016). Quantifying volume loss from ice cliffs on debris-covered glaciers using high-resolution terrestrial and aerial photogrammetry. *Journal of Glaciology*, pages 1–12.

Burkhart, J. F., Kylling, A., Schaaf, C. B., Wang, Z., Bogren, W., Storvold, R., Solbø, S., Pedersen, C. A., and Gerland, S. (2017). Unmanned aerial system nadir reflectance and MODIS nadir BRDF-adjusted surface reflectances intercompared over Greenland. *The Cryosphere*, 11(4):1575–1589.

Carmichael, J. D., Joughin, I., Behn, M. D., Das, S., King, M. A., Stevens, L., and Lizarralde, D. (2015). Seismicity on the western Greenland Ice Sheet: Surface fracture in the vicinity of active moulins. *Journal of Geophysical Research: Earth Surface*, 120(6):1082–1106.

Carrivick, J. L., Smith, M. W., and Quincey, D. J. (2016). *Structure from Motion in the Geosciences*. John Wiley & Sons.

Catania, G. and Neumann, T. (2010). Persistent englacial drainage features in the Greenland Ice Sheet. *Geophysical Research Letters*, 37(2).

Catania, G. A., Stearns, L. A., Moon, T. A., Enderlin, E. M., and Jackson, R. H. (2020). Future Evolution of Greenland's Marine-Terminating Outlet Glaciers. *Journal of Geophysical Research: Earth Surface*, 125(2):e2018JF004873. e2018JF004873 10.1029/2018JF004873.

Cavanagh, J., Lampkin, D., and Moon, T. (2017). Seasonal variability in regional ice flow due to meltwater injection into the shear margins of Jakobshavn Isbræ. *Journal of Geophysical Research: Earth Surface*, 122(12):2488–2505.

Chandler, D., Wadham, J., Lis, G., Cowton, T., Sole, A., Bartholomew, I., Telling, J., Nienow, P., Bagshaw, E., Mair, D., et al. (2013). Evolution of the subglacial drainage system beneath the Greenland Ice Sheet revealed by tracers. *Nature Geoscience*, 6(3):195–198.

Chauche, N., Hubbard, A., Gascard, J.-C., Box, J., Bates, R., Koppes, M., Sole, A., Christoffersen, P., and Patton, H. (2014). Ice–ocean interaction and calving front morphology at two west Greenland tidewater outlet glaciers. *The Cryosphere*, 8(4):1457–1468.

Chen, G. (1998). *GPS kinematic positioning for the airborne laser altimetry at Long Valley, California*. PhD thesis, Massachusetts Institute of Technology.

Chen, X., Zhang, X., Church, J. A., Watson, C. S., King, M. A., Monselesan, D., Legresy, B., and Harig, C. (2017). The increasing rate of global mean sea-level rise during 1993–2014. *Nature Climate Change*, 7(7):492–495.

Christoffersen, P., Bougamont, M., Hubbard, A., Doyle, S. H., Grigsby, S., and Pettersson, R. (2018). Cascading lake drainage on the Greenland Ice Sheet triggered by tensile shock and fracture. *Nature communications*, 9(1):1064.

Chu, V. W. (2014). Greenland ice sheet hydrology: A review. *Progress in Physical Geography*, 38(1):19–54.

Chu, W., Schroeder, D. M., Seroussi, H., Creyts, T. T., Palmer, S. J., and Bell, R. E. (2016). Extensive winter subglacial water storage beneath the Greenland Ice Sheet. *Geophysical Research Letters*, 43(24):12,484–12,492.

Chudley, T. R., Christoffersen, P., Doyle, S. H., Abellan, A., and Snooke, N. (2019a). High-accuracy UAV photogrammetry of ice sheet dynamics with no ground control. *The Cryosphere*, 13(3):955–968.

Chudley, T. R., Christoffersen, P., Doyle, S. H., Bougamont, M., Schoonman, C. M., Hubbard, B., and James, M. R. (2019b). Supraglacial lake drainage at a fast-flowing greenlandic outlet glacier. *Proceedings of the National Academy of Sciences*, 116(51):25468–25477.

Church, J., Clark, P., Cazenave, A., Gregory, J., Jevrejeva, S., Levermann, A., Merrifield, M., Milne, G., Nerem, R., Nunn, P., Payne, A., Pfeffer, W., Stammer, D., and Unnikrishnan, A. (2013). Sea Level Change. In Stocker, T., Qin, D., Plattner, G.-K., Tignor, M., Allen, S., Boschung, J., Nauels, A., Xia, Y., Bex, V., and Midgley, P., editors, *Climate Change 2013: The Physical Science Basis. Contribution of Working Group I to the Fifth Assessment Report of the Intergovernmental Panel on Climate Change*, book section 4, pages 317—-382. Cambridge University Press, Cambridge, United Kingdom and New York, NY, USA.

Clason, C. C., Mair, D., Nienow, P., Bartholomew, I., Sole, A., Palmer, S., and Schwanghart, W. (2015). Modelling the transfer of supraglacial meltwater to the bed of Leverett Glacier, Southwest Greenland. *The Cryosphere*, 9(1):123–138.

Colgan, W., Rajaram, H., Abdalati, W., McCutchan, C., Mottram, R., Moussavi, M. S., and Grigsby, S. (2016). Glacier crevasses: Observations, models, and mass balance implications. *Reviews of Geophysics*, 54(1):119–161.

Colgan, W., Steffen, K., McLamb, W. S., Abdalati, W., Rajaram, H., Motyka, R., Phillips, T., and Anderson, R. (2011). An increase in crevasse extent, West Greenland: Hydrologic implications. *Geophysical Research Letters*, 38(18).

Cook, J. M., Tedstone, A. J., Williamson, C., McCutcheon, J., Hodson, A. J., Dayal, A., Skiles, M., Hofer, S., Bryant, R., McAree, O., McGonigle, A., Ryan, J., Anesio, A. M., Irvine-Fynn, T. D. L., Hubbard, A., Hanna, E., Flanner, M., Mayanna, S., Benning, L. G., van As, D., Yallop, M., McQuaid, J. B., Gribbin, T., and Tranter, M. (2020). Glacier algae accelerate melt rates on the south-western Greenland Ice Sheet. *The Cryosphere*, 14(1):309–330.

Cooley, S. W. and Christoffersen, P. (2017). Observation bias correction reveals more rapidly draining lakes on the Greenland Ice Sheet. *Journal of Geophysical Research: Earth Surface*, 122(10):1867–1881.

Cooper, M. G., Smith, L. C., Rennermalm, A. K., Miège, C., Pitcher, L. H., Ryan, J. C., Kang, Y., and Cooley, S. W. (2018). Meltwater storage in low-density near-surface bare ice in the Greenland ice sheet ablation zone. *The Cryosphere*, 12(3):955.

Copernicus Climate Change Service (2017). ERA5: Fifth generation of ECMWF atmospheric reanalyses of the global climate. Copernicus Climate Change Service Climate Data Store (CDS). https://cds.climate.copernicus.eu/cdsapp#!/home.

Cowton, T., Nienow, P., Sole, A., Bartholomew, I., and Mair, D. (2016). Variability in ice motion at a land-terminating Greenlandic outlet glacier: the role of channelized and distributed drainage systems. *Journal of Glaciology*, 62(233):451–466.

Cowton, T., Nienow, P., Sole, A., Wadham, J., Lis, G., Bartholomew, I., Mair, D., and Chandler, D. (2013). Evolution of drainage system morphology at a land-terminating Greenlandic outlet glacier. *Journal of Geophysical Research: Earth Surface*, 118(1):29–41.

Cowton, T., Slater, D., Sole, A., Goldberg, D., and Nienow, P. (2015). Modeling the impact of glacial runoff on fjord circulation and submarine melt rate using a new subgrid-scale parameterization for glacial plumes. *Journal of Geophysical Research: Oceans*, 120(2):796–812.

Csatho, B. M., Schenk, A. F., van der Veen, C. J., Babonis, G., Duncan, K., Rezvanbehbahani, S., Van Den Broeke, M. R., Simonsen, S. B., Nagarajan, S., and van Angelen, J. H. (2014). Laser altimetry reveals complex pattern of Greenland Ice Sheet dynamics. *Proceedings of the National Academy of Sciences*, 111(52):18478–18483.

Cucci, D. A., Rehak, M., and Skaloud, J. (2017). Bundle adjustment with raw inertial observations in UAV applications. *ISPRS Journal of Photogrammetry and Remote Sensing*, 130:1–12.

Cuffey, K. M. and Paterson, W. S. B. (2010). *The physics of glaciers*. Academic Press.

Das, S. B., Joughin, I., Behn, M. D., Howat, I. M., King, M. A., Lizarralde, D., and Bhatia, M. P. (2008). Fracture propagation to the base of the Greenland Ice Sheet during supraglacial lake drainage. *Science*, 320(5877):778–781.

Davison, B. J., Sole, A. J., Livingstone, S. J., Cowton, T. R., and Nienow, P. W. (2019). The influence of hydrology on the dynamics of land-terminating sectors of the Greenland Ice Sheet. *Frontiers in Earth Science*, 7.

Dell, R., Carr, R., Phillips, E., and Russel, A. J. (2019). Response of glacier flow and structure to proglacial lake development and climate at Fjallsjökull, south-east Iceland. *Journal of Glaciology*, page 1–16.

Dietrich, J. T. (2017). Bathymetric structure-from-motion: extracting shallow stream bathymetry from multi-view stereo photogrammetry. *Earth Surface Processes and Landforms*, 42(2):355–364.

Ding, P., Zhang, Y., Deng, W.-J., Jia, P., and Kuijper, A. (2018). A light and faster regional convolutional neural network for object detection in optical remote sensing images. *ISPRS Journal of Photogrammetry and Remote Sensing*, 141:208–218.

Doake, C., Corr, H., Rott, H., Skvarca, P., and Young, N. (1998). Breakup and conditions for stability of the northern Larsen Ice Shelf, antarctica. *Nature*, 391(6669):778–780.

Dow, C. F., Kulessa, B., Rutt, I. C., Tsai, V. C., Pimentel, S., Doyle, S. H., van As, D., Lindbäck, K., Pettersson, R., Jones, G. A., and Hubbard, A. (2015). Modeling of subglacial hydrological development following rapid supraglacial lake drainage. *Journal of Geophysical Research: Earth Surface*, 120(6):2014JF003333.

Dow, J. M., Neilan, R. E., and Rizos, C. (2009). The international GNSS service in a changing landscape of global navigation satellite systems. *Journal of Geodesy*, 83(3-4):191–198.

Doyle, S. H. (2014). *GPS-based investigations of Greenland Ice Sheet dynamics*. PhD thesis, Aberystwyth University.

Doyle, S. H., Hubbard, A., Dow, C. F., Jones, G. A., Fitzpatrick, A., Gusmeroli, A., Kulessa, B., Lindback, K., Pettersson, R., and Box, J. E. (2013). Ice tectonic deformation during the rapid in situ drainage of a supraglacial lake on the Greenland Ice Sheet. *The Cryosphere*, 7(1):129–140.

Doyle, S. H., Hubbard, A., Fitzpatrick, A. A., Van As, D., Mikkelsen, A. B., Pettersson, R., and Hubbard, B. (2014). Persistent flow acceleration within the interior of the Greenland ice sheet. *Geophysical Research Letters*, 41(3):899–905.

Doyle, S. H., Hubbard, A., van de Wal, R. S. W., Box, J. E., van As, D., Scharrer, K., Meierbachtol, T. W., Smeets, P. C. J. P., Harper, J. T., Johansson, E., Mottram, R. H., Mikkelsen, A. B., Wilhelms, F., Patton, H., Christoffersen, P., and Hubbard, B. (2015). Amplified melt and flow of the Greenland ice sheet driven by late-summer cyclonic rainfall. *Nature Geoscience*, 8(8):647–653.

Doyle, S. H., Hubbard, B., Christoffersen, P., Young, T. J., Hofstede, C., Bougamont, M., Box, J. E., and Hubbard, A. (2018). Physical Conditions of Fast Glacier Flow: 1. Measurements From Boreholes Drilled to the Bed of Store Glacier, West Greenland. *Journal of Geophysical Research: Earth Surface*, 123(2):324–348.

Dąbski, M., Zmarz, A., Pabjanek, P., Korczak-Abshire, M., Karsznia, I., and Chwedorzewska, K. (2017). UAV-based detection and spatial analyses of periglacial landforms on Demay Point (King George Island, South Shetland Islands, Antarctica). *Geomorphology*, 290:29–38.

Echelmeyer, K., Clarke, T., and Harrison, W. (1991). Surficial glaciology of Jakobshavns Isbræ, West Greenland: Part I. Surface morphology. *Journal of Glaciology*, 37(127):368–382.

Eltner, A., Kaiser, A., Castillo, C., Rock, G., Neugirg, F., and Abellán, A. (2016). Image-based surface reconstruction in geomorphometry–merits, limits and developments. *Earth Surface Dynamics*, 4(2):359–389.

Ely, J. C., Graham, C., Barr, I. D., Rea, B. R., Spagnolo, M., and Evans, J. (2016). Using UAV acquired photography and structure from motion techniques for studying glacier landforms: application to the glacial flutes at Isfallsglaciären. *Earth Surface Processes and Landforms*, 42(6):877–888.

Enderlin, E. M., Howat, I. M., Jeong, S., Noh, M.-J., van Angelen, J. H., and van den Broeke, M. R. (2014). An improved mass budget for the Greenland ice sheet. *Geophysical Research Letters*, 41(3):866–872.

Everett, A., Murray, T., Selmes, N., Rutt, I., Luckman, A., James, T., Clason, C., O'Leary, M., Karunarathna, H., Moloney, V., et al. (2016). Annual down-glacier drainage of lakes and water-filled crevasses at Helheim Glacier, southeast Greenland. *Journal of Geophysical Research: Earth Surface*, 121(10):1819–1833.

Fahnestock, M., Scambos, T., Moon, T., Gardner, A., Haran, T., and Klinger, M. (2016). Rapid large-area mapping of ice flow using Landsat 8. *Remote Sensing of Environment*, 185:84–94.

Fazeli, H., Samadzadegan, F., and Dadrasjavan, F. (2016). Evaluating the potential of RTK-UAV for automatic point cloud generation in 3D rapid mapping. *The International Archives of Photogrammetry, Remote Sensing and Spatial Information Sciences*, 41:221.

Felikson, D., Bartholomaus, T. C., Catania, G. A., Korsgaard, N. J., Kjær, K. H., Morlighem, M., Noël, B., Van Den Broeke, M., Stearns, L. A., Shroyer, E. L., Sutherland, D. A., and Nash, J. D. (2017). Inland thinning on the Greenland ice sheet controlled by outlet glacier geometry. *Nature Geoscience*, 10(5):366–369.

Fettweis, X., Box, J., Agosta, C., Amory, C., Kittel, C., Lang, C., van As, D., Machguth, H., and Gallée, H. (2017). Reconstructions of the 1900–2015 Greenland ice sheet surface mass balance using the regional climate MAR model. *The Cryosphere*, 11:1015–1033.

Finsterwalder, R. (1954). Photogrammetry and glacier research with special reference to glacier retreat in the eastern Alps. *Journal of Glaciology*, 2(15):306–315.

Fitzpatrick, A. A. W., Hubbard, A. L., Box, J., Quincey, D. J., Van As, D., Mikkelsen, A., Doyle, S. H., Dow, C., Hasholt, B., and Jones, G. A. (2014). A decade (2002–2012) of supraglacial lake volume estimates across Russell Glacier, West Greenland. *Cryosphere*, 8(1):107–121.

Florinsky, I. and Bliakharskii, D. (2019). Detection of crevasses by geomorphometric treatment of data from unmanned aerial surveys. *Remote Sensing Letters*, 10(4):323–332.

Flowers, G. E. (2018). Hydrology and the future of the Greenland Ice Sheet. *Nature communications*, 9(1):1–4.

Flowers, G. E., Jarosch, A. H., Belliveau, P. T., and Fuhrman, L. A. (2016). Short-term velocity variations and sliding sensitivity of a slowly surging glacier. *Annals of Glaciology*, 57(72):71–83.

Fonstad, M. A., Dietrich, J. T., Courville, B. C., Jensen, J. L., and Carbonneau, P. E. (2013). Topographic structure from motion: a new development in photogrammetric measurement. *Earth Surface Processes and Landforms*, 38(4):421–430.

Forster, R. R., Box, J. E., Van Den Broeke, M. R., Miège, C., Burgess, E. W., Van Angelen, J. H., Lenaerts, J. T., Koenig, L. S., Paden, J., Lewis, C., et al. (2014). Extensive liquid meltwater storage in firn within the Greenland ice sheet. *Nature Geoscience*, 7(2):95–98.

Fountain, A. G., Jacobel, R. W., Schlichting, R., and Jansson, P. (2005). Fractures as the main pathways of water flow in temperate glaciers. *Nature*, 433(7026):618–621.

Fountain, A. G. and Walder, J. S. (1998). Water flow through temperate glaciers. *Reviews of Geophysics*, 36(3):299–328.

Freeman, T. G. (1991). Calculating catchment area with divergent flow based on a regular grid. *Computers & Geosciences*, 17(3):413–422.

Fried, M., Catania, G., Stearns, L., Sutherland, D., Bartholomaus, T., Shroyer, E., and Nash, J. (2018). Reconciling drivers of seasonal terminus advance and retreat at 13 Central West Greenland tidewater glaciers. *Journal of Geophysical Research: Earth Surface*, 123(7):1590–1607.

Fryer, J. (1983). Photogrammetry through shallow water. *Australian Journal of Geodesy, Photogrammetry and Surveying*, 38:25–38.

Fryer, J. and Kniest, H. (1985). Errors in depth determination caused by waves in through-water photogrammetry. *The Photogrammetric Record*, 11(66):745–753.

Funk, M., Echelmeyer, K., and Iken, A. (1994). Mechanisms of fast flow in Jakobshavns Isbræ, West Greenland: Part II. modeling of englacial temperatures. *Journal of Glaciology*, 40(136):569–585.

Furukawa, Y. and Hernández, C. (2015). Multi-view stereo: A tutorial. *Foundations and Trends in Computer Graphics and Vision*, 9(1-2):1–148.

Furukawa, Y. and Ponce, J. (2010). Accurate, dense, and robust multiview stereopsis. *IEEE transactions on pattern analysis and machine intelligence*, 32(8):1362–1376.

Gardner, A. S., Fahnestock, M. A., and Scambos, T. A. (2019). ITS_LIVE: Regional Glacier and Ice Sheet Surface Velocities. National Snow and Ice Data Center.

Gindraux, S., Boesch, R., and Farinotti, D. (2017). Accuracy Assessment of Digital Surface Models from Unmanned Aerial Vehicles' Imagery on Glaciers. *Remote Sensing*, 9(2):186.

Gledhill, L. A. and Williamson, A. G. (2018). Inland advance of supraglacial lakes in north-west Greenland under recent climatic warming. *Annals of Glaciology*, 59(76pt1):66–82.

Gorelick, N., Hancher, M., Dixon, M., Ilyushchenko, S., Thau, D., and Moore, R. (2017). Google Earth Engine: Planetary-scale geospatial analysis for everyone. *Remote Sensing of Environment*, 202:18 – 27.

Gudmundsson, G., Bassi, A., Vonmoos, M., Bauder, A., Fischer, U., and Funk, M. (2000). High-resolution measurements of spatial and temporal variations in surface velocities of Unteraargletscher, Bernese Alps, Switzerland. *Annals of Glaciology*, 31:63–68.

Hagen, J. O., Eiken, T., Kohler, J., and Melvold, K. (2005). Geometry changes on Svalbard glaciers: mass-balance or dynamic response? *Annals of Glaciology*, 42:255–261.

Hambrey, M. J. and Müller, F. (1978). Structures and ice deformation in the white glacier, Axel Heiberg Island, Northwest Territories, Canada. *Journal of Glaciology*, 20(82):41–66.

Hanna, E., Cropper, T. E., Hall, R. J., and Cappelen, J. (2016). Greenland Blocking Index 1851–2015: a regional climate change signal. *International Journal of Climatology*, 36(15):4847–4861.

Hanna, E., Fettweis, X., Mernild, S. H., Cappelen, J., Ribergaard, M. H., Shuman, C. A., Steffen, K., Wood, L., and Mote, T. L. (2014). Atmospheric and oceanic climate forcing of the exceptional Greenland ice sheet surface melt in summer 2012. *International Journal of Climatology*, 34(4):1022–1037.

Harper, J. T., Humphrey, N. F., and Pfeffer, W. T. (1998). Crevasse patterns and the strain-rate tensor: A high-resolution comparison. *Journal of Glaciology*, 44(146):68–76.

Harper, J. T., Humphrey, N. F., Pfeffer, W. T., and Lazar, B. (2007). Two modes of accelerated glacier sliding related to water. *Geophysical Research Letters*, 34(12).

Harrington, J. A., Humphrey, N. F., and Harper, J. T. (2015). Temperature distribution and thermal anomalies along a flowline of the Greenland ice sheet. *Annals of Glaciology*, 56(70):98–104.

Harris, W. and Umbach, M. (1972). Underwater mapping. *Photogrammetric Engineering*, 38:1037–1042.

Hinze, H. and Seeber, G. (1988). Ice-motion determination by means of satellite positioning systems. *Annals of Glaciology*, 11:36–41.

Hoffman, M., Catania, G., Neumann, T., Andrews, L., and Rumrill, J. (2011). Links between acceleration, melting, and supraglacial lake drainage of the western Greenland Ice Sheet. *Journal of Geophysical Research: Earth Surface*, 116(F4).

Hoffman, M. J., Perego, M., Andrews, L. C., Price, S. F., Neumann, T. A., Johnson, J. V., Catania, G., and Lüthi, M. P. (2018). Widespread moulin formation during supraglacial lake drainages in Greenland. *Geophysical Research Letters*, 45(2):778–788.

Hofstede, C., Christoffersen, P., Hubbard, B., Doyle, S. H., Young, T. J., Diez, A., Eisen, O., and Hubbard, A. (2018). Physical conditions of fast glacier flow: 2. variable extent of anisotropic ice and soft basal sediment from seismic reflection data acquired on Store Glacier, West Greenland. *Journal of Geophysical Research: Earth Surface*, 123(2):349–362.

Holmlund, E. S. and Holmlund, P. (2019). Constraining 135 years of mass balance with historic structure-from-motion photogrammetry on Storglaciären, sweden. *Geografiska Annaler: Series A, Physical Geography*, 101(3):195–210.

Howat, I., De la Pena, S., Van Angelen, J., Lenaerts, J., and Van den Broeke, M. (2013). Brief Communication Expansion of meltwater lakes on the Greenland ice sheet. *The Cryosphere*, 7:201–204.

Howat, I. M., Box, J. E., Ahn, Y., Herrington, A., and McFadden, E. M. (2010). Seasonal variability in the dynamics of marine-terminating outlet glaciers in Greenland. *Journal of Glaciology*, 56(198):601–613.

Howat, I. M., Negrete, A., and Smith, B. E. (2014). The Greenland Ice Mapping Project (GIMP) land classification and surface elevation data sets. *The Cryosphere*, 8(4):1509–1518.

Hubbard, B. and Nienow, P. (1997). Alpine subglacial hydrology. *Quaternary Science Reviews*, 16(9):939–955.

Hugenholtz, C., Brown, O., Walker, J., Barchyn, T., Nesbit, P., Kucharczyk, M., and Myshak, S. (2016). Spatial Accuracy of UAV-Derived Orthoimagery and Topography: Comparing Photogrammetric Models Processed with Direct Geo-Referencing and Ground Control Points. *GEOMATICA*, 70(1):21–30.

Ignéczi, Á., Sole, A. J., Livingstone, S. J., Leeson, A. A., Fettweis, X., Selmes, N., Gourmelen, N., and Briggs, K. (2016). Northeast sector of the Greenland Ice Sheet to undergo the greatest inland expansion of supraglacial lakes during the 21st century. *Geophysical Research Letters*, 43(18):9729–9738.

Iken, A., Echelmeyer, K., Harrison, W., and Funk, M. (1993). Mechanisms of fast flow in Jakobshavns Isbræ, West Greenland: Part I. Measurements of temperature and water level in deep boreholes. *Journal of Glaciology*, 39(131):15–25.

IMBIE Team (2018). Mass balance of the Antarctic Ice Sheet from 1992 to 2017. *Nature*, 558:219–222.

Immerzeel, W. W., Kraaijenbrink, P. D. A., Shea, J. M., Shrestha, A. B., Pellicciotti, F., Bierkens, M. F. P., and de Jong, S. M. (2014). High-resolution monitoring of Himalayan glacier dynamics using unmanned aerial vehicles. *Remote Sensing of Environment*, 150:93–103.

Irvine-Fynn, T. D., Hodson, A. J., Moorman, B. J., Vatne, G., and Hubbard, A. L. (2011). Polythermal glacier hydrology: A review. *Reviews of Geophysics*, 49(4).

James, M. R. and Robson, S. (2014). Mitigating systematic error in topographic models derived from UAV and ground-based image networks. *Earth Surface Processes and Landforms*, 39(10):1413–1420.

James, M. R., Robson, S., and Smith, M. W. (2017). 3-D uncertainty-based topographic change detection with structure-from-motion photogrammetry: precision maps for ground control and directly georeferenced surveys. *Earth Surface Processes and Landforms*, 42(12):1769–1788.

Johnson, K., Nissen, E., Saripalli, S., Arrowsmith, J. R., McGarey, P., Scharer, K., Williams, P., and Blisniuk, K. (2014). Rapid mapping of ultrafine fault zone topography with structure from motion. *Geosphere*, 10(5):969–986.

Jones, C., Ryan, J., Holt, T., and Hubbard, A. (2018). Structural glaciology of Isunguata Sermia, West Greenland. *Journal of Maps*, 14(2):517–527.

Joughin, I., Das, S. B., Flowers, G. E., Behn, M. D., Alley, R. B., King, M. A., Smith, B. E., Bamber, J. L., van den Broeke, M. R., and van Angelen, J. H. (2013). Influence of ice-sheet geometry and supraglacial lakes on seasonal ice-flow variability. *The Cryosphere*, 7(4):1185–1192.

Joughin, I., Smith, B. E., and Howat, I. M. (2018). A complete map of Greenland ice velocity derived from satellite data collected over 20 years. *Journal of Glaciology*, 64(243):1–11.

Joughin, I., Smith, B. E., Howat, I. M., Scambos, T., and Moon, T. (2010). Greenland flow variability from ice-sheet-wide velocity mapping. *Journal of Glaciology*, 56(197):415–430.

Jouvet, G., van Dongen, E., Lüthi, M. P., and Vieli, A. (2020). In situ measurements of the ice flow motion at Eqip Sermia Glacier using a remotely controlled unmanned aerial vehicle (UAV). *Geoscientific Instrumentation, Methods and Data Systems*, 9(1):1–10.

Jouvet, G., Weidmann, Y., Kneib, M., Detert, M., Seguinot, J., Sakakibara, D., and Sugiyama, S. (2018). Short-lived ice speed-up and plume water flow captured

by a VTOL UAV give insights into subglacial hydrological system of Bowdoin Glacier. *Remote Sensing of Environment*, 217:389–399.

Jouvet, G., Weidmann, Y., Seguinot, J., Funk, M., Abe, T., Sakakibara, D., Seddik, H., and Sugiyama, S. (2017). Initiation of a major calving event on the Bowdoin Glacier captured by UAV photogrammetry. *The Cryosphere*, 11(2):911–921.

Jouvet, G., Weidmann, Y., van Dongen, E., Luethi, M., Vieli, A., and Ryan, J. (2019). High-endurance UAV for monitoring calving glaciers: Application to the Inglefield Bredning and Eqip Sermia, Greenland. *Frontiers in Earth Science*, 7:206.

Kääb, A., Haeberli, W., and Gudmundsson, G. H. (1997). Analysing the creep of mountain permafrost using high precision aerial photogrammetry: 25 years of monitoring Gruben rock glacier, Swiss Alps. *Permafrost and periglacial processes*, 8(4):409–426.

Kamb, B. (1987). Glacier surge mechanism based on linked cavity configuration of the basal water conduit system. *Journal of Geophysical Research: Solid Earth*, 92(B9):9083–9100.

Kick, W. (1966). Long-term glacier variations measured by photogrammetry. A re-survey of Tunsbergdalsbreen after 24 years. *Journal of Glaciology*, 6(43):3–18.

King, M. (2004). Rigorous GPS data-processing strategies for glaciological applications. *Journal of Glaciology*, 50(171):601–607.

King, M. D., Howat, I. M., Jeong, S., Noh, M. J., Wouters, B., Noël, B., and van den Broeke, M. R. (2018). Seasonal to decadal variability in ice discharge from the Greenland Ice Sheet. *The Cryosphere*, 12(12):3813.

Kingslake, J., Ng, F., and Sole, A. (2015). Modelling channelized surface drainage of supraglacial lakes. *Journal of Glaciology*, 61(225):185–199.

Kodde, M., Pfeifer, N., Gorte, B., Geist, T., and Höfle, B. (2007). Automatic glacier surface analysis from airborne laser scanning. *International Archives of the Photogrammetry, Remote Sensing and Spatial Information Sciences*, 36(3/W52):221–226.

Koenig, L. S., Lampkin, D. J., Montgomery, L. N., Hamilton, S. L., Turrin, J. B., Joseph, C. A., Moutsafa, S. E., Panzer, B., Casey, K. A., Paden, J. D., Leuschen, C., and Gogineni, P. (2015). Wintertime storage of water in buried supraglacial lakes across the Greenland Ice Sheet. *The Cryosphere*, 9(4):1333–1342.

Koenig, L. S., Miège, C., Forster, R. R., and Brucker, L. (2014). Initial in situ measurements of perennial meltwater storage in the Greenland firn aquifer. *Geophysical Research Letters*, 41(1):81–85.

Konecny, G. (1966). Applications of photogrammetry to surveys of glaciers in Canada and Alaska. *Canadian Journal of Earth Sciences*, 3(6):783–798.

Koziol, C., Arnold, N., Pope, A., and Colgan, W. (2017). Quantifying supraglacial meltwater pathways in the Paakitsoq region, west Greenland. *Journal of Glaciology*, 63(239):464–476.

Koziol, C. P. and Arnold, N. S. (2018). Modelling seasonal meltwater forcing of the velocity of the Greenland Ice Sheet. *The Cryosphere*, 12:971–991.

Kraaijenbrink, P., Meijer, S. W., Shea, J. M., Pellicciotti, F., Jong, S. M. D., and Immerzeel, W. W. (2016a). Seasonal surface velocities of a Himalayan glacier derived by automated correlation of unmanned aerial vehicle imagery. *Annals of Glaciology*, 57(71):103–113.

Kraaijenbrink, P. D. A., Shea, J. M., Litt, M., Steiner, J. F., Treichler, D., Koch, I., and Immerzeel, W. W. (2018). Mapping Surface Temperatures on a Debris-Covered Glacier with an Unmanned Aerial Vehicle. *Frontiers in Earth Science*, 6:64.

Kraaijenbrink, P. D. A., Shea, J. M., Pellicciotti, F., Jong, S. M. d., and Immerzeel, W. W. (2016b). Object-based analysis of unmanned aerial vehicle imagery to map and characterise surface features on a debris-covered glacier. *Remote Sensing of Environment*, 186:581–595.

Krawczynski, M. J., Behn, M. D., Das, S. B., and Joughin, I. (2009). Constraints on the lake volume required for hydro-fracture through ice sheets. *Geophysical Research Letters*, 36(10).

Lampkin, D., Amador, N., Parizek, B., Farness, K., and Jezek, K. (2013). Drainage from water-filled crevasses along the margins of Jakobshavn Isbræ: A potential catalyst for catchment expansion. *Journal of Geophysical Research: Earth Surface*, 118(2):795–813.

Lampkin, D. J., Parizek, B., Larour, E. Y., Seroussi, H., Joseph, C., and Cavanagh, J. P. (2018). Toward Improved Understanding of Changes in Greenland Outlet Glacier Shear Margin Dynamics in a Warming Climate. *Frontiers in Earth Science*, 6.

Law, R., Arnold, N., Benedek, C., Tedesco, M., Banwell, A., and Willis, I. (2020). Over-winter persistence of supraglacial lakes on the Greenland Ice Sheet: results and insights from a new model. *Journal of Glaciology*.

Lea, J. M. (2018). The Google Earth Engine Digitisation Tool (GEEDiT) and the Margin change Quantification tool (MaQiT)–simple tools for the rapid mapping and quantification of changing Earth surface margins. *Earth Surface Dynamics*, 6(3):551–561.

Leeson, A., Shepherd, A., Briggs, K., Howat, I., Fettweis, X., Morlighem, M., and Rignot, E. (2015). Supraglacial lakes on the Greenland ice sheet advance inland under warming climate. *Nature Climate Change*, 5(1):51–55.

Leick, A. (2004). GPS satellite surveying. *A Wiley–Interscience publication. United States of America*.

Lemos, A., Shepherd, A., McMillan, M., Hogg, A. E., Hatton, E., and Joughin, I. (2018). Ice velocity of Jakobshavn Isbræ, Petermann Glacier, Nioghalvfjerdsfjorden, and Zachariæ Isstrøm, 2015–2017, from Sentinel 1-a/b SAR imagery. *The Cryosphere*, 12(6):2087–2097.

Lindbäck, K., Pettersson, R., Hubbard, A. L., Doyle, S. H., van As, D., Mikkelsen, A. B., and Fitzpatrick, A. A. (2015). Subglacial water drainage, storage, and piracy beneath the Greenland ice sheet. *Geophysical Research Letters*, 42(18):7606–7614.

Liu, E. J., Wood, K., Mason, E., Edmonds, M., Aiuppa, A., Giudice, G., Bitetto, M., Francofonte, V., Burrow, S., Richardson, T., et al. (2019). Dynamics of outgassing and plume transport revealed by proximal Unmanned Aerial System (UAS) measurements at Volcán Villarrica, Chile. *Geochemistry, Geophysics, Geosystems*, 20(2):730–750.

Livingstone, S. J., Sole, A. J., Storrar, R. D., Harrison, D., Ross, N., and Bowling, J. (2019). Brief Communication: Outburst floods triggered by periodic drainage of subglacial lakes, Isunguata Sermia, West Greenland. *The Cryosphere*, 13(10):2789–2796.

Lowe, D. G. (2004). Distinctive image features from scale-invariant keypoints. *International Journal of Computer Vision*, 60(2):91–110.

Lüthi, M., Funk, M., Iken, A., Gogineni, S., and Truffer, M. (2002). Mechanisms of fast flow in Jakobshavn Isbrae, West Greenland, Part III: measurement of temperature and water level in deep boreholes. *Journal of Glaciology*, 46:369–385.

Lüthi, M. P., Ryser, C., Andrews, L. C., Catania, G. A., Funk, M., and Hawley, R. L. (2015). Heat sources within the Greenland Ice Sheet: dissipation, temperate paleo-firn and cryo-hydrologic warming. *The Cryosphere*.

Macdonald, G. J., Banwell, A. F., and MacAyeal, D. R. (2018). Seasonal evolution of supraglacial lakes on a floating ice tongue, Petermann Glacier, Greenland. *Annals of Glaciology*, 59(76pt1):56–65.

MacFerrin, M., Machguth, H., van As, D., Charalampidis, C., Stevens, C. M., Heilig, A., Vandecrux, B., Langen, P. L., Mottram, R., Fettweis, X., et al. (2019). Rapid expansion of Greenland's low-permeability ice slabs. *Nature*, 573(7774):403–407.

Machguth, H., MacFerrin, M., van As, D., Box, J. E., Charalampidis, C., Colgan, W., Fausto, R. S., Meijer, H. A., Mosley-Thompson, E., and van de Wal, R. S. (2016). Greenland meltwater storage in firn limited by near-surface ice formation. *Nature Climate Change*, 6(4):390–393.

Mair, D., Nienow, P., Willis, I., and Sharp, M. (2001). Spatial patterns of glacier motion during a high-velocity event: Haut Glacier d'Arolla, Switzerland. *Journal of Glaciology*, 47(156):9–20.

Mallalieu, J., Carrivick, J. L., Quincey, D. J., and Smith, M. W. (2020). Calving seasonality associated with melt-undercutting and lake ice cover. *Geophysical Research Letters*.

Mallalieu, J., Carrivick, J. L., Quincey, D. J., Smith, M. W., and James, W. H. (2017). An integrated Structure-from-Motion and time-lapse technique for quantifying ice-margin dynamics. *Journal of Glaciology*, 63(242):937–949.

Mankoff, K. D., Colgan, W., Solgaard, A., Karlsson, N. B., Ahlstrøm, A. P., van As, D., Box, J. E., Khan, S. A., Kjeldsen, K. K., Mouginot, J., and Fausto, R. S. (2019). Greenland Ice Sheet solid ice discharge from 1986 through 2017. *Earth System Science Data*, 11(2):769–786.

McGrath, D., Colgan, W., Steffen, K., Lauffenburger, P., and Balog, J. (2011). Assessing the summer water budget of a moulin basin in the Sermeq Avannarleq ablation region, Greenland ice sheet. *Journal of Glaciology*, 57(205):954–964.

Meierbachtol, T., Harper, J., and Humphrey, N. (2013). Basal Drainage System Response to Increasing Surface Melt on the Greenland Ice Sheet. *Science*, 341(6147):777–779.

Meierbachtol, T. W., Harper, J. T., Humphrey, N. F., and Wright, P. J. (2016). Mechanical forcing of water pressure in a hydraulically isolated reach beneath western greenland's ablation zone. *Annals of Glaciology*, 57(72):62–70.

Meredith, M., Sommerkorn, M., Cassotta, S., Derksen, C., Ekaykin, A., Hollowed, A., Kofinas, G., Mackintosh, A., Melbourne-Thomas, J., Muelbert, M., Ottersen, G., Pritchard, H., and Schuur, E. (2019). Polar Regions. In Pörtner, H.-O., Roberts, D., Masson-Delmotte, V., Zhai, P., Tignor, M., Poloczanska, E., Mintenbeck, K., Alegriía, A., Nicolai, M., Okem, A., Petzold, J., Rama, B., and Weyer, N., editors, *IPCC Special Report on the Ocean and Cryosphere in a Changing Climate*, book section 3.

Messerli, A. and Grinsted, A. (2015). Image georectification and feature tracking toolbox: ImGRAFT. *Geoscientific Instrumentation, Methods and Data Systems*, 4(1):23.

Mian, O., Lutes, J., Lipa, G., Hutton, J., Gavelle, E., and Borghini, S. (2015). Direct georeferencing on small unmanned aerial platforms for improved reliability and accuracy of mapping without the need for ground control points. *International Archives of the Photogrammetry, Remote Sensing and Spatial Information Sciences*, 40(1):397.

Midgley, N. G., Tonkin, T. N., Graham, D. J., and Cook, S. J. (2018). Evolution of high-Arctic glacial landforms during deglaciation. *Geomorphology*, 311:63–75.

Miles, K. E., Willis, I. C., Benedek, C. L., Williamson, A. G., and Tedesco, M. (2017). Toward monitoring surface and subsurface lakes on the Greenland ice sheet using Sentinel-1 SAR and Landsat-8 OLI imagery. *Frontiers in Earth Science*, 5:58.

Minchew, B., Simons, M., Riel, B., and Milillo, P. (2017). Tidally induced variations in vertical and horizontal motion on Rutford Ice Stream, West Antarctica, inferred from remotely sensed observations. *Journal of Geophysical Research: Earth Surface*, 122(1):167–190.

Mohajerani, Y., Wood, M., Velicogna, I., and Rignot, E. (2019). Detection of Glacier Calving Margins with Convolutional Neural Networks: A Case Study. *Remote Sensing*, 11(1):74.

Mölg, N. and Bolch, T. (2017). Structure-from-motion using historical aerial images to analyse changes in glacier surface elevation. *Remote Sensing*, 9(10):1021.

Moon, T., Joughin, I., Smith, B., and Howat, I. (2012). 21st-century evolution of Greenland outlet glacier velocities. *Science*, 336(6081):576–578.

Moon, T., Joughin, I., Smith, B., Van Den Broeke, M. R., Van De Berg, W. J., Noël, B., and Usher, M. (2014). Distinct patterns of seasonal Greenland glacier velocity. *Geophysical Research Letters*, 41(20):7209–7216.

Morlighem, M., Williams, C. N., Rignot, E., An, L., Arndt, J. E., Bamber, J. L., Catania, G., Chauché, N., Dowdeswell, J. A., Dorschel, B., et al. (2017). BedMachine v3: Complete bed topography and ocean bathymetry mapping of Greenland from multibeam echo sounding combined with mass conservation. *Geophysical Research Letters*, 44(21):11–051.

Morriss, B., Hawley, R., Chipman, J., Andrews, L., Catania, G., Hoffman, M., Lüthi, M., and Neumann, T. (2013). A ten-year record of supraglacial lake evolution and rapid drainage in West Greenland using an automated processing algorithm for multispectral imagery. *The Cryosphere*, 7(6):1869–1877.

Mottram, R. H. and Benn, D. I. (2009). Testing crevasse-depth models: A field study at Breiðamerkurjökull, Iceland. *Journal of Glaciology*, 55(192):746–752.

Mouginot, J., Rignot, E., Bjørk, A. A., van den Broeke, M., Millan, R., Morlighem, M., Noël, B., Scheuchl, B., and Wood, M. (2019a). Forty-six years of Greenland Ice Sheet mass balance from 1972 to 2018. *Proceedings of the National Academy of Sciences*, 116(19):9239–9244.

Mouginot, J., Rignot, E., and Scheuchl, B. (2019b). Continent-Wide, Interferometric SAR Phase, Mapping of Antarctic Ice Velocity. *Geophysical Research Letters*, 46(16):9710–9718.

Mulsow, C., Kenner, R., Bühler, Y., Stoffel, A., and Maas, H.-G. (2018). Subaquatic Digital Elevation Models from UAV-Imagery. *International Archives of the Photogrammetry, Remote Sensing & Spatial Information Sciences*, 42(2).

Nesbit, P. R. and Hugenholtz, C. H. (2019). Enhancing UAV–SfM 3d Model Accuracy in High-Relief Landscapes by Incorporating Oblique Images. *Remote Sensing*, 11(3):239.

Ng, Y. H. and Buchheim, J. (2018). WingtraOne PPK Assessment. White Paper, Wingtra.

Nghiem, S., Hall, D., Mote, T., Tedesco, M., Albert, M., Keegan, K., Shuman, C., DiGirolamo, N., and Neumann, G. (2012). The extreme melt across the Greenland ice sheet in 2012. *Geophysical Research Letters*, 39(20).

Nick, F. M., Vieli, A., Howat, I. M., and Joughin, I. (2009). Large-scale changes in Greenland outlet glacier dynamics triggered at the terminus. *Nature Geoscience*, 2(2):110–114.

Nienow, P., Sharp, M., and Willis, I. (1998). Seasonal changes in the morphology of the subglacial drainage system, Haut Glacier d'Arolla, Switzerland. *Earth Surface Processes and Landforms: The Journal of the British Geomorphological Group*, 23(9):825–843.

Nienow, P. W., Sole, A. J., Slater, D. A., and Cowton, T. R. (2017). Recent Advances in Our Understanding of the Role of Meltwater in the Greenland Ice Sheet System. *Current Climate Change Reports*, 3(4):330–344.

Noël, B., van De Berg, W., Lhermitte, S., Wouters, B., Machguth, H., Howat, I., Citterio, M., Moholdt, G., Lenaerts, J., and van den Broeke, M. R. (2017). A tipping point in refreezing accelerates mass loss of Greenland's glaciers and ice caps. *Nature Communications*, 8(1):1–8.

Noël, B., van de Berg, W. J., Wessem, V., Melchior, J., Van Meijgaard, E., Van As, D., Lenaerts, J., Lhermitte, S., Munneke, P. K., Smeets, C., et al. (2018). Modelling the climate and surface mass balance of polar ice sheets using RACMO2 – Part 1: Greenland (1958-2016). *Cryosphere*, 12(3):811–831.

Nye, J. (1976). Water flow in glaciers: jökulhlaups, tunnels and veins. *Journal of Glaciology*, 17(76):181–207.

Nye, J. F. (1957). The distribution of stress and velocity in glaciers and ice-sheets. *Proceedings of the Royal Society of London. Series A. Mathematical and Physical Sciences*, 239(1216):113–133.

Oppenheimer, M., Glavovic, B., Hinkel, J., van de Wal, R., Magnan, A., Abd-Elgawad, A., Cai, R., Cifuentes-Jara, M., DeConto, R., Ghosh, T., Hay, J., Isla,

F., Marzeion, B., Meyssignac, B., and Sebesvari, Z. (2019). Sea Level Rise and Implications for Low-Lying Islands, Coasts and Communities. In Pörtner, H.-O., Roberts, D., Masson-Delmotte, V., Zhai, P., Tignor, M., Poloczanska, E., Mintenbeck, K., Alegriía, A., Nicolai, M., Okem, A., Petzold, J., Rama, B., and Weyer, N., editors, *IPCC Special Report on the Ocean and Cryosphere in a Changing Climate*, book section 4.

Palmer, S., Shepherd, A., Nienow, P., and Joughin, I. (2011). Seasonal speedup of the Greenland Ice Sheet linked to routing of surface water. *Earth and Planetary Science Letters*, 302(3):423–428.

Parno, M. D., West, B. A., Song, A. J., Hodgdon, T. S., and O'Connor, D. (2019). Remote measurement of sea ice dynamics with regularized optimal transport. *Geophysical Research Letters*, 46(10):5341–5350.

Phillips, E., Finlayson, A., and Jones, L. (2013a). Fracturing, block faulting, and moulin development associated with progressive collapse and retreat of a maritime glacier: Falljökull, SE Iceland. *Journal of Geophysical Research: Earth Surface*, 118(3):1545–1561.

Phillips, T., Rajaram, H., Colgan, W., Steffen, K., and Abdalati, W. (2013b). Evaluation of cryo-hydrologic warming as an explanation for increased ice velocities in the wet snow zone, Sermeq Avannarleq, West Greenland. *Journal of Geophysical Research: Earth Surface*, 118(3):1241–1256.

Phillips, T., Rajaram, H., and Steffen, K. (2010). Cryo-hydrologic warming: A potential mechanism for rapid thermal response of ice sheets. *Geophysical Research Letters*, 37(20).

Poinar, K. (2015). *The Influence of Meltwater on the Thermal Structure and Flow of the Greenland Ice Sheet*. Thesis.

Poinar, K., Dow, C. F., and Andrews, L. C. (2019). Long-Term Support of an Active Subglacial Hydrologic System in Southeast Greenland by Firn Aquifers. *Geophysical Research Letters*, 46(9):4772–4781.

Poinar, K., Joughin, I., Das, S. B., Behn, M. D., Lenaerts, J. T., and Van Den Broeke, M. R. (2015). Limits to future expansion of surface-melt-enhanced ice flow into the interior of western Greenland. *Geophysical Research Letters*, 42(6):1800–1807.

Poinar, K., Joughin, I., Lenaerts, J. T., and Van Den Broeke, M. R. (2017a). Englacial latent-heat transfer has limited influence on seaward ice flux in western Greenland. *Journal of Glaciology*, 63(237):1–16.

Poinar, K., Joughin, I., Lilien, D., Brucker, L., Kehrl, L., and Nowicki, S. (2017b). Drainage of Southeast Greenland firn aquifer water through crevasses to the bed. *Frontiers in Earth Science*, 5:5.

Pope, A. (2016). Reproducibly estimating and evaluating supraglacial lake depth with Landsat 8 and other multispectral sensors. *Earth and Space Science*, 3(4):176–188.

Porter, C., Morin, P., Howat, I., Noh, M.-J., Bates, B., Peterman, K., Keesey, S., Schlenk, M., Gardiner, J., Tomko, K., Willis, M., Kelleher, C., Cloutier, M., Husby, E., Foga, S., Nakamura, H., Platson, M., Wethington, Michael, J., Williamson, C., Bauer, G., Enos, J., Arnold, G., Kramer, W., Becker, P., Doshi, A., D'Souza, C., Cummens, P., Laurier, F., and Bojesen, M. (2018). ArcticDEM. Harvard Dataverse.

Price, S. F., Payne, A. J., Howat, I. M., and Smith, B. E. (2011). Committed sea-level rise for the next century from Greenland ice sheet dynamics during the past decade. *Proceedings of the National Academy of Sciences*, 108(22):8978–8983.

Quincey, D. J., Glasser, N. F., Cook, S. J., and Luckman, A. (2015). Heterogeneity in Karakoram glacier surges. *Journal of Geophysical Research: Earth Surface*, 120(7):1288–1300.

Quinn, P., Beven, K., Chevallier, P., and Planchon, O. (1991). The prediction of hillslope flow paths for distributed hydrological modelling using digital terrain models. *Hydrological processes*, 5(1):59–79.

Ragettli, S., Pellicciotti, F., Immerzeel, W. W., Miles, E. S., Petersen, L., Heynen, M., Shea, J. M., Stumm, D., Joshi, S., and Shrestha, A. (2015). Unraveling the hydrology of a Himalayan catchment through integration of high resolution in situ data and remote sensing with an advanced simulation model. *Advances in Water Resources*, 78:94–111.

Rathmann, N., Hvidberg, C., Solgaard, A., Grinsted, A., Gudmundsson, G. H., Langen, P. L., Nielsen, K., and Kusk, A. (2017). Highly temporally resolved response to seasonal surface melt of the Zachariae and 79N outlet glaciers in northeast Greenland. *Geophysical Research Letters*, 44(19):9805–9814.

Rignot, E., Box, J., Burgess, E., and Hanna, E. (2008). Mass balance of the Greenland ice sheet from 1958 to 2007. *Geophysical Research Letters*, 35(20).

Rippin, D. M., Pomfret, A., and King, N. (2015). High resolution mapping of supraglacial drainage pathways reveals link between micro-channel drainage density, surface roughness and surface reflectance: UAVs, SfM and Supra-Glacial Drainage. *Earth Surface Processes and Landforms*, 40(10):1279–1290.

Rohner, C., Small, D., Beutel, J., Henke, D., Lüthi, M. P., and Vieli, A. (2019). Multisensor validation of tidewater glacier flow fields derived from synthetic aperture radar (SAR) intensity tracking. *The Cryosphere*, 13(11):2953–2975.

Röthlisberger, H. (1972). Water pressure in intra-and subglacial channels. *Journal of Glaciology*, 11(62):177–203.

Roze, A., Zufferey, J.-C., Beyeler, A., and McClellan, A. (2014). eBee RTK Accuracy Assessment. White Paper, SenseFly.

Ryan, J. C., Hubbard, A., Box, J. E., Brough, S., Cameron, K., Cook, J. M., Cooper, M., Doyle, S. H., Edwards, A., Holt, T., Irvine-Fynn, T., Jones, C., Pitcher, L. H., Rennermalm, A. K., Smith, L. C., Stibal, M., and Snooke, N. (2017). Derivation of High Spatial Resolution Albedo from UAV Digital Imagery: Application over the Greenland Ice Sheet. *Frontiers in Earth Science*, 5.

Ryan, J. C., Hubbard, A., Stibal, M., Irvine-Fynn, T. D., Cook, J., Smith, L. C., Cameron, K., and Box, J. (2018). Dark zone of the Greenland Ice Sheet controlled by distributed biologically-active impurities. *Nature Communications*, 9(1):1065.

Ryan, J. C., Hubbard, A. L., Box, J. E., Todd, J., Christoffersen, P., Carr, J. R., Holt, T. O., and Snooke, N. (2015). UAV photogrammetry and structure from motion to assess calving dynamics at Store Glacier, a large outlet draining the Greenland ice sheet. *The Cryosphere*, 9(1):1–11.

Sankey, T., Donager, J., McVay, J., and Sankey, J. B. (2017). UAV lidar and hyperspectral fusion for forest monitoring in the southwestern USA. *Remote Sensing of Environment*, 195:30–43.

Schoof, C. (2010). Ice-sheet acceleration driven by melt supply variability. *Nature*, 468(7325):803.

Schwalbe, E., Maas, H., Dietrich, R., and Ewert, H. (2008). Glacier velocity determination from multi temporal terrestrial long range laser scanner point clouds. *The International Archives of the Photogrammetry, Remote Sensensing and Spatial Information Sciences*, 37:457–462.

Schwalbe, E. and Maas, H.-G. (2017). The determination of high-resolution spatio-temporal glacier motion fields from time-lapse sequences. *Earth Surface Dynamics*, 5(4):861.

Seale, A., Christoffersen, P., Mugford, R. I., and O'Leary, M. (2011). Ocean forcing of the Greenland Ice Sheet: Clving fronts and patterns of retreat identified by automatic satellite monitoring of eastern outlet glaciers. *Journal of Geophysical Research: Earth Surface*, 116(F3).

Seier, G., Kellerer-Pirklbauer, A., Wecht, M., Hirschmann, S., Kaufmann, V., Lieb, G. K., and Sulzer, W. (2017). UAS-Based Change Detection of the Glacial and Proglacial Transition Zone at Pasterze Glacier, Austria. *Remote Sensing*, 9(6):549.

Seitz, S. M., Curless, B., Diebel, J., Scharstein, D., and Szeliski, R. (2006). A comparison and evaluation of multi-view stereo reconstruction algorithms. In *2006 IEEE computer society conference on computer vision and pattern recognition (CVPR'06)*, volume 1, pages 519–528. IEEE.

Selmes, N., Murray, T., and James, T. (2011). Fast draining lakes on the Greenland Ice Sheet. *Geophysical Research Letters*, 38(15).

Selmes, N., Murray, T., and James, T. (2013). Characterizing supraglacial lake drainage and freezing on the Greenland Ice Sheet. *The Cryosphere Discussions*, 7(1):475–505.

Shahbazi, M., Sohn, G., Théau, J., and Menard, P. (2015). Development and evaluation of a UAV-photogrammetry system for precise 3d environmental modeling. *Sensors*, 15(11):27493–27524.

Shapero, D. R., Joughin, I. R., Poinar, K., Morlighem, M., and Gillet-Chaulet, F. (2016). Basal resistance for three of the largest Greenland outlet glaciers. *Journal of Geophysical Research: Earth Surface*, 121(1):168–180.

Sharp, M., Richards, K., Willis, I., Arnold, N., Nienow, P., Lawson, W., and Tison, J.-L. (1993). Geometry, bed topography and drainage system structure of the Haut Glacier d'Arolla, Switzerland. *Earth Surface Processes and Landforms*, 18(6):557–571.

Shepherd, A., Ivins, E. R., Geruo, A., Barletta, V. R., Bentley, M. J., Bettadpur, S., Briggs, K. H., Bromwich, D. H., Forsberg, R., Galin, N., et al. (2012). A reconciled estimate of ice-sheet mass balance. *Science*, 338(6111):1183–1189.

Slater, D., Straneo, F., Das, S., Richards, C., Wagner, T., and Nienow, P. (2018). Localized plumes drive front-wide ocean melting of a Greenlandic tidewater glacier. *Geophysical Research Letters*, 45(22):12–350.

Slater, D. A., Goldberg, D. N., Nienow, P. W., and Cowton, T. R. (2016). Scalings for submarine melting at tidewater glaciers from buoyant plume theory. *Journal of Physical Oceanography*, 46(6):1839–1855.

Smith, L. C., Yang, K., Pitcher, L. H., Overstreet, B. T., Chu, V. W., Rennermalm, A. K., Ryan, J. C., Cooper, M. G., Gleason, C. J., Tedesco, M., Jeyaratnam, J., As, D. v., Broeke, M. R. v. d., Berg, W. J. v. d., Noël, B., Langen, P. L., Cullather, R. I., Zhao, B., Willis, M. J., Hubbard, A., Box, J. E., Jenner, B. A., and Behar, A. E. (2017). Direct measurements of meltwater runoff on the Greenland ice sheet surface. *Proceedings of the National Academy of Sciences*, 114(50):E10622–E10631.

Snavely, N., Seitz, S. M., and Szeliski, R. (2008). Modeling the world from internet photo collections. *International Journal of Computer Vision*, 80(2):189–210.

Sole, A., Nienow, P., Bartholomew, I., Mair, D., Cowton, T., Tedstone, A., and King, M. A. (2013). Winter motion mediates dynamic response of the Greenland Ice Sheet to warmer summers. *Geophysical Research Letters*, 40(15):3940–3944.

Sole, A. J., Mair, D. W. F., Nienow, P. W., Bartholomew, I., King, M., Burke, M. J., and Joughin, I. (2011). Seasonal speedup of a Greenland marine-terminating

outlet glacier forced by surface melt–induced changes in subglacial hydrology. *Journal of Geophysical Research: Earth Surface*, 116(F3).

Stevens, L. A., Behn, M. D., McGuire, J. J., Das, S. B., Joughin, I., Herring, T., Shean, D. E., and King, M. A. (2015). Greenland supraglacial lake drainages triggered by hydrologically induced basal slip. *Nature*, 522(7554):73.

Straneo, F., Hamilton, G. S., Sutherland, D. A., Stearns, L. A., Davidson, F., Hammill, M. O., Stenson, G. B., and Rosing-Asvid, A. (2010). Rapid circulation of warm subtropical waters in a major glacial fjord in East Greenland. *Nature Geoscience*, 3(3):182–186.

Strick, R. J., Ashworth, P. J., Sambrook Smith, G. H., Nicholas, A. P., Best, J. L., Lane, S. N., Parsons, D. R., Simpson, C. J., Unsworth, C. A., and Dale, J. (2018). Quantification of bedform dynamics and bedload sediment flux in sandy braided rivers from airborne and satellite imagery. *Earth Surface Processes and Landforms*, 44(4):953–972.

Stutz, J., Werner, B., Spolaor, M., Scalone, L., Festa, J., Tsai, C., Cheung, R., Colosimo, S. F., Tricoli, U., Raecke, R., et al. (2017). A new Differential Optical Absorption Spectroscopy instrument to study atmospheric chemistry from a high-altitude unmanned aircraft. *Atmospheric Measurement Techniques*, 10(3):1017–1042.

Sugiyama, S., Bauder, A., Huss, M., Riesen, P., and Funk, M. (2008). Triggering and drainage mechanisms of the 2004 glacier-dammed lake outburst in Gornergletscher, Switzerland. *Journal of Geophysical Research: Earth Surface*, 113(F4).

Sundal, A. V., Shepherd, A., Nienow, P., Hanna, E., Palmer, S., and Huybrechts, P. (2011). Melt-induced speed-up of Greenland ice sheet offset by efficient subglacial drainage. *Nature*, 469(7331):521.

Tahar, K. (2013). An evaluation on different number of ground control points in unmanned aerial vehicle photogrammetric block. *Int. Arch. Photogramm. Remote Sens. Spat. Inf. Sci*, 40:93–98.

Taylor, Z. J., Gurka, R., Kopp, G. A., and Liberzon, A. (2010). Long-duration time-resolved PIV to study unsteady aerodynamics. *IEEE Transactions on Instrumentation and Measurement*, 59(12):3262–3269.

Tedesco, M., Willis, I. C., Hoffman, M. J., Banwell, A. F., Alexander, P., and Arnold, N. S. (2013). Ice dynamic response to two modes of surface lake drainage on the Greenland ice sheet. *Environmental Research Letters*, 8(3):034007.

Tedstone, A. J., Cook, J. M., Williamson, C. J., Hofer, S., McCutcheon, J., Irvine-Fynn, T., Gribbin, T., and Tranter, M. (2020). Algal growth and weathering crust state drive variability in western Greenland Ice Sheet ice albedo. *The Cryosphere*, 14(2):521–538.

Tedstone, A. J., Nienow, P. W., Gourmelen, N., Dehecq, A., Goldberg, D., and Hanna, E. (2015). Decadal slowdown of a land-terminating sector of the Greenland Ice Sheet despite warming. *Nature*, 526(7575):692.

Tedstone, A. J., Nienow, P. W., Sole, A. J., Mair, D. W., Cowton, T. R., Bartholomew, I. D., and King, M. A. (2013). Greenland ice sheet motion insensitive to exceptional meltwater forcing. *Proceedings of the National Academy of Sciences*, 110(49):19719–19724.

Telling, J. W., Glennie, C., Fountain, A. G., and Finnegan, D. C. (2017). Analyzing glacier surface motion using LiDAR data. *Remote Sensing*, 9(3):283.

Tewinkel, G. (1963). Water depths from aerial photographs. *Photogrammetric Engineering*, 29(10):1037–1042.

Todd, J., Christoffersen, P., Zwinger, T., Råback, P., and Benn, D. I. (2019). Sensitivity of a calving glacier to ice—ocean interactions under climate change: New insights from a 3-D full-Stokes model. *The Cryosphere*.

Todd, J., Christoffersen, P., Zwinger, T., Råback, P., Chauché, N., Benn, D., Luckman, A., Ryan, J., Toberg, N., Slater, D., and Hubbard, A. (2018). A Full-Stokes 3D Calving Model applied to a large Greenlandic Glacier. *Journal of Geophysical Research: Earth Surface*.

Tonkin, T. N. and Midgley, N. G. (2016). Ground-Control Networks for Image Based Surface Reconstruction: An Investigation of Optimum Survey Designs Using UAV Derived Imagery and Structure-from-Motion Photogrammetry. *Remote Sensing*, 8(9):786.

Tonkin, T. N., Midgley, N. G., Cook, S. J., and Graham, D. J. (2016). Ice-cored moraine degradation mapped and quantified using an unmanned aerial vehicle: A case study from a polythermal glacier in Svalbard. *Geomorphology*, 258:1–10.

Trusel, L. D., Das, S. B., Osman, M. B., Evans, M. J., Smith, B. E., Fettweis, X., McConnell, J. R., Noël, B. P., and van den Broeke, M. R. (2018). Nonlinear rise in Greenland runoff in response to post-industrial Arctic warming. *Nature*, 564(7734):104–108.

Van Angelen, J., Van den Broeke, M., Wouters, B., and Lenaerts, J. (2014). Contemporary (1960–2012) evolution of the climate and surface mass balance of the Greenland ice sheet. *Surveys in Geophysics*, 35(5):1155–1174.

Van de Wal, R., Smeets, C., Boot, W., Stoffelen, M., Van Kampen, R., Doyle, S. H., Wilhelms, F., van den Broeke, M. R., Reijmer, C., Oerlemans, J., et al. (2015). Self-regulation of ice flow varies across the ablation area in south-west Greenland. *Cryosphere*, 9(2):603–611.

van de Wal, R. S., Boot, W., Van den Broeke, M., Smeets, C., Reijmer, C., Donker, J., and Oerlemans, J. (2008). Large and rapid melt-induced velocity changes in the ablation zone of the Greenland Ice Sheet. *Science*, 321(5885):111–113.

Van den Broeke, M. R., Enderlin, E. M., Howat, I. M., Kuipers Munneke, P., Noël, B. P., Jan Van De Berg, W., Van Meijgaard, E., and Wouters, B. (2016). On the recent contribution of the Greenland ice sheet to sea level change. *The Cryosphere*, 10(5):1933–1946.

van der Sluijs, J., Kokelj, S., Fraser, R., Tunnicliffe, J., and Lacelle, D. (2018). Permafrost Terrain Dynamics and Infrastructure Impacts Revealed by UAV Photogrammetry and Thermal Imaging. *Remote Sensing*, 10(11):1734.

Van der Veen, C. (1998). Fracture mechanics approach to penetration of surface crevasses on glaciers. *Cold Regions Science and Technology*, 27(1):31–47.

van der Veen, C. J. (1999). Crevasses on glaciers. *Polar Geography*, 23(3):213–245.

van der Veen, C. J. (2007). Fracture propagation as means of rapidly transferring surface meltwater to the base of glaciers. *Geophysical Research Letters*, 34(1).

Vaughan, D. G. (1993). Relating the occurrence of crevasses to surface strain rates. *Journal of Glaciology*, 39(132):255–266.

Velicogna, I., Sutterley, T., and Van Den Broeke, M. (2014). Regional acceleration in ice mass loss from Greenland and Antarctica using grace time-variable gravity data. *Geophysical Research Letters*, 41(22):8130–8137.

Voigt, U. (1966). The determination of the direction of movement on glacier surfaces by terrestrial photogrammetry. *Journal of Glaciology*, 6(45):359–367.

Voytenko, D., Dixon, T. H., Holland, D. M., Cassotto, R., Howat, I. M., Fahnestock, M. A., Truffer, M., and De la Pena, S. (2017). Acquisition of a 3 min, two-dimensional glacier velocity field with terrestrial radar interferometry. *Journal of Glaciology*, 63(240):629–636.

Voytenko, D., Stern, A., Holland, D. M., Dixon, T. H., Christianson, K., and Walker, R. T. (2015). Tidally driven ice speed variation at Helheim Glacier, Greenland, observed with terrestrial radar interferometry. *Journal of Glaciology*, 61(226):301–308.

Walter, F., Chaput, J., and Lüthi, M. P. (2014). Thick sediments beneath Greenland's ablation zone and their potential role in future ice sheet dynamics. *Geology*, 42(6):487–490.

Watson, C. S., Quincey, D. J., Smith, M. W., Carrivick, J. L., Rowan, A. V., and James, M. R. (2017). Quantifying ice cliff evolution with multi-temporal point

clouds on the debris-covered Kumbu Glacier, Nepal. *Journal of Glaciology*, 63(241):823–837.

Weertman, J. (1973). Can a water-filled crevasse reach the bottom surface of a glacier. *International Association of Scientific Hydrology*, 95:139–145.

Weidick, A. (1995). Greenland, with a section on Landsat images of Greenland. In Williams, R. S. and Ferrigno, J. G., editors, *Satellite image atlas of glaciers of the world*, pages C1 – C105 (USGS Professional Paper 1386–C). US Geological Survey, Washington, DC.

Werder, M. A., Hewitt, I. J., Schoof, C. G., and Flowers, G. E. (2013). Modeling channelized and distributed subglacial drainage in two dimensions. *Journal of Geophysical Research: Earth Surface*, 118(4):2140–2158.

Westaway, R., Lane, S., and Hicks, D. (2000). The development of an automated correction procedure for digital photogrammetry for the study of wide, shallow, gravel-bed rivers. *Earth Surface Processes and Landforms*, 25(2):209–226.

Westoby, M. J., Brasington, J., Glasser, N. F., Hambrey, M. J., and Reynolds, J. (2012). 'Structure-from-Motion' photogrammetry: A low-cost, effective tool for geoscience applications. *Geomorphology*, 179:300–314.

Westoby, M. J., Dunning, S. A., Hein, A. S., Marrero, S. M., and Sugden, D. E. (2016). Interannual surface evolution of an Antarctic blue-ice moraine using multi-temporal DEMs. *Earth Surface Dynamics*, 4(2):515–529.

Whitehead, K. and Hugenholtz, C. H. (2014). Remote sensing of the environment with small unmanned aircraft systems (UASs), part 1: A review of progress and challenges. *Journal of Unmanned Vehicle Systems*, 2(3):69–85.

Whitehead, K., Moorman, B., and Hugenholtz, C. (2013). Brief communication: Low-cost, on-demand aerial photogrammetry for glaciological measurement. *The Cryosphere*, 7(6):1879.

Wigmore, O. and Mark, B. (2017). Monitoring tropical debris-covered glacier dynamics from high-resolution unmanned aerial vehicle photogrammetry, Cordillera Blanca, Peru. *The Cryosphere*, 11(6):2463–2480.

Williams, J. J., Gourmelen, N., and Nienow, P. (2020). Dynamic response of the Greenland ice sheet to recent cooling. *Scientific Reports*, 10(1):1–11.

Williamson, A. G., Arnold, N. S., Banwell, A. F., and Willis, I. C. (2017). A Fully Automated Supraglacial lake area and volume Tracking ("FAST") algorithm: Development and application using MODIS imagery of West Greenland. *Remote Sensing of Environment*, 196:113–133.

Williamson, A. G., Banwell, A. F., Willis, I. C., and Arnold, N. S. (2018a). Dual-satellite (Sentinel-2 and Landsat 8) remote sensing of supraglacial lakes in Greenland. *The Cryosphere*, 12(9):3045–3065.

Williamson, A. G., Willis, I. C., Arnold, N. S., and Banwell, A. F. (2018b). Controls on rapid supraglacial lake drainage in West Greenland: an Exploratory Data Analysis approach. *Journal of Glaciology*, 64(244):208–226.

Young, T. J., Christoffersen, P., Doyle, S. H., Nicholls, K. W., Stewart, C., Hubbard, B., Hubbard, A., Lok, L. B., Brennan, P. V., Benn, D. I., et al. (2019). Physical Conditions of Fast Glacier Flow: 3. Seasonally-Evolving Ice Deformation on Store Glacier, West Greenland. *Journal of Geophysical Research: Earth Surface*, 124(1):245–267.

Zwally, H. J., Abdalati, W., Herring, T., Larson, K., Saba, J., and Steffen, K. (2002). Surface melt-induced acceleration of Greenland ice-sheet flow. *Science*, 297(5579):218–222.

Appendix A

Results I Supplementary Material

Table A.1 List of flights used to produce data in this study. 'Time' refers to the local time (West Greenland Summer Time) at the flight midpoint.

Location	Date	Time
Calving Front	2017-07-10	12:33
	2017-07-10	18:45
	2017-07-11	10:20
	2017-07-11	16:50
	2017-07-11	22:06
	2017-07-12	10:08
	2017-07-12	16:18
	2017-07-12	22:17
	2017-07-13	10:15
	2017-07-14	22:03
Downstream Transverse	2017-07-22	15:22
	2017-07-26	19:29
Upstream Longitudinal	2017-07-22	21:35
	2017-07-26	11:26
Downstream Longitudinal	2017-07-22	14:24
	2017-07-26	08:43

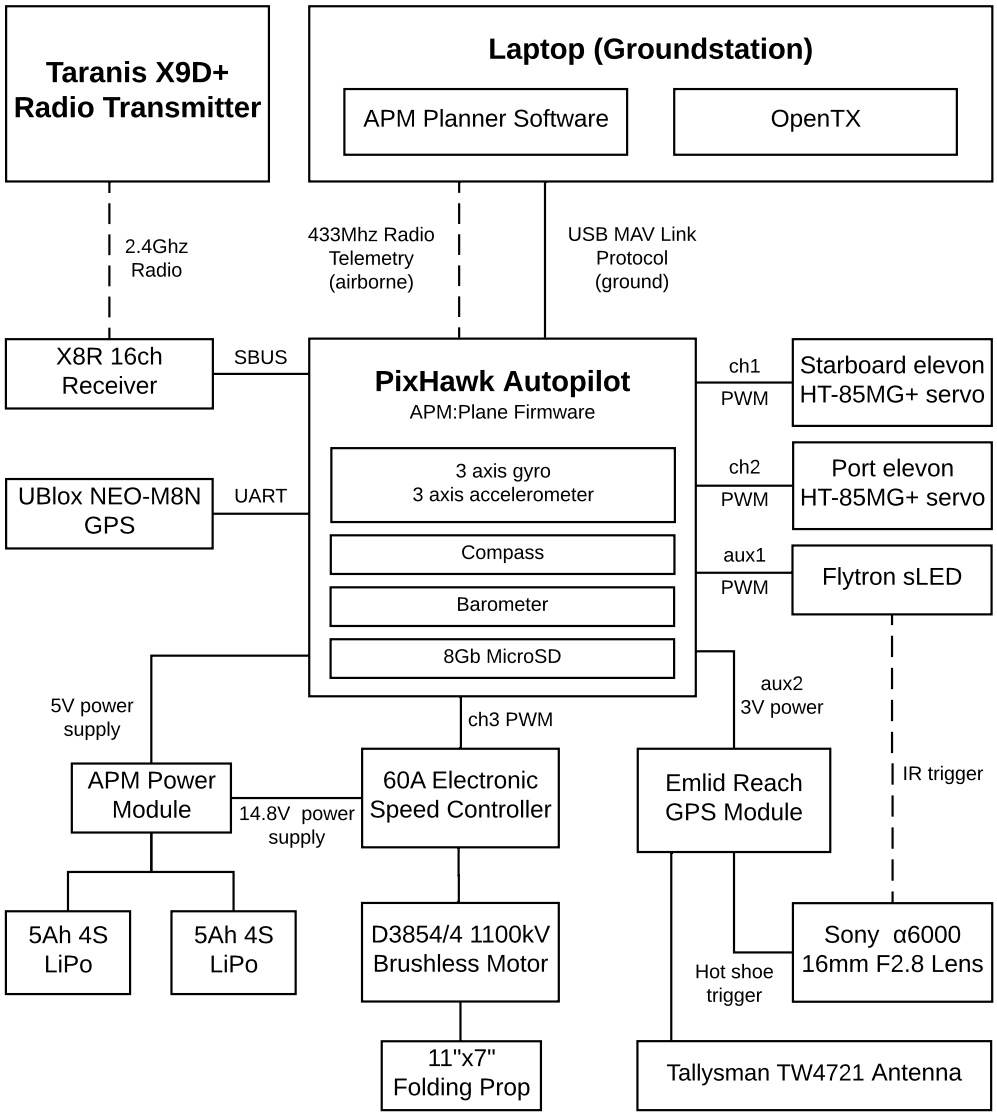

Fig. A.1 Components and set-up of Skywalker X8 UAV used in this study.

Appendix B

Results II Supplementary Material

Depth Correction of Photogrammetry-Derived Lake Bathymetry

Photogrammetry is known to underestimate the depth of water bodies observed from the air due to influence from refraction at the air-water interface (e.g. Fryer, 1983; Fryer and Kniest, 1985; Harris and Umbach, 1972; Mulsow et al., 2018; Tewinkel, 1963; Westaway et al., 2000). Under idealised conditions, corrections can be determined precisely if the imaging geometry relative to the interface is known but, in the Photoscan software used here, the critical information on which photographs contribute to each individual point in the final model, is not available. Although estimates and simplifications can be used (Dietrich, 2017), through having repeat DEMs of the lake basin (i) prior to and (ii) following lake drainage, our study allowed us to infer an empirical correction factor on observed lake depth. This correction factor was derived as the slope of a linear regression performed between the apparent depth of the submerged regions and their 'true' position derived after lake drainage. Areas of <0.5 m apparent depth were eliminated prior to this regression as they often contained floating ice. We performed this regression across multiple comparisons between three DEMs of the highest water level (5th, 6th, and 7th July) against the four DEMs of the lowest water level (12th, 15th, 24th, 28th July) in order to minimise the influence of vertical error and artefacting in individual DEMs. The average slope of the regression fit was 1.32, which was applied as the correction factor to all submerged regions of DEMs. We note that this value is within 1% of the refractive index of water – suggesting that, for our Photoscan-

processed nadir image sets, a straightforward first-order refraction correction (e.g. Westaway et al., 2000) would suffice.

To produce a single time-averaged lake bathymetry for pressure-sensor depth-volume calculation, we median-averaged all the pre-drainage DEMs (5th, 6th, and 7th July) before applying a 2 m gaussian filter in order to remove the impacts of floating lake ice, advecting crevasses, progressive ice surface ablation, and data artefacts present in individual DEMs.

Supplementary Movie

Movie B.1 Time lapse photography of the lake drainage taken every 10 seconds between 2018-07-07 21:21:10 and 2018-07-08 01:30:00. Displayed alongside is a zoomed-in and time-marked version of Figure 3 in the main text. The movie is available as supplementary information to the published version of this chapter (Chudley et al., 2019b) at https://doi.org/10.1073/pnas.1913685116.

Supplementary Table

Table B.1 Dates and time (UTC) of UAV flights used in this study. Times represent the midpoints of flights, rounded to the nearest five minutes. For further information on the 2017 flight, see Chudley et al. (2019a).

Date	Time
2017-07-26	11:35
2018-07-05	02:00
2018-07-06	16:40
2018-07-07	12:45
2018-07-08	01:40
2018-07-08	15:15
2018-07-09	18:15
2018-07-12	15:25
2018-07-15	13:00
2018-07-18	12:00
2018-07-24	21:30
2018-07-28	12:50

Supplementary Figures

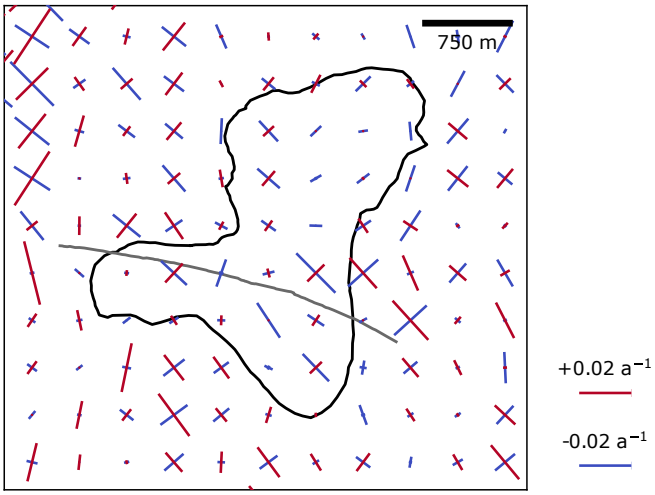

Fig. B.1 Surface principal strain rates (red and blue lines) around Lake F derived from 2017 annual MEASUREs velocity data (Joughin et al., 2010). Maximum lake extent (black) and fracture (grey) from (Doyle et al., 2013). Note the order-of-magnitude difference in strain vector scale between this figure and figure 6.

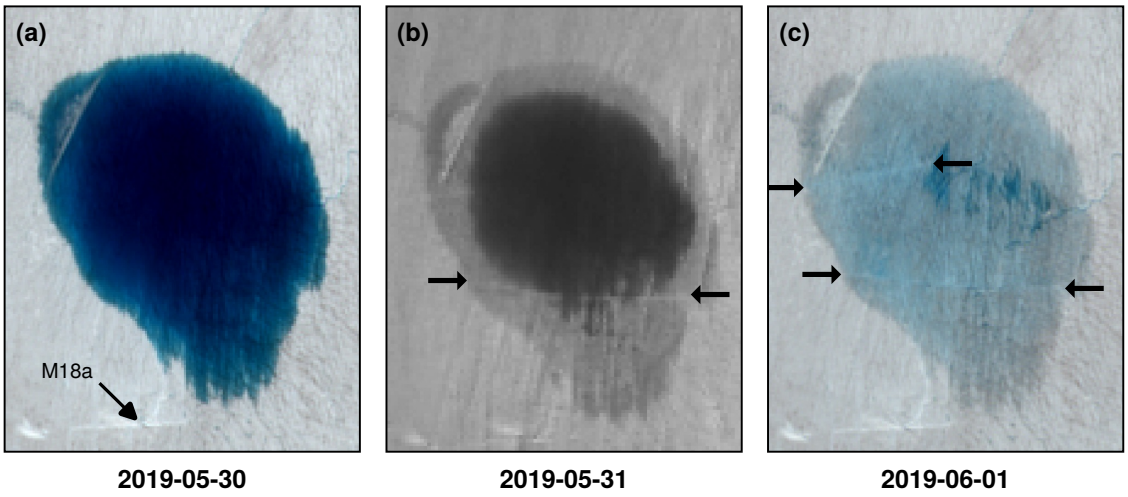

Fig. B.2 The 2019 drainage of Lake 028 as captured by RGB Sentinel-2 (a, c) and panchromatic Landsat-8 OLI (b) imagery. Arrows identify the ends of drainage fractures.

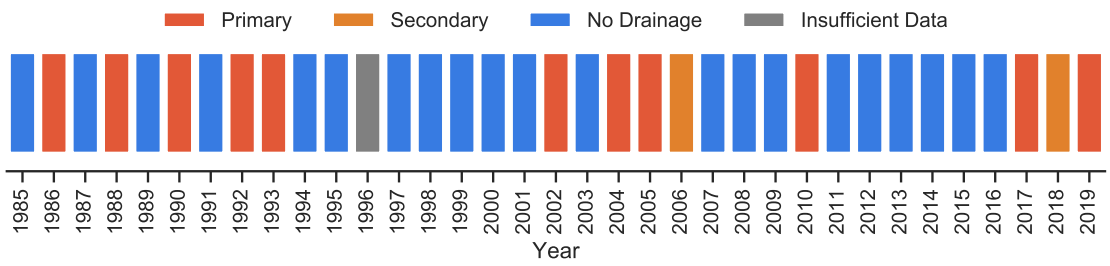

Fig. B.3 Drainage history of Lake 028, as manually assessed from historical Landsat and Sentinel-2 data.

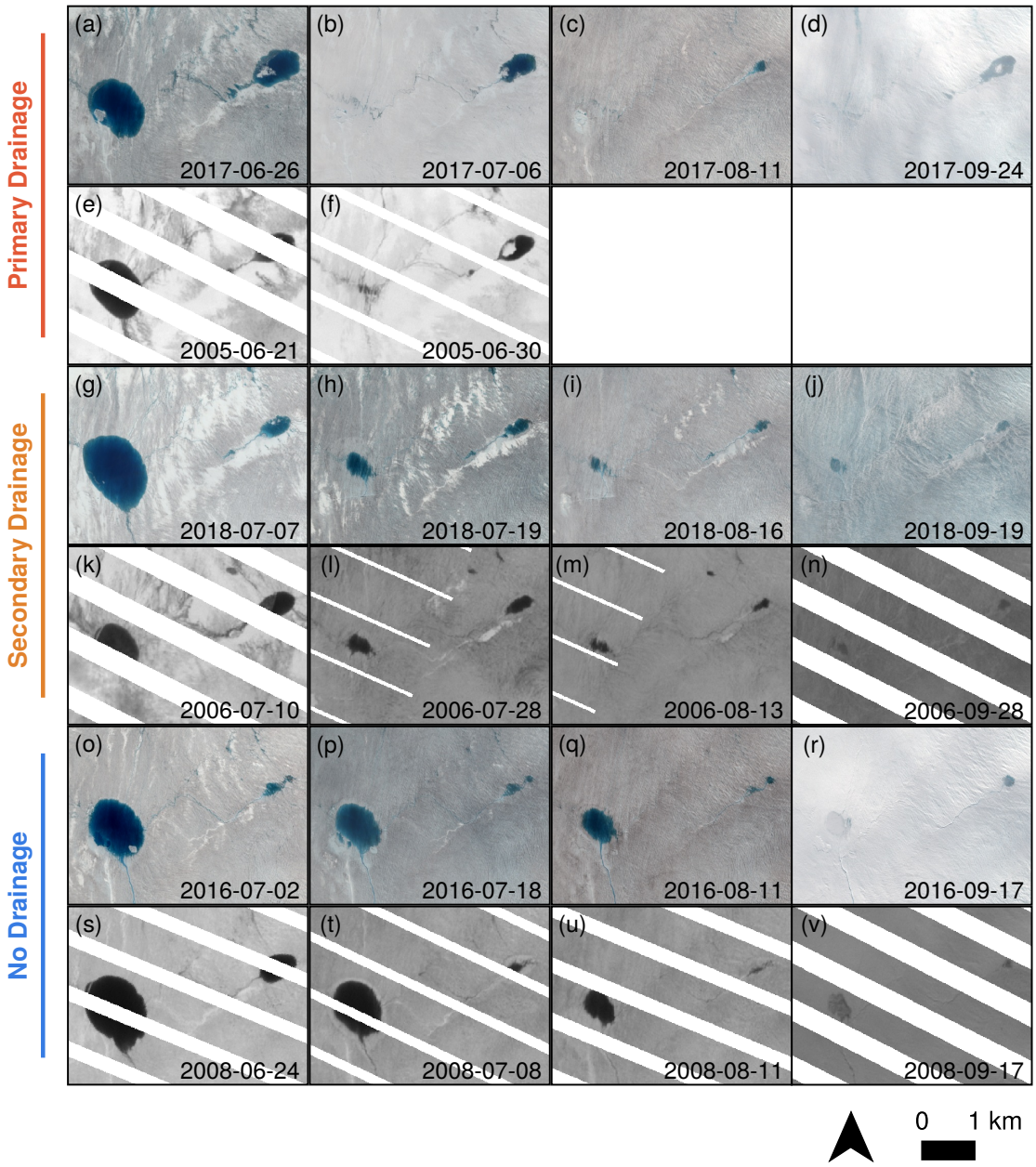

Fig. B.4 Sentinel-2 false colour and Landsat 7 ETM+ (SLC-off) panchromatic imagery showing examples of the three modes of drainage of Lake 028 (left-hand lake in images) paired with Lake 031 (right-hand lake in images). (a–f) Type I 'primary' drainage occurring when Lake 028 had not drained the year before, showing the total loss of lake volume. (g–n) Type II 'secondary' drainage, occurring in years where type I drainage had occurred in the prior year, showing partial lake drainage and cut-off of outflow channel. (o–v) Examples of no drainage (NB the continuation of outflow channel, in contrast to reactivation drainage).

Appendix C

Results III Supplementary Material

Supplementary Table

Table C.1 Dates and time (UTC) of UAV flights used in this study. Times represent the midpoints of flights, rounded to the nearest five minutes.

Date	Time (UTC)
2018-07-05	21:10
2018-07-06	19:25
2018-07-07	17:25
2018-07-08	19.25
2018-07-18	14:20

Supplementary Figures

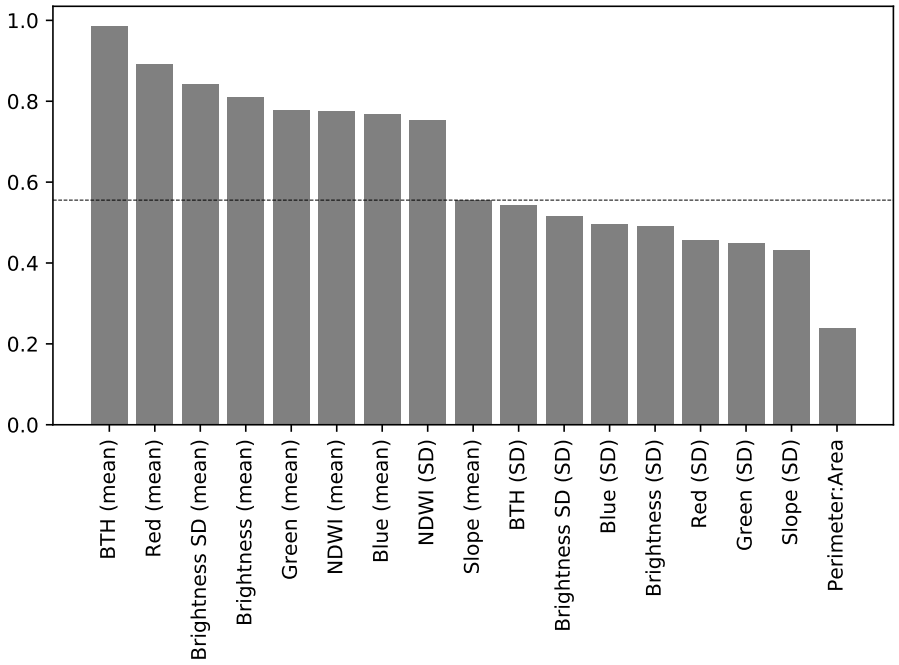

Fig. C.1 Results of mutual information tests for all potential input variables against training data. Median value is marked by the dotted line. BTH is black top-hat filter. SD is standard deviation.

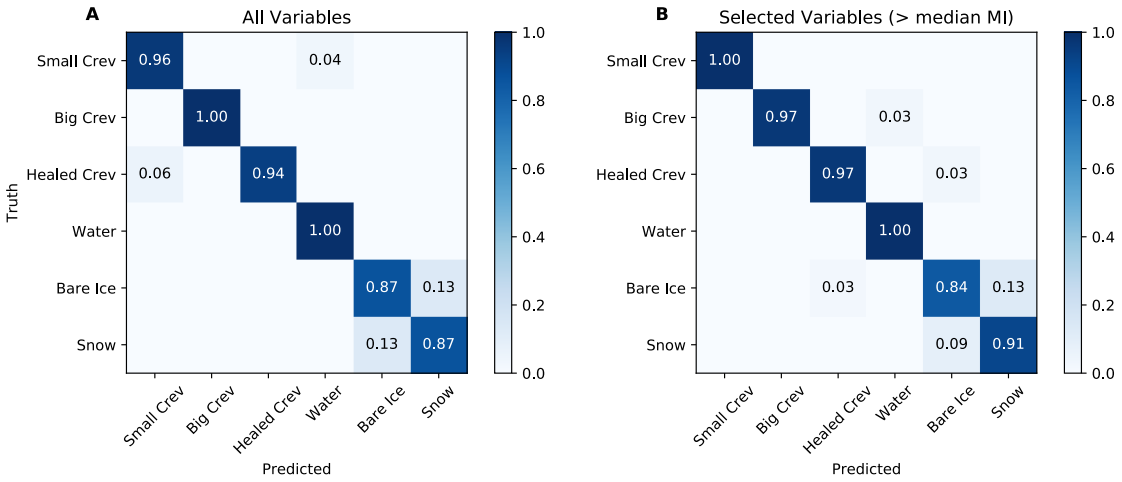

Fig. C.2 Confusion diagrams for object-based image analysis of 2018-07-08 imagery for (A) all input variables; and (B) selected input variables with mutual information test results greater than median.

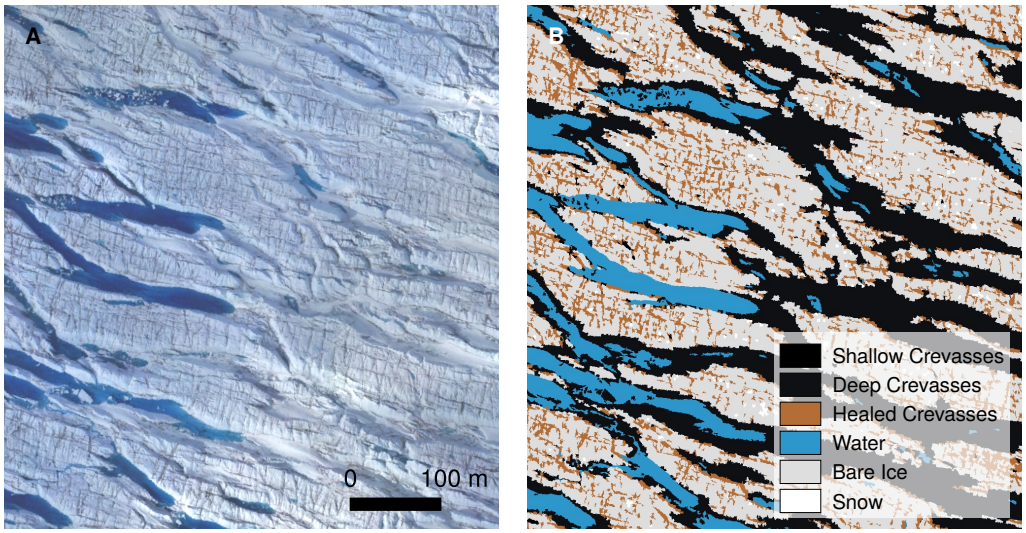

Fig. C.3 Example results for object-based image analysis of 2018-07-08 imagery. (A) Segmented orthophoto. (B) Full classification into six surface types.

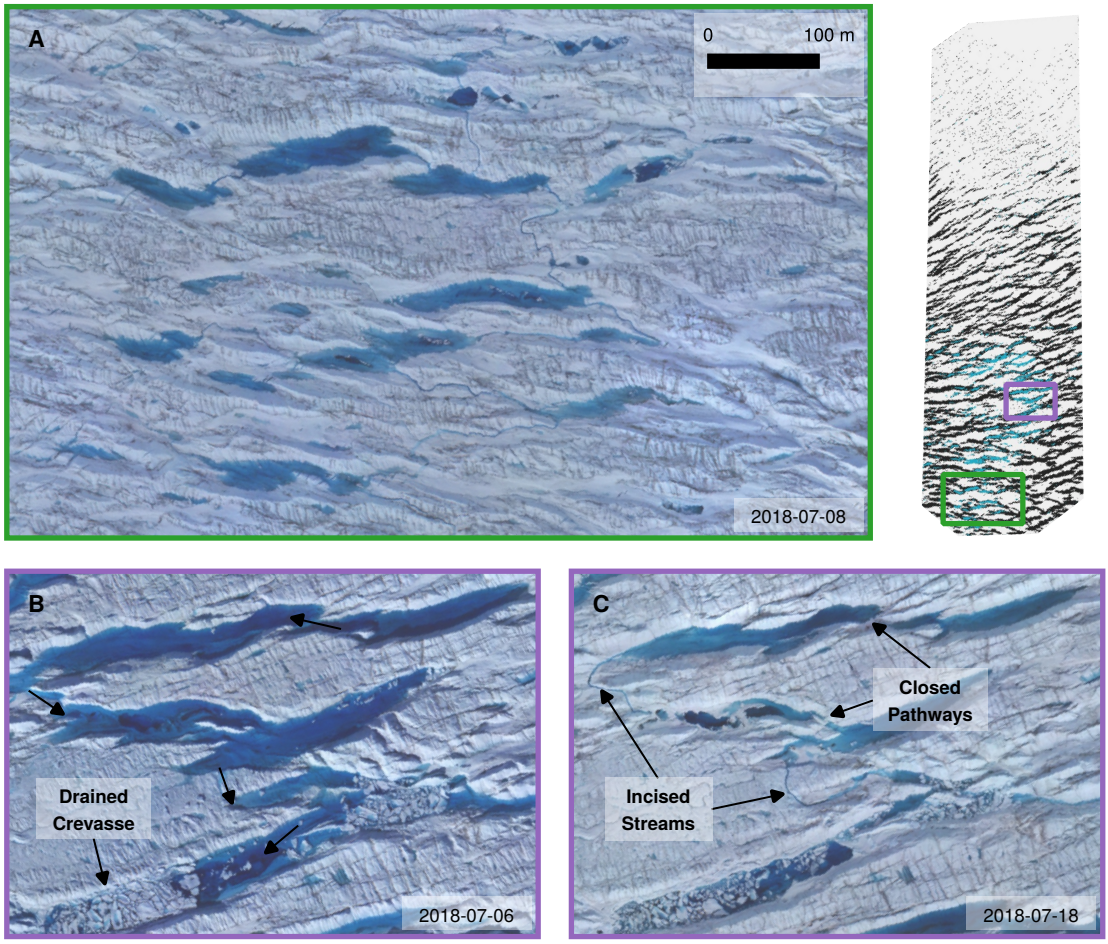

Fig. C.4 Supraglacial connections between crevasses. (A) Southwestern extent of UAV survey area, displaying clear incised supraglacial pathways between crevasses. (B–C) Crevasse system identified in main figure 7A–B in the 24 hours following (B) and 12 days following (C) drainage, showing the development of incised streams as water level lowers. Inset: subfigure extents identified in full UAV survey extent.